2009

# An Improved Hurrican Wind Vector Retrieval Algorithm Using Sea Winds Scatterometer

Peth Laupattarakasem
*University of Central Florida*

# AN IMPROVED HURRICANE WIND VECTOR RETRIEVAL ALGORITHM USING SEAWINDS SCATTEROMETER

by

PETH LAUPATTARAKASEM

M.S. Florida Atlantic University, 2003

A dissertation submitted in partial fulfillment of the requirements
for the degree of Doctor of Philosophy
in the School of Electrical Engineering and Computer Science
in the College of Engineering and Computer Science
at the University of Central Florida

Orlando, Florida

Spring Term

2009

Major Professor: W. Linwood Jones

# ABSTRACT

Over the last three decades, microwave remote sensing has played a significant role in ocean surface wind measurement, and several scatterometer missions have flown in space since early 1990's. Although they have been extremely successful for measuring ocean surface winds with high accuracy for the vast majority of marine weather conditions, unfortunately, the conventional scatterometer cannot measure extreme winds condition such as hurricane.

The SeaWinds scatterometer, onboard the QuikSCAT satellite is NASA's only operating scatterometer at present. Like its predecessors, it measures global ocean vector winds; however, for a number of reasons, the quality of the measurements in hurricanes are significantly degraded. The most pressing issues are associated with the presence of precipitation and Ku-band saturation effects, especially in extreme wind speed regime such as tropical cyclones (hurricanes and typhoons).

Under this dissertation, an improved hurricane ocean vector wind retrieval approach, named as Q-Winds, was developed using existing SeaWinds scatterometer data. This unique data processing algorithm uses combined SeaWinds active and passive measurements to extend the use of SeaWinds for tropical cyclones up to approximately 50 m/s (Hurricane Category-3).

Results show that Q-Winds wind speeds are consistently superior to the standard SeaWinds Project Level 2B wind speeds for hurricane wind speed measurement, and also Q-Winds

provides more reliable rain flagging algorithm for quality assurance purposes. By comparing to H*Wind, Q-Winds achieves ~9% of error, while L2B-12.5km exhibits wind speed saturation at ~30 m/s with error of ~31% for high wind speed (> 40 m/s).

To my parents: Prof. Wiroon Laupattarakasem and Dr. Pisamai Laupattarakasem,

and family

# ACKNOWLEDGMENTS

I would like to express my deepest gratitude to my advisor, Dr. W. Linwood Jones, his guidance, dedication, and support throughout the program. Also as a mentor, I'm grateful for the time he invested in me and for sharing his work experiences and life lessons. I also would like to thank my committee members: Dr. Takis Kasparis, Dr. Larry Andrews, Dr. Christopher Hennon, and Mr. James Johnson for their kind advices.

I also would like to acknowledge my parents, Prof. Wiroon and Dr. Pisamai Laupattarakasem. I would like to thank them for their unconditional love and support - I would not accomplish this far without both of them. They have always been the steps I would follow without hesitation and the arms that always embrace me with warmth.

This research was sponsored under a grant with NASA Headquarters for ROSES earth sciences investigations of the Ocean Vector Winds Science Team.

# TABLE OF CONTENTS

# LIST OF FIGURES

# LIST OF TABLES

# LIST OF ACRONYMS/ABBREVIATIONS

| | |
|---|---|
| ADEOS | Advanced Earth Observing Satellite |
| AFRC | Air Force Reserve Command |
| AMSR | Advanced Microwave Scanning Radiometer |
| ASCAT | Advanced Scatterometer |
| CCW | Counter-clockwise |
| CFRSL | Central Florida Remote Sensing Laboratory |
| CPHC | Central Pacific Hurricane Center |
| DMSP | Defense Meteorological Satellite Program |
| ERS | European Remote Sensing Satellite |
| EM | Electromagnetic |
| ESA | European Space Agency |
| GDAS | Global Data Assimilation System |
| GMF | Geophysical Model Function |
| GOES | Geostationary Operational Environmental Satellite |
| GPS | Global Positioning System |

| | |
|---|---|
| H*Wind | Hurricane Wind Analysis System |
| HDF | Hierachical Data Format |
| HRD | Hurricane Research Division |
| IFOV | Instantaneous-field-of-view |
| JAXA | Japan Aerospace Exploration Agency (formerly NASDA) |
| JHT | Joint Hurricane Testbed |
| JPL | Jet Propulsion Laboratory |
| JTWC | Joint Typhoon Warning Center |
| L2A | QuikSCAT Level 2A |
| L2B | QuikSCAT Level 2B |
| MetOp | Meteorological Operational |
| MLE | Maximum Likelihood Estimation |
| MUDH | Multidimensional Histogram |
| NASA | National Aeronautics and Space Administration |
| NASDA | National Space Development Agency (currently JAXA) |
| NCEP | National Centers for Environmental Prediction |
| NESDIS | National Environmental Satellite, Data, and Information Service |

| | |
|---|---|
| NHC | National Hurricane Center |
| NOAA | National Oceanic and Atmospheric Administration |
| NRCS | Normalized Radar Cross Section |
| NRL | Naval Research Laboratory |
| NSCAT | NASA Scatterometer |
| NWP | Numerical Weather Prediction |
| NWS | National Weather Service |
| OSVW | Ocean Surface Vector Winds |
| PODAAC | Physical Oceanography Distributed Active Archive Center |
| Q-Winds | QuikSCAT Wind Vector Retrieval |
| QC | Quality Control |
| QuikSCAT | Quick Scatterometer |
| QRad | QuikSCAT Radiometer |
| QS-GMF | QuikSCAT Geophysical Model Function |
| SASS | SeaSat-A Satellite Scatterometer |
| SFMR | Stepped Frequency Microwave Radiometer |
| SNR | Signal-to-noise Ratio |

| | |
|---|---|
| SSM/I | Special Sensor Microwave/Imager |
| SST | Sea Surface Temperature |
| STD | Standard Deviation |
| Tb | Brightness Temperature |
| TC | Tropical Cyclone |
| TMI | TRMM Microwave Imager |
| TPC | Tropical Prediction Center |
| TRMM | Tropical Rainfall Measuring Mission Microwave Imager |
| WVC | Wind Vector Cell |
| XW-GMF | Extreme Winds Geophysical Model Function |

# CHAPTER-I: INTRODUCTION

Tropical cyclones (hurricanes and typhoons) are one of the greatest natural threats for ships at sea, inhabited coastal areas and islands. Once they make landfall, they can cause severe wind and flood damage, which can result in catastrophic loss in both human lives and property. Unfortunately, there is currently no human intervention that has demonstrated any significant mitigation to lessen their impact except for civil hurricane preparedness, which includes warning and evacuation. Therefore, accurate observational information on the extent and magnitude of hurricane surface winds is critical for the world's operational weather forecast community to predict storm path and intensity and to issue timely warnings to those in harm's way. In the United States, tropical cyclones (TC's) are monitored by several federal governmental organizations with the National Oceanic and Atmospheric Administration (NOAA) taking the lead.

Since hurricanes spawn in the ocean and usually are distant from land, the use of satellite remote sensing plays an important role in their monitoring; and microwave sensors are especially vital for this purpose because they "see" through clouds to measure surface conditions. For the past two decades, space-borne active microwave remote sensing (using scatterometry) has been an effective method to acquire ocean surface (vector) winds information by interpreting ocean radar backscatter. Scatterometers have achieved high accuracy for synoptic ocean wind conditions and have provided these measurements under all-weather, day/night conditions with high spatial and temporal sampling and global coverage over ice-free oceans. The ocean (surface) vector winds

(OVW) data from NASA's SeaWinds scatterometer on the QuikSCAT satellite are captured in near-real time and are incorporated in operational marine weather forecasts worldwide. In regards to tropical cyclones, the QuikSCAT OVW data have become an important tool for storm analysis and diagnostics at all of federal agencies responsible for tropical cyclone forecasting and warning, including the Tropical Prediction Center/National Hurricane Center (TPC/NHC), Central Pacific Hurricane Center (CPHC), the Weather Forecast Office (WFO) Guam, and Joint Typhoon Warning Center (JTWC).

For tropical cyclones in the North Atlantic and eastern North Pacific basins, the NHC is responsible for tracking and warnings. The QuikSCAT wind speed and direction retrieval are utilized in TC analysis; the use of QuikSCAT has been steadily increased since 2000. For example, during the period 2003 - 2006, QuikSCAT data were used 17% of the time to determine storm radii, 21% of the time to identify storm fix, and 62% of the time to estimate storm intensity [1, 2]; and their impact (and limitations) have been well documented [1-5].

## 1.1 History of Active Microwave Wind Vector Retrieval

The idea of using radar to estimate ocean surface wind conditions originated during World War II (1940's), where the interest was primarily to understand how ocean backscatter interference, referred as sea "clutter", would impede the detection of ships and submarine periscopes at incidence angles near grazing. During this period, it was recognized that there was a cause and effect relationship between ocean clutter, wind speed and sea state (wave height); but it was not until the 1960s that the clutter was scientifically understood. In 1963, Richard Moore and

Willard Pierson [6, 7] first proposed that the ocean wind speed could be inferred by radar remote sensing techniques by interpreting the magnitude of the ocean backscatter.

During the 1960's and 70's, ocean remote sensing were actively studied within the National Aeronautics and Space Administration (NASA) and US Navy research communities. There were a number of groups who were engaged in research to define the fundamental physics and develop the technology of microwave scatterometry for the measurement of oceanic wind vector [8-11].

From the collection of theoretical and experiment results, it was discovered that a robust relationship exists between the ocean normalized radar cross section (sigma-0, $\sigma^0$) and the wind stress at the air/sea interface. The $\sigma^0$ is the result of the resonant Bragg backscatter from the small-scale ocean "capillary" waves that have wavelengths of the order of a few centimeters on ocean surface. Further capillary wave amplitudes are proportional to the surface wind stress and thereby carry the information of the magnitude and direction of the local near-surface winds [12].

Numerous airborne experiments were conducted during the late 1960's and early 70's, which established the empirical relationship between $\sigma^0$ and the neutral stability local wind vector. These experiments lay the foundation for the feasibility of the remote sensing of ocean wind vector from space [13].

The discussion that follows presents an abbreviated history of satellite OVW scatterometer instruments sponsored by NASA and the European Space Agency (ESA). An illustration of satellite scatterometers from Skylab (1974) to present (2009) is given in Fig. 1.1 and key instrument characteristics are summarized in Table 1.1.

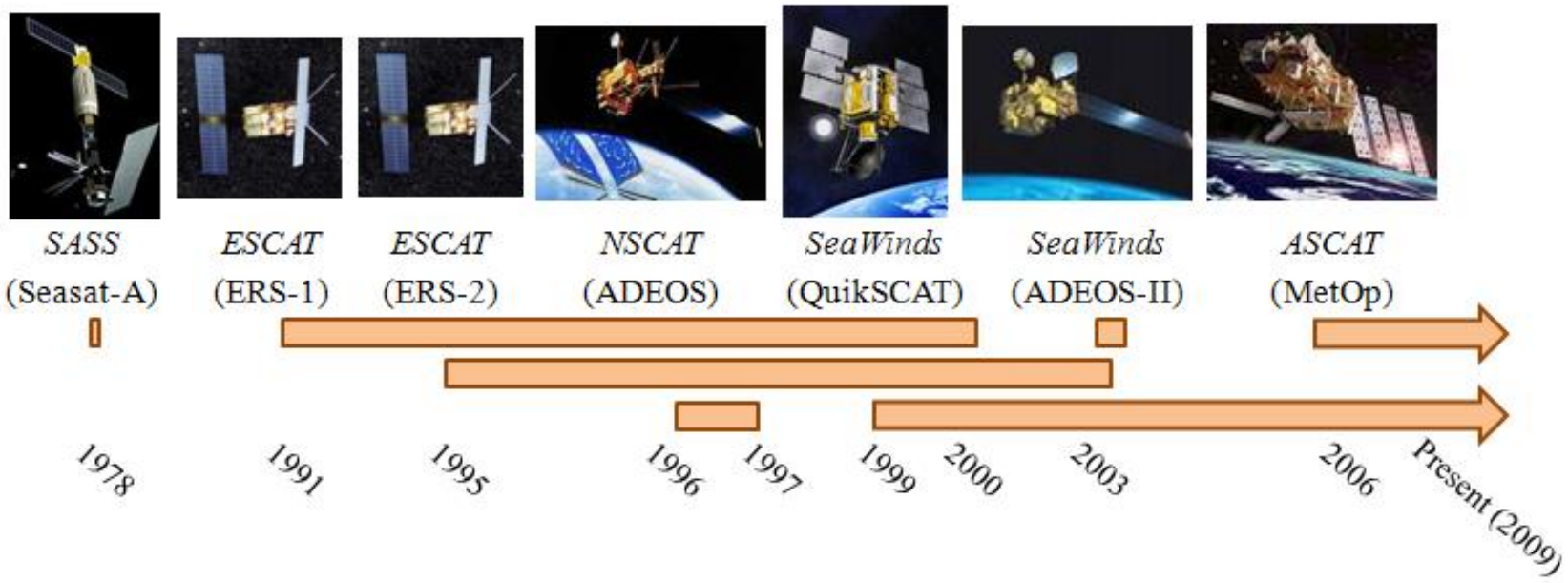


Fig. 1.1: Spaceborne wind measuring scatterometers sponsored by NASA and ESA.

Table 1.1: Characteristics of space-borne wind scatterometers.

| | SASS | ESCAT | NSCAT | SeaWinds | ASCAT |
|---|---|---|---|---|---|
| Frequency (GHz) | 14.6 | 5.3 | 14.0 | 13.4 | 5.3 |
| Antenna Azimuth Orientations |  |  |  |  |  |
| Polarizations | V-H, V-H | VV | V, V-H, V | H(Inner), v(Outer) | VV |
| Resolution (km) | 50/100 | 25/50 | 25/50 | 25/6×25 | 25/50 |
| Swath (km) | 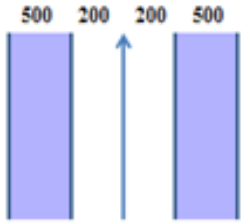 | 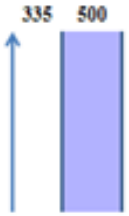 | 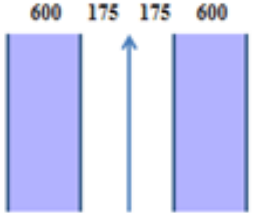 | 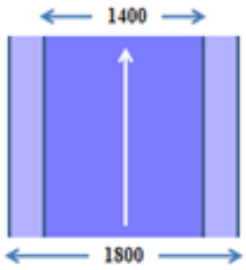 | 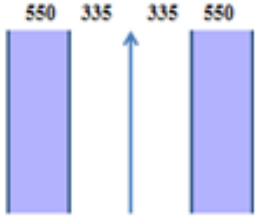 |
| Incidence Angles | 0°-70° | 18°-59° | 17°-60° | 46°,54° | 25°-65° |

## 1.2 Spaceborne Scatterometers

Satellite scatterometers are spaceborne remote sensing instruments that are designed to measure ocean surface wind speeds and directions on a global scale. Scatterometers transmit electromagnetic (EM) pulses to the Earth's surface and measure the radar backscatter response or the power of the return pulse backscattered to the antenna. The ocean surface wind speed and direction are inferred from the scatterometer geophysical model function (GMF), which relates ocean $\sigma^0$ to wind magnitude at a given azimuth "look" (relative wind direction). Because scatterometers are designed to measure synoptic scale ocean winds, their spatial resolution is not high; and their measurement grids are typically 25 – 50 km resolution. On the other hand, they do provide wide swath coverage (> 1,000 km) and near-global sampling (75 – 90%) on a daily basis.

To present, spaceborne scatterometers of 5 different designs have been deployed, and this subsection provides a brief overview of these scatterometer systems.

### *1.2.1 Skylab S-193*

The first spaceborne demonstration of ocean wind vector measurement occurred during NASA's Skylab mission in May, 1973 (Fig. 1.2) [14], when the combined Ku-band (13.9 GHz) radar altimeter/scatterometer/radiometer known as Earth Resources Package experiment S-193 flew.

The major objective of S-193, the first NASA scatterometer in space, was to demonstrate that microwave radars could operate in space, to obtain data to demonstrate the feasibility of making oceanographic measurements (waves, winds, and topography) remotely from space, and to obtain information for the future design of high-resolution altimeters.

The S-193 was equipped with a mechanically scanned one-meter parabolic antenna with dual linear polarizations. The instrument could be either operated in altimeter mode while looking at nadir (perpendicular to the surface) or in the radiometer/scatterometer (RadScat) mode with variable antenna scanning. The scanning was provided by a dual-gimbaled mount (elevation over azimuth), which allowed the RadScat to sample the ocean in different modes. Over the ocean, the primary operating mode was an along-track scan at fixed multiple angles from 0° to 48°, which resulted in a measurement of sigma-0 versus incidence angle. Also, there was another mode for the across-track scanning each selected along-track scanning incidence angle.

Because S-193 operation was astronaut attended, the operation times were limited. Further, during the second manned mission, there was a failure of one gimbal, which limited the scanning ability. As a result the total RadScat dataset was less than a few ten’s of hours operation. While S-193 did not follow-on to the next scatterometer in space (SeaSat-A Satellite Scatterometer); nevertheless, the mission was successful in achieving its major objectives, which indirectly contributed scatterometer (and altimeter) technology that was utilized in SeaSat-A.

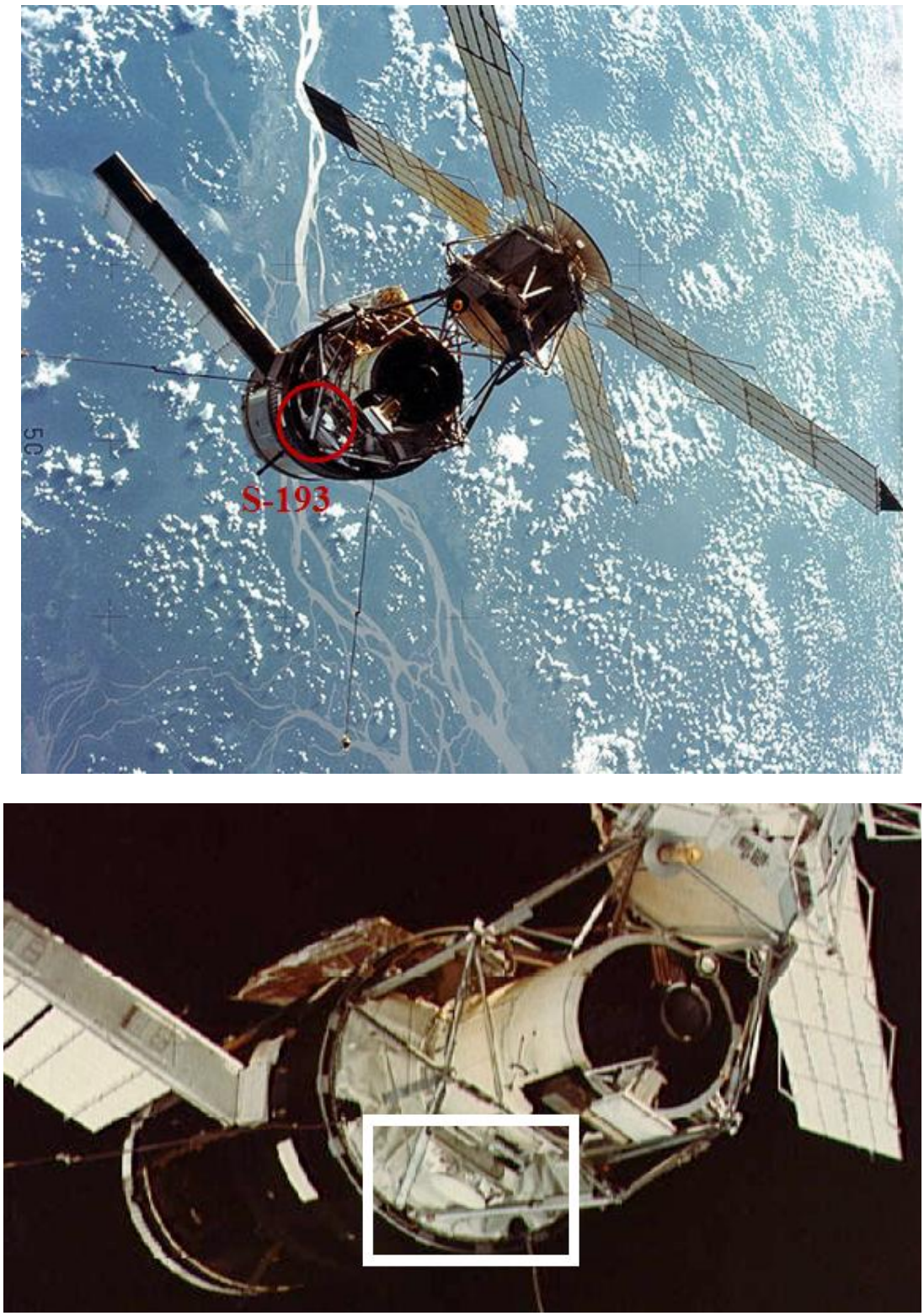


Fig. 1.2: S-193 on the Skylab space station.

### *1.2.2 SASS on SeaSat-A*

In June 1978, NASA launched its first oceanographic satellite "SeaSat-A" (Fig. 1.3) with five primary microwave instruments: an L-Band synthetic aperture radar (SAR), a radar altimeter (ALT), a scanning multi-frequency microwave radiometer (SMMR), an ocean wind scatterometer (SASS), and a visible and infrared radiometer (VIRR). The mission of SeaSat-A was a proof of concept for satellite oceanography, which was to demonstrate that it was feasible to obtain scientifically useful ocean measurements using remote sensing technologies from space. Unfortunately, the lifetime of SeaSat-A was only about 100 days because of a satellite power subsystem failure; but in this short time, sufficient data were obtained that clearly demonstrated the proof of concept for microwave active remote sensing of waves, winds, and ocean topography. SeaSat-A provided the justification for a number of satellite missions that followed.

The SeaSat-A Satellite Scatterometer (SASS) was the first satellite scatterometer specifically designed to measure the ocean surface wind vector; and as a proof-of-concept instrument, the first to demonstrate that ocean surface wind scatterometry could be achieved from space [14]. SASS operated at 14.6 GHz and had four fan-beam dual-linear (H and V) polarized antennas (±45° and ±135° relative to the flight direction), as shown in Figs. 1.3 and 1.4. The fan beams were subdivided using twelve fixed analog Doppler filters to provide contiguous footprints along the beams. Radar measurements were performed sequentially beam to beam was such that ocean was sampled approximately every 8 seconds (50 km along the track). The two beams on each

side were designed to yield two orthogonal azimuthal radar backscatter observations at each 50 km “wind vector cell”, which were used to infer the speed and direction. This geometry provided two 500-km wind vector swaths, offset ±200 km from the orbit sub-track.

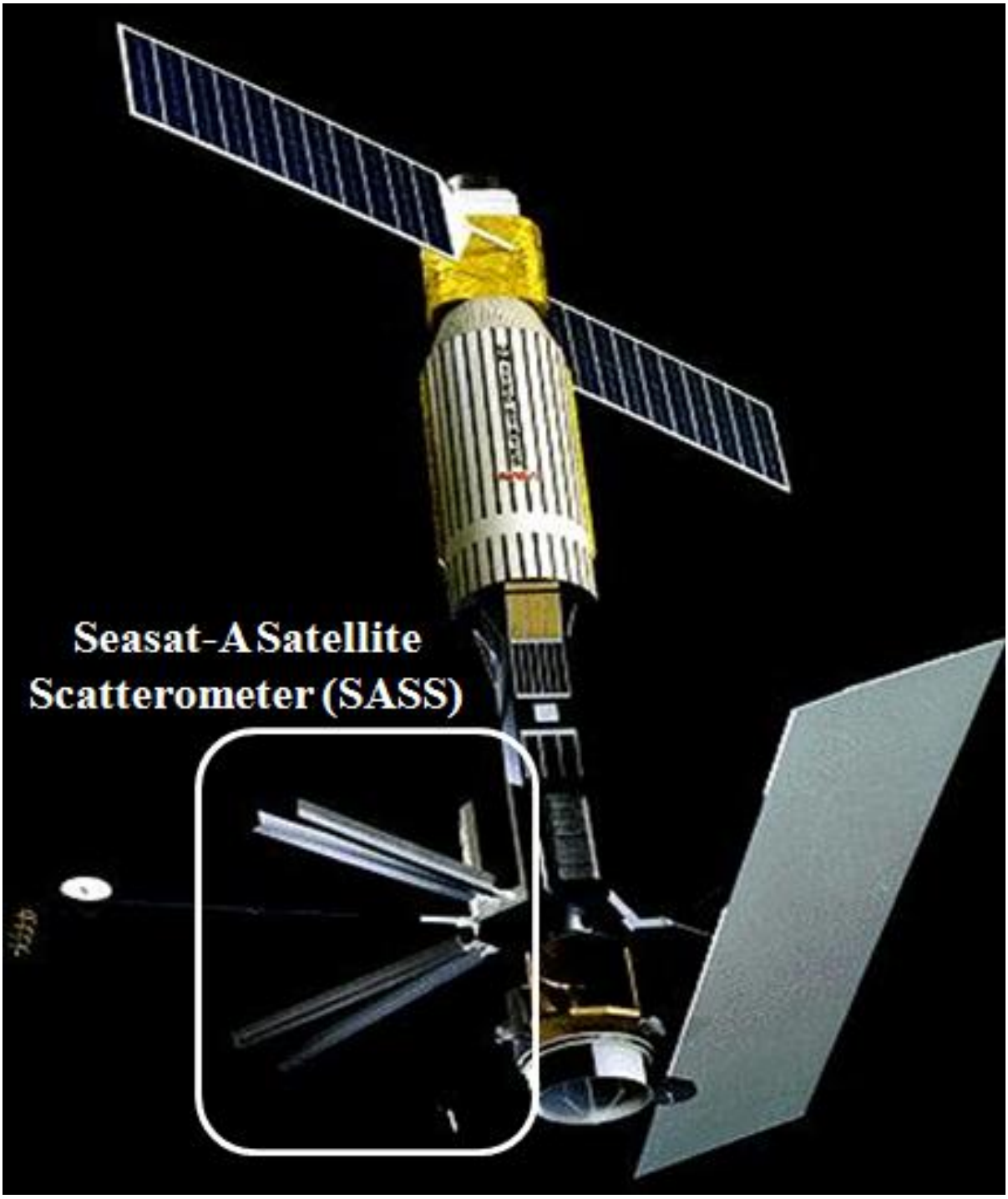


Fig. 1.3: SeaSat-A Satellite Scatterometer (SASS) on SeaSat-A.

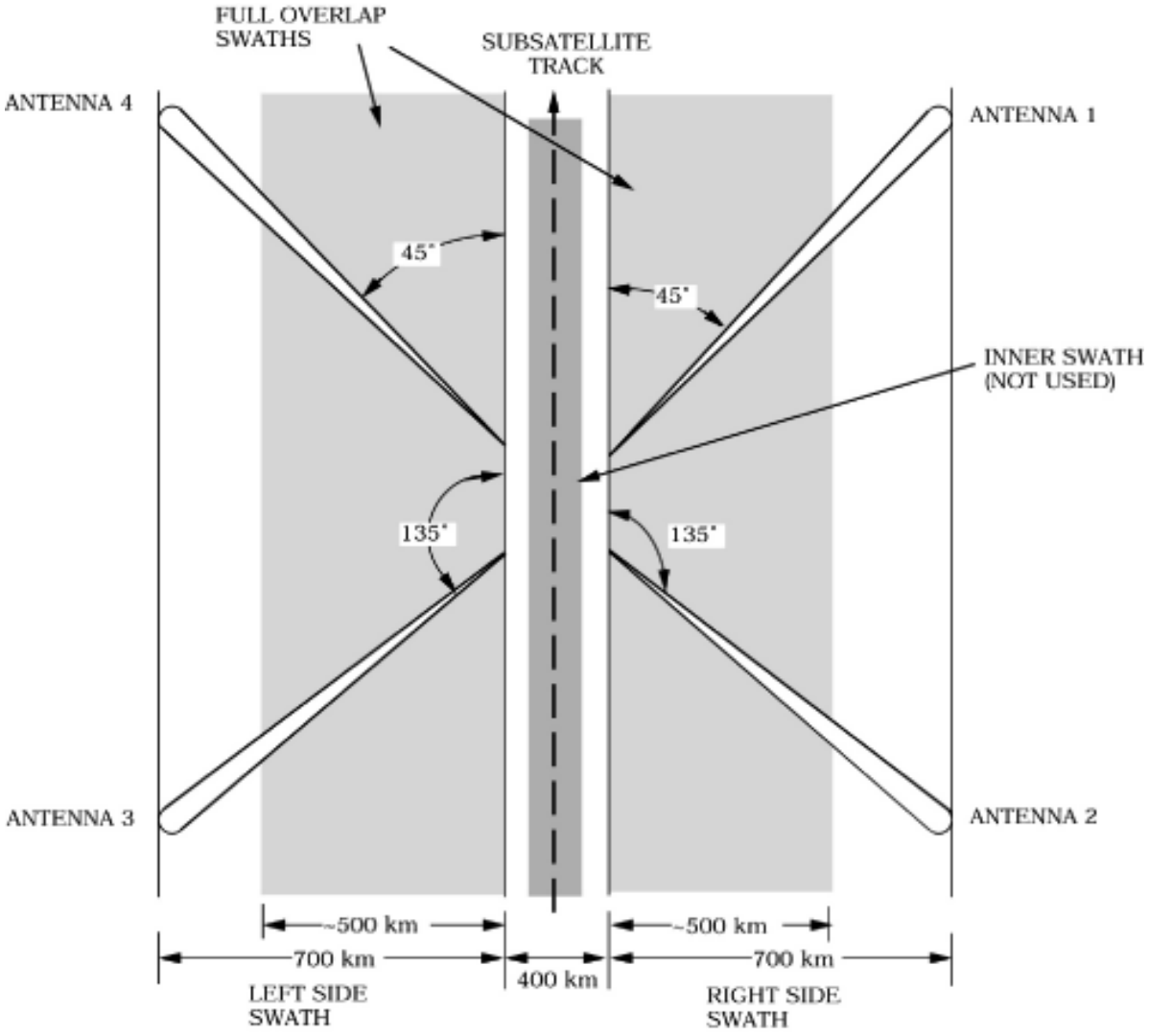


Fig. 1.4: SASS beam configuration and swath coverage (Courtesy of Grantham et al [14]).

### *1.2.3 ESCAT on ERS-1 and ERS-2*

After almost one and a half decades following the success of the SASS, a series of satellite scatterometers were launched; scatterometer coverage continues through present times as illustrated in Fig. 1.1. The first was the launch of the European Space Agency's (ESA) European Remote Sensing Satellite (ERS-1) in 1991. It was equipped with several microwave sensors including: the Active Microwave Instrument (AMI) - a combined C-band (5.3 GHz) SAR/scatterometer, a radar altimeter, an infrared radiometer (IRR), a Microwave Sounder (MWS), and an ultraviolet and visible spectrometer Global Ozone Monitoring Experiments (GOME).

The AMI [15], also referred as the ERS Scatterometer (ESCAT), employed a vertically polarized three-beam antenna and operated at C-band (5.3 GHz). The ESA selected C-band primarily because of the SAR operation; but it also provided an advantage over NASA's Ku-band scatterometer because C-band suffers less rain attenuation and rain volume backscatter effects than does Ku-band [16]. Other than this, the overall wind vector measurement performance is comparable to NASA's Ku-band scatterometers.

In contrast with the SASS, the ESCAT provided only a single-sided 500 km swath offset 335 km from the ground track (Fig. 1.5); but it increased the number of azimuth looks to three to improve the wind direction measurement performance. This idea was originated by NASA

Langley during their post-SeaSat-A design activities for the NASA follow-on scatterometer mission on the National Ocean Observing System (NOOS) [17].

Another difference between AMI and SASS was the method used to sub-divide the fan-beam antenna into wind vector cells. For SASS, Doppler filters were used; but for AMI, short pulses were transmitted and range gates processing was used.

The successor of ERS-1 was ERS-2, a nearly identical spacecraft including an identical AMI scatterometer, which was launched in same orbital plane in April, 1995 and was operated in tandem and passed the same location one day later than ERS-1. They both operated successfully until 2000 when ERS-1 failed; the ERS-2 mission continued for another three years until it was terminated in 2003. Both AMI's operated successfully beyond their design lifespans.

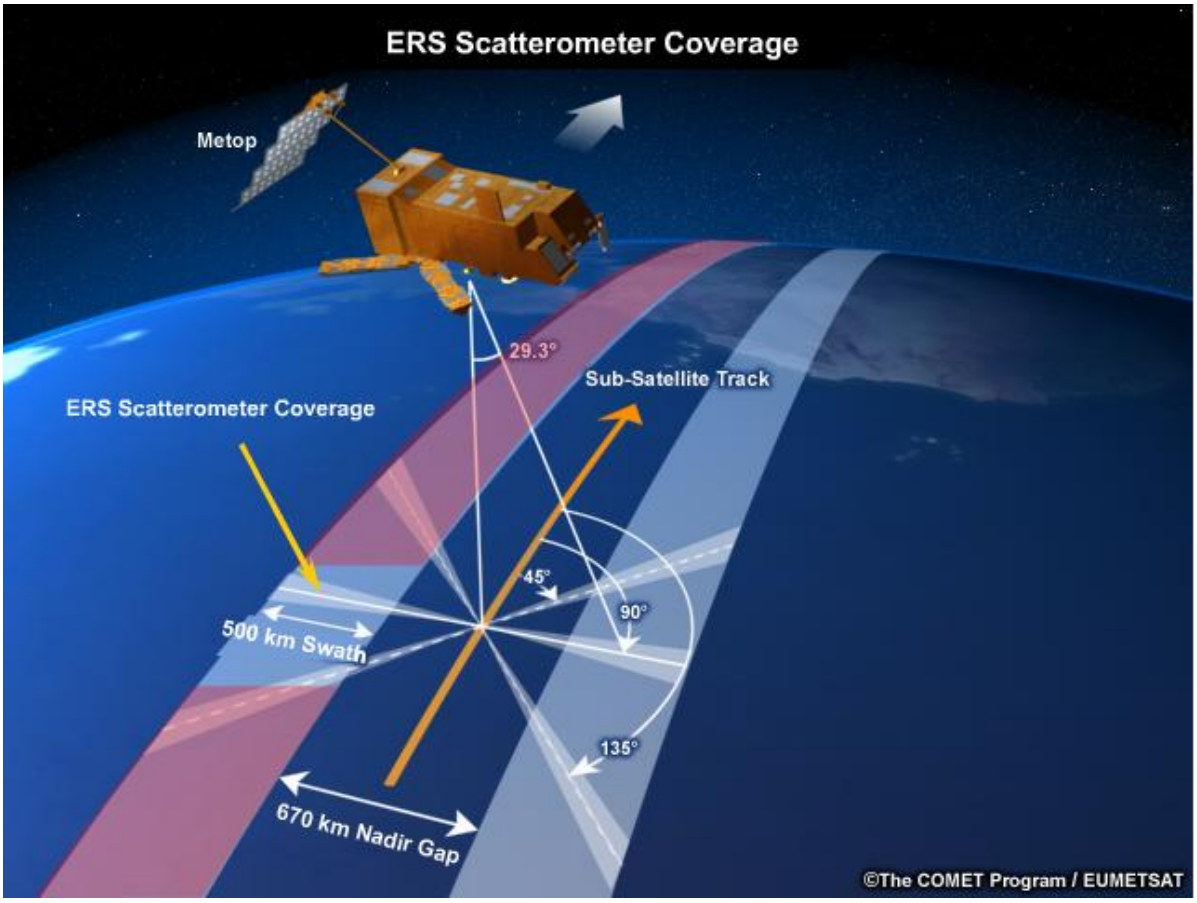

Fig. 1.5: ESCAT on ERS-1 (single blue swath) and ERS-2 (dual swath) measurement geometry.

### *1.2.4 NSCAT on ADEOS*

During the 1980s, the NASA Office of Applications began the development of the improved NASA Scatterometer (NSCAT) at the Jet Propulsion Laboratory (JPL) [18]. This instrument to be flown on the Naval Ocean Remote Sensing Satellite (NORSS) provided an improved Ku-band scatterometer that was based upon lessons learned from SASS. Unfortunately, at the time of the NROSS Program cancellation, the instrument was at the critical design review milestone and (without spacecraft interface definition) could not proceed to flight hardware build. Later in 1988-1989, the NSCAT was selected for flight on Japan's first resources remote sensing satellite, and the instrument flight hardware development was subsequently completed.

In August, 1996, the Ku-band (14.0 GHz) NASA Scatterometer (NSCAT) was launched onboard the Japanese Aerospace Exploration (JAXA) Advanced Earth Observing Satellite (ADEOS), also called "Midori". The NSCAT was the first dual-swath, scatterometer to fly in space since SASS. Its primary science objective was to measure surface wind speed and direction over the global oceans, with a requirement to provide > 90% coverage every two days under all weather conditions. Unfortunately, the ADEOS Mission suffered a premature fatal power system (solar array) failure, which terminated the mission after only 42 weeks (September, 1996 – June, 1997) [18]. During this period, the NSCAT instrument operated continuously without any anomaly and had produced approximately nine months of valuable global ocean surface wind vectors for the NASA ocean sciences community, which lead to many scientific advances in oceanographic and climate research [19].

The NSCAT was a 14 GHz (Ku-band) dual-swath scatterometer, that provided off-nadir ocean sampling in two 600 km swaths on both sides of the satellite sub-track, separated by an approximately 350 km "nadir gap". Unlike SASS with four fixed azimuth beams (Fig. 1.4), NSCAT inserted the two extra side-looking fan-beam antennas, two at ±45° relative to cross-track with vertical polarization and a third dual-polarized (V- & H-pol) beam at 20° between these directions, as shown in Figs. 1.6 and 1.7. This configuration improved the ambiguity removal skill [20] and Gonzales and Long reported 99% success for wind speeds exceeding 4 m/s [21]. Another distinctive design feature for NSCAT (compared to SASS) was an on-board digital Doppler radar processor, which was used to form higher spatial resolution (25 km) $\sigma^0$ resolution cells. Electronic Doppler filtering also allowed NSCAT to dynamically adjust center frequencies to compensate for the earth rotation, thereby enabling excellent co-registered measurements at fixed cross-track distances [18].

Because of NSCAT's 14.0 GHz frequency, the ocean $\sigma^0$ measurement was highly sensitive to rain in the propagation path; hence, the retrieved surface wind data measured in rainy regions was likely be degraded. Unfortunately, without a microwave radiometer onboard this spacecraft, it was not possible to reliably estimate the presence of rain in the scatterometer measurements, which occurs globally about 5% of the time.

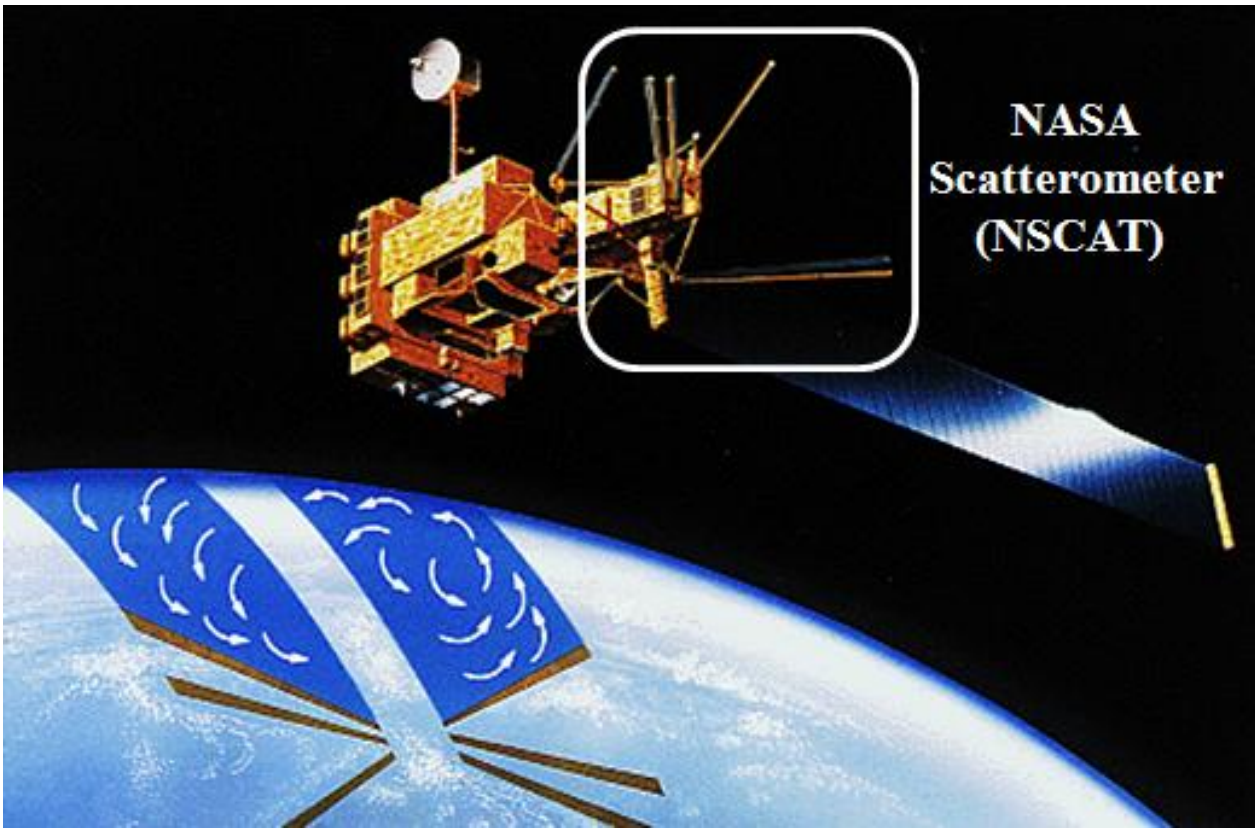

Fig. 1.6: NASA Scatterometer (NSCAT) on ADEOS.

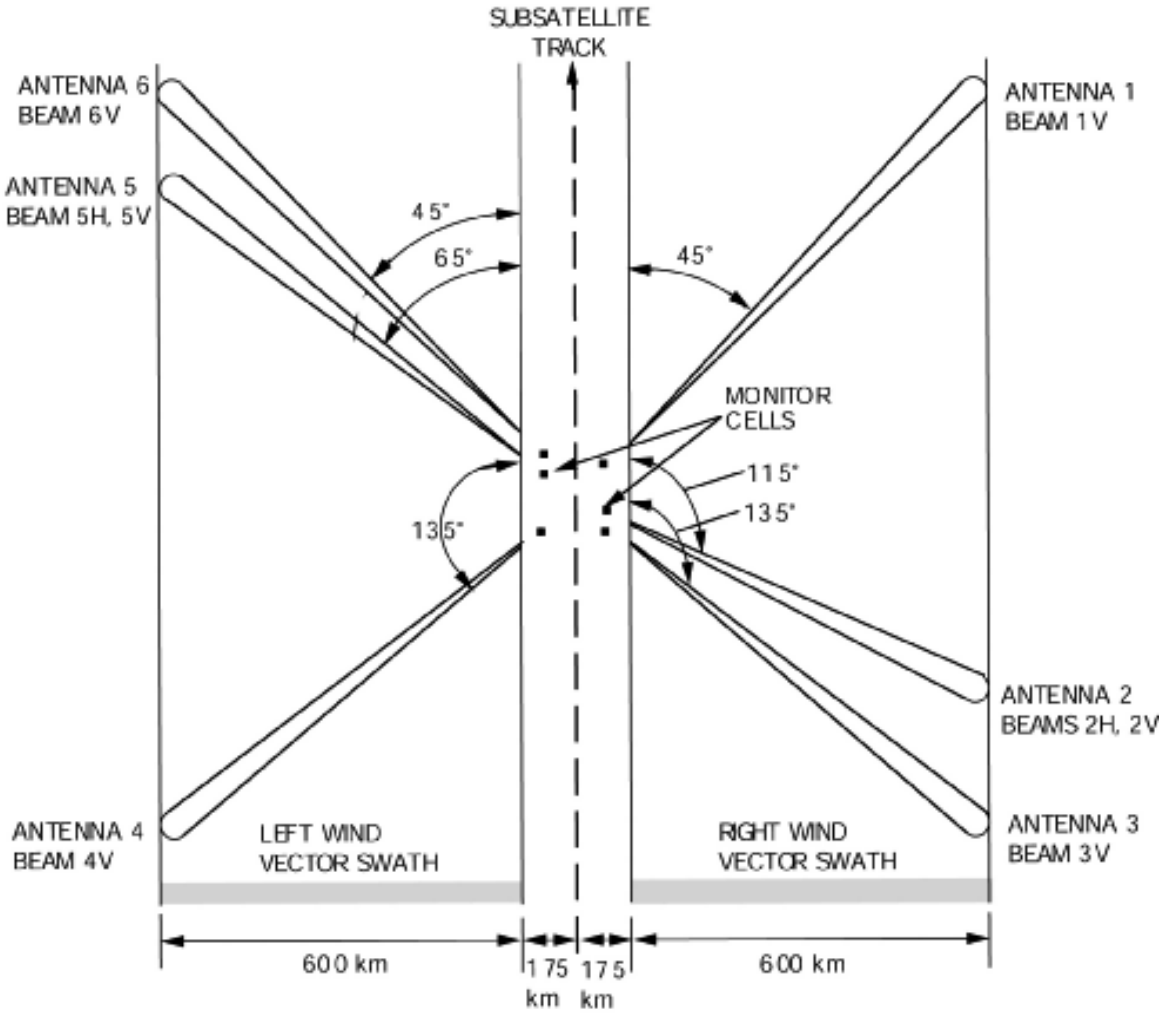


Fig. 1.7: NSCAT scanning geometry (Courtesy of Long and Drinkwater [22]).

### *1.2.5 SeaWinds on ADEOS-II and QuikSCAT*

ADEOS-II was the follow-on to JAXA's earth observing ADEOS-I mission; but with a new payload of sensors. The major change in the instruments was the addition of the JAXA Advanced Microwave Scanning Radiometer (AMSR), which occupied the location previously used by the NSCAT. Because of this, the NASA JPL designed a new conical scanning scatterometer, which could be more easily accommodated because of the smaller compact mechanical antenna design. This instrument, known as SeaWinds, was originally planned to launch three years after ADEOS-I. But because of the premature failure of ADEOS-I, delays in mission development postponed the launch to considerably later.

To mitigate the loss of this flight opportunity, NASA developed a substitute "quick recovery" mission to fill the gap between the demise of ADEOS-I and launch of ADEOS-II. This mission, named QuikSCAT, was launched on June 19$^{th}$, 1999. It carried exclusively the SeaWinds scatterometer flight unit [23], which was originally built to fly on ADEOS-II. QuikSCAT operates in a 803 km altitude, 98.6° inclination (retrograde) orbit as shown in Fig. 1.8. The satellite completes a full revolution (rev) in 100.9 minutes, and the earth's rotation underneath the orbit results in a measurement gap created between orbits.


Fig. 1.8: QuikSCAT swath coverage for 6 hours period (approximately 4 revs).

The science objectives of the QuikSCAT missions are:

- Acquire all-weather measurements of near-surface winds over global ice-free oceans
- Investigate air-sea interaction mechanisms and ocean response on various spatial and temporal scales
- Study long-term rain forest vegetation changes
- Study daily/seasonal sea-ice edge movement and Arctic/Antarctic ice pack changes

During late 2002, JAXA launched its successor of the ADEOS-I (Midori), ADEOS-II (Midori-II). Since the SeaWinds flight model originally intended for flight on this satellite was launched on QuikSCAT, the refurbished engineering model of the SeaWinds became the flight model for ADEOS-II. For approximately seven months, two SeaWinds scatterometers operated in tandem orbits to provide unprecedented high temporal and spatial sampling of global OVW's. Regrettably, due to a solar panel malfunction of the spacecraft, the mission was prematurely terminated ten months after launch despite a fully functional scatterometer.

SeaWinds is NASA's only presently operating radar scatterometer for the measurement of global ocean surface wind vectors. The radar is a conical scanning system, which operates at a Ku-band (13.46 GHz), measuring normalized ocean radar backscatter over a wide swath. It employs a conically scanning 1-meter antenna with two linear-polarized beams (feeds): inner beam H-pol at 46° incidence angle and outer V-pol at 54° incidence angle, as shown in Fig. 1.9. The outer swath is approximately 1800 and overlapped (inner) swath is 1400 km (not shown). The

measurement of ocean $\sigma^0$ with azimuthal diversity (multiple azimuth looks) enables the scatterometer to infer corresponding ocean surface wind speeds and wind directions. Outside of this overlapping region, forward and aft V-pol measurements from the outer antenna beam extend the swath by ± 200 km.

The SeaWinds has significant measurement geometry differences compared to the previous fan-beam scatterometers (SASS, NSCAT and ERS-1 & -2), where antenna azimuth angles are fixed. The over lapping scanning produces a variable azimuthal separation depending upon the cross-swath distance, which increases the complexity the OVW retrieval algorithm. On the other hand, it is advantageous in that the conical scanning provides significantly wider contiguous coverage and eliminates the objectionable nadir gap in measurements.

Each transmitted pulse projects an elliptical instantaneous field of view (IFOV) on the earth surface, which is limited by the 3-dB antenna power beam width footprint of 24 × 31 km (inner beam) or 26 x 36 km (outer beam). The IFOV is subdivided using range gate processing to produce an approximately 4-km width $\sigma^0$ "slice", and the combined $\sigma^0$ is known as an "egg" as shown in Fig. 1.10.

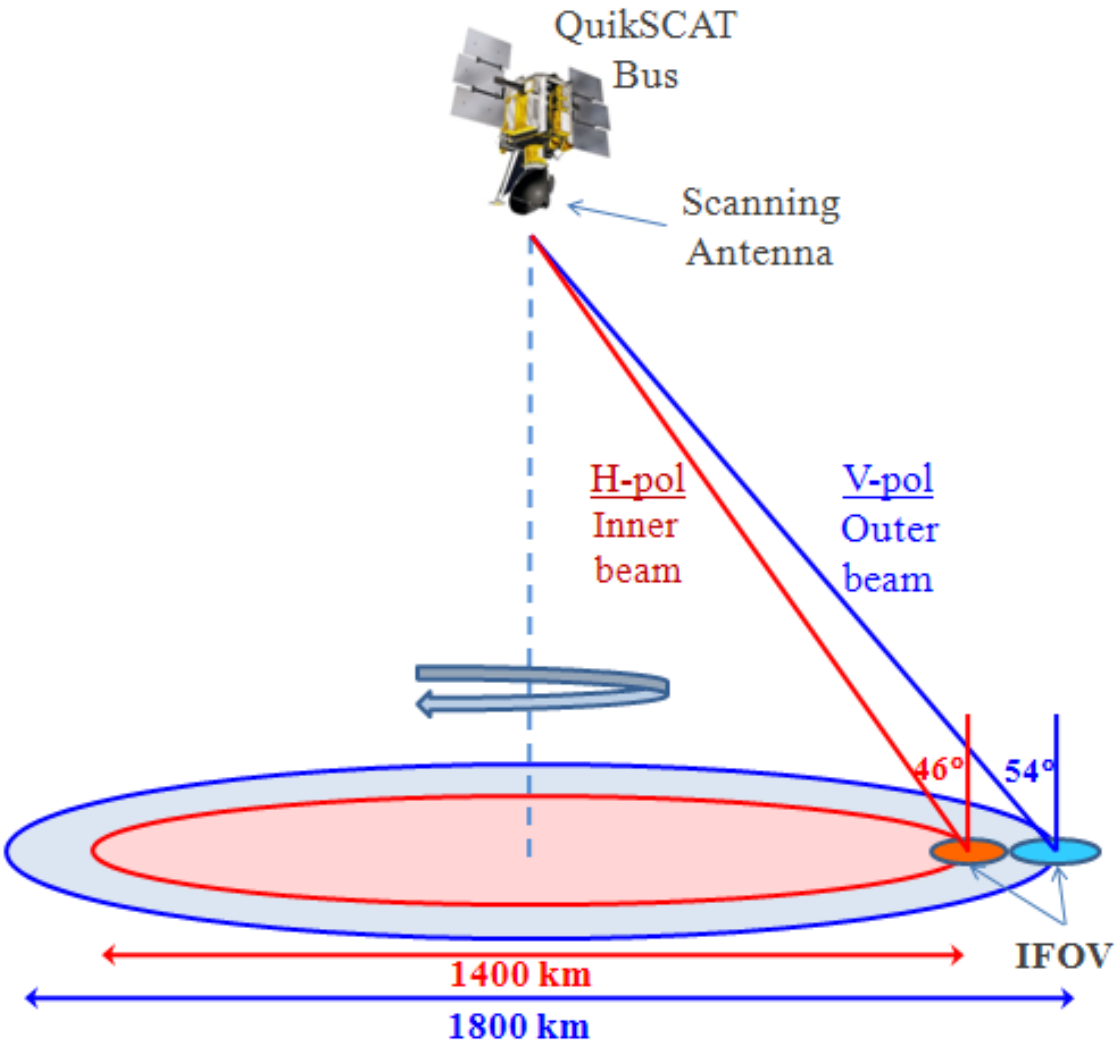


Fig. 1.9: SeaWinds on QuikSCAT conically scanning geometry.

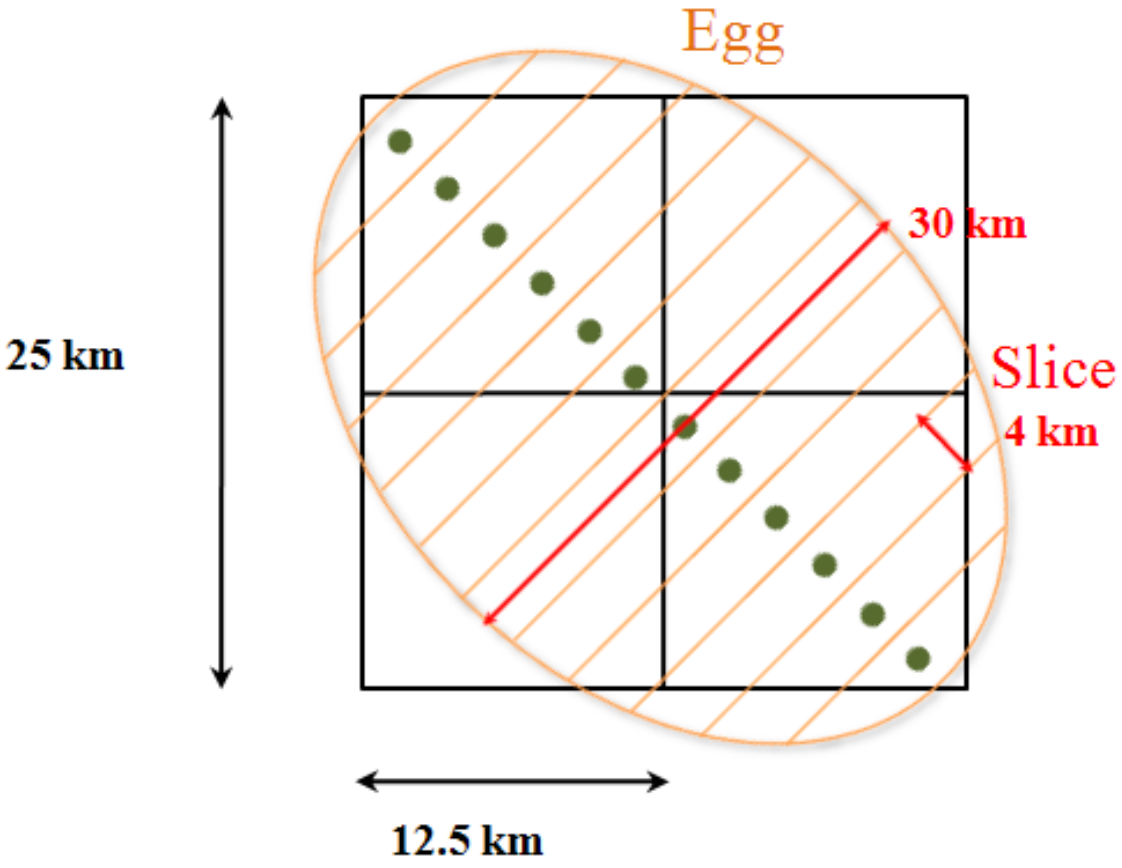


Fig. 1.10: SeaWinds' Sigma-0 resolution elements (eggs and slices).

SeaWinds conical scan geometry (Fig. 1.11) was designed to provide overlapping measurements for each latitude/longitude (25 × 25 km) box, known as a wind vector cell (WVC). These multiple observations of the ocean $\sigma^0$'s are measured from two beams (looking both forward and aft); and this results in four azimuth look observations at each WVC. Considering a given cross-swath WVC location (Fig. 1.12), ocean backscatter is first measured by the outer beam (V-pol) during the forward scan portion at time $t_1$ (red arc). This is shortly followed by the inner beam (H-pol) forward scan at $t_2$ (blue arc). Several minutes later, the measurement is made from the inner beam from aft scan segment at $t_3$ (magenta arc). Finally, the aft-look outer beam at $t_4$ (green arc) is measured. These four-azimuth look ocean $\sigma^0$'s are known as "4-flavors" and they provide an overlapping swath of approximately 1400 km wide. The scatterometer measurement timing is such that the IFOV's overlap in the along-scan direction by 50%, and the antenna spin rate provides 50% overlap in the along-track direction (scan-to-scan).

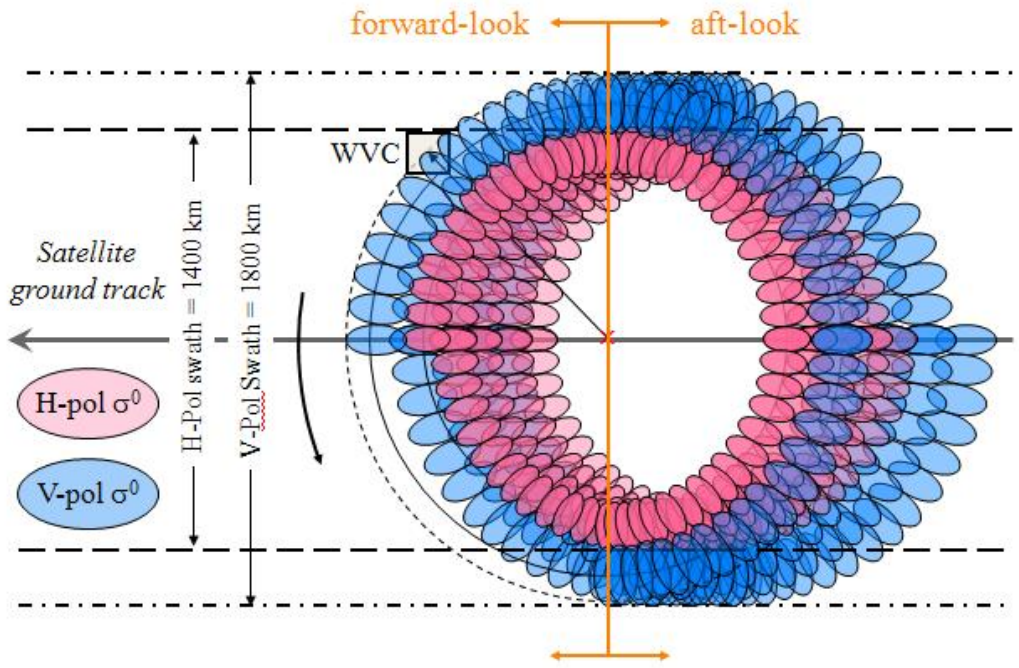


Fig. 1.11: SeaWinds conical scanning geometry.

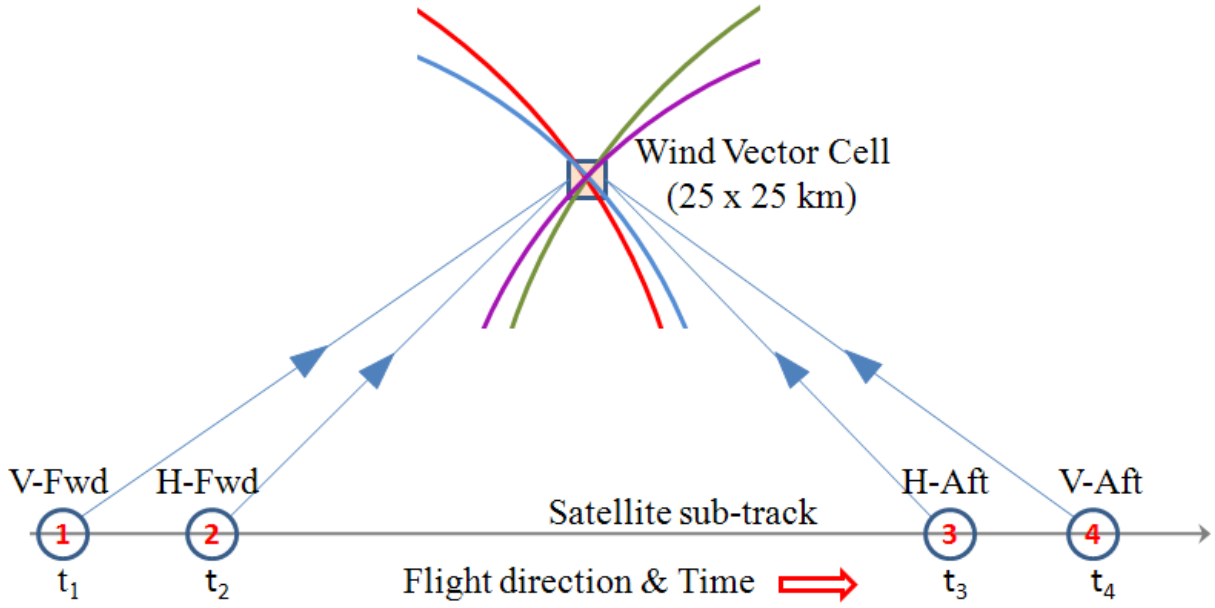


Fig. 1.12: QuikSCAT 4-flavor $\sigma^0$ measurements for one wind vector cell location.

### *1.2.6 ASCAT*

The most recent scatterometer mission, the Advanced Scatterometer (ASCAT), was launched in 2006 on the European Meteorological Operational (MetOp) satellite. This C-band scatterometer is the sequel instrument to ERS-1 and ERS-2, and its mission is to measure OVW to study ocean climate and tropical vegetation. The ASCAT system geometry is based on the fan-beam configuration with incidence angle ranges from 25° to 65° providing two 550-km separated swaths. Each swath is made up of observations taken sequentially from fore-, mid- and aft-antennas. The ASCAT measures ocean $\sigma^0$ from three different azimuth angles and determines wind vector using a GMF.

ASCAT is a C-band real aperture radar operating at 5.255 GHz with two 3-m long antennas with a fixed "V-shaped" positions at ±135° with respect to the spacecraft flight direction. It subdivides the fan-beams by using pulse compress range gates. The two sets of three antennas allow simultaneous observations to be made from three directions in each of its two 550 km-wide swaths as shown in Fig. 1.13. This geometry provides better resolution and over twice the coverage of its predecessors (ESCAT on ERS-1 and ERS-2) and achieves near global coverage in five days.

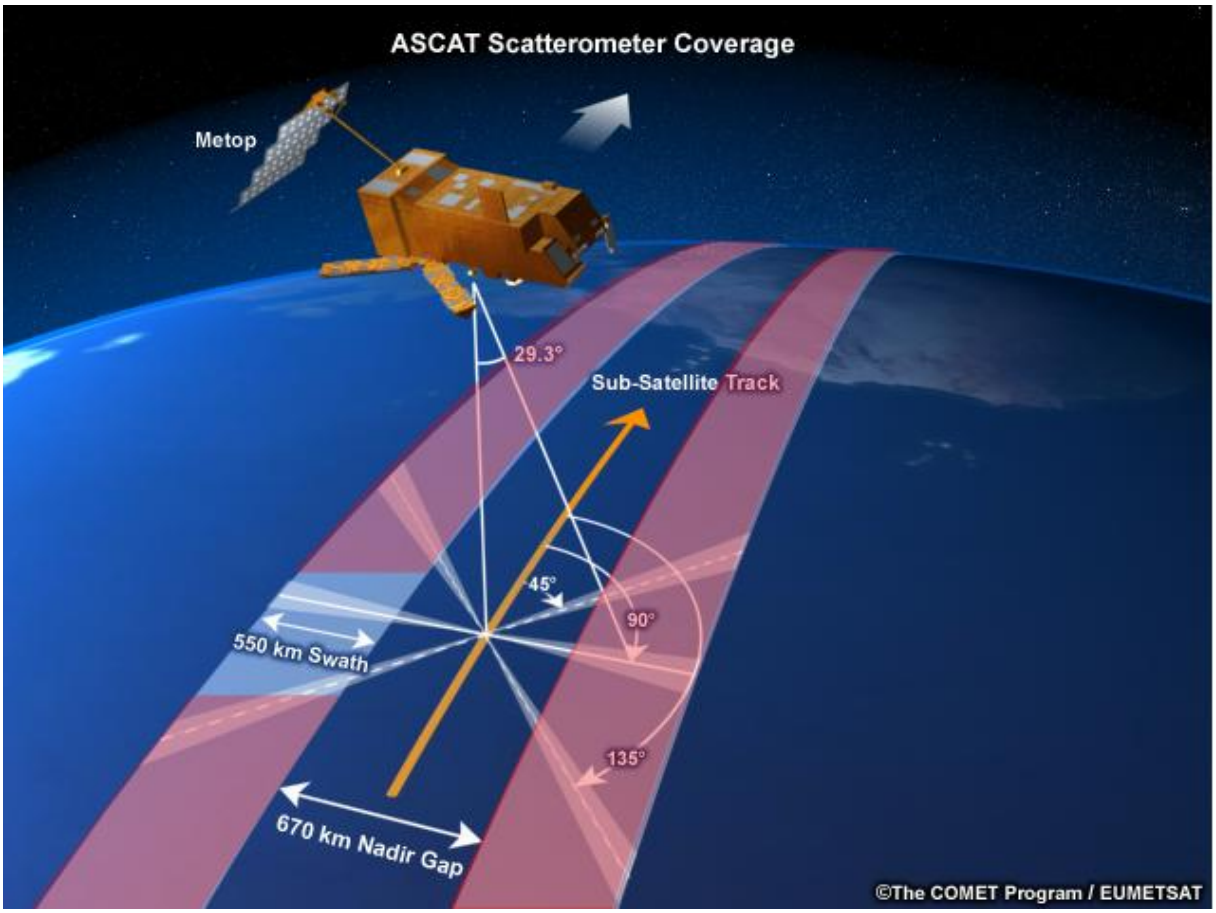


Fig. 1.13: ASCAT scanning geometry.

## 1.3 Current Scatterometer Limitation for Hurricane Measurement and Requirement for Ocean Surface Vector Winds

Satellite scatterometry has evolved considerably in the past three decades; and the most recent JPL conically scanning pencil-beam design offers much higher signal-to-noise ratio (SNR) and wider swath coverage with a lighter and smaller instrument than the previous fan-beam scanning configuration [24]. This conical scanning technique also provides measurements at a constant incidence angle that results in a constant IFOV at all scan positions. SeaWinds achieves wind speed error accuracies of < 2 m/s and wind direction error < 15° [25]. Presently, the SeaWinds on QuikSCAT is the only pencil-beam conical scan scatterometer operating.

With regards to hurricane retrievals, QuikSCAT has three major issues [3]:

1. Uncertainty in the measured ocean backscatter due to precipitation,
2. The measured ocean normalized radar cross section at Ku-band begins to severely saturate beyond wind speeds of approximately 30 m/s, and
3. The instrument spatial resolution is not adequate to resolve small-scale storm structure associated with tropical cyclones.

Furthermore, the instrument was designed for global synoptic-scale average wind measurements and not especially tailored to the high spatial gradients of extreme wind events. Future scatterometer designs will address this instrument design shortcoming [26]. However, a significant improvement can be accomplished with the existing SeaWinds instrument, namely a

new special OVW retrieval algorithm that improves the accuracy of the ocean surface wind vectors in extreme wind events.

The objective of this research is to improve the state-of-the-art for scatterometer wind retrieval for hurricane measurements (and other extreme wind events). This dissertation documents the development of a stand-alone hurricane measurement algorithm using the QuikSCAT scatterometer, named "Q-Winds". The next subsection presents a brief history of ocean wind vector retrieval, which addresses the current scatterometer limitations and summarizes ocean surface vector winds requirements for scientific and operational users.

## 1.4 Dissertation Objective

The purpose of this dissertation is to develop an improved OVW retrieval algorithm for hurricanes and to validate the algorithm with independent hurricane OSVW measurements. This dissertation is organized into five chapters. Chapter 1: Introduction, has covered the history and literature reviews of the space-borne active microwave wind retrieval and the requirement for hurricane OVW measurements. Chapter 2: Hurricane Wind Measurements, describes remote sensing airborne and satellite wind measuring techniques and the surface truth used in Q-Winds algorithm validation. Chapter 3: Hurricane Wind Vector Retrieval Algorithm "Q-Winds", which is the essence of this dissertation, describes an improved hurricane retrieval algorithm using QuikSCAT. Chapter 4: Results, presents results of performance evaluation and comparison to surface truth. Finally, Chapter 5: Discussion and Conclusion, summarizes conclusions, and presents possible scope of future works.

# CHAPTER-II: HURRICANE WIND MEASUREMENTS

The objective of this chapter is to provide a brief overview of the NOAA's responsibility for TC surveillance and warnings, including a discussion of airborne measurements and surface wind field analyses used in hurricanes and the SeaWinds scatterometer data products. The TC forecast centers use these measurements for both operations and research to analyze and study the characteristics of the storm. The primary data used in this dissertation are from the SeaWinds scatterometer on QuikSCAT satellite (algorithm development) and the H*Wind surface analyses (algorithm validation), which are available for Atlantic Ocean, Gulf of Mexico, and Caribbean Sea.

## 2.1 Tropical Cyclone Surveillance and Warning Organization Responsibility

TC warnings and forecast services are the cooperative efforts of several departments and federal agencies. NOAA under the Department of Commerce (DOC) is responsible to provide TC warnings and forecasts for the Atlantic and Eastern and Central Pacific Oceans and the Department of Defense (DOD) is responsible for Western Pacific and Indian Oceans.

Researches regarding to TC studies are conducted in NOAA, the U.S. Navy, and NASA to improve TC forecast accuracy. The NOAA is one of the federal government agencies responsible for studying Earth's environment and managing environmental resources. One of the major tasks

that NOAA undertakes is the monitoring and issuing of warnings for Atlantic hurricanes through its operational organization, the Tropical Prediction Center and the National Hurricane Center in Miami, Florida. The area of responsibility for TC is shown in Fig. 2.1.

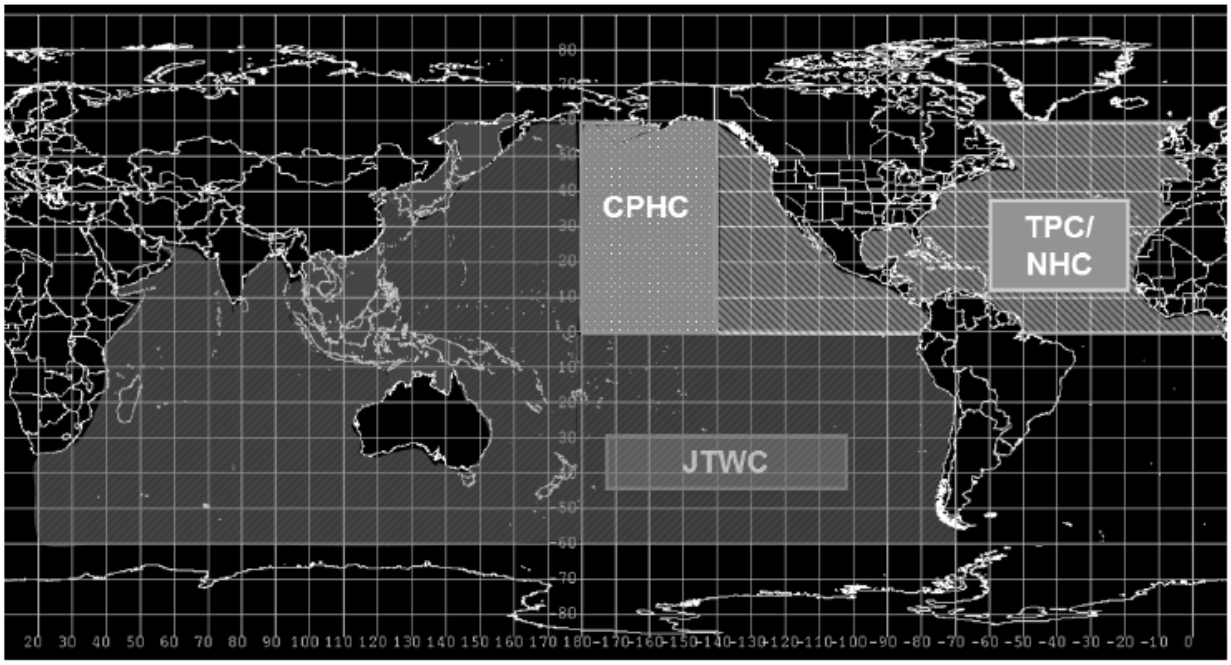


Fig. 2.1: Tropical Cyclone Forecast Center's Areas of Responsibility.

Regarding the TC's in U.S. territory, Gulf of Mexico, and Caribbean Sea areas, the DOC (through NOAA) is charged with the overall responsibility to provide forecasts, warnings, and necessary information to the appropriate agencies and the general public. DOC, with support from DOD, Department of Transportation (DOT), and the Department of Homeland Security (DHS)/U.S. Coast Guard (USCG), implements appropriate actions and utilizes the federal resources for storm forecasting. The aircraft reconnaissance is routinely used for TC monitoring. Three different research aircraft (WC-130J, G-IV, and NOAA P-3 in Fig. 2.2) are dedicated for TCs observation once the storms approach landfall. They are well-equipped for hurricane wind

and environmental parameters measurements which include: flight-level data sensors, airborne radars (tail Doppler), cloud physics instrumentation, expendable wind sensors (dropwindsondes and drifting buoys), and remote sensors (Stepped Frequency Microwave Radiometer (SFMR) and C-band scatterometer) [27].


Fig. 2.2: Reconnaissance and surveillance aircraft used in TC operation. Top is the WC-130J and at bottom are two Gulfstream-IV (front), and WP-3D (back).

## 2.2 Hurricane Wind Speed Measurement Scale

When the storm intensity exceeds tropical storm strength (33 m/s; 64 kts) wind speed exceeds 74 mph, it becomes a hurricane. Hurricane and the one-minute sustained surface intensities can be classified by the Saffir-Simpson Hurricane Scale (SSHS). The SSHS divides hurricane into five categories (Category-1 to Category-5) distinguished by the intensity of the sustained winds. The SSHS is presented in Table 2.1.

Table 2.1. Saffir-Simpson Hurricane Scale

| Storm Class | m/s | mph | kt | km/h |
|---|---|---|---|---|
| Tropical depression | 0-17 | 0-38 | 0-33 | 0-62 |
| Tropical storm | 18-33 | 39-73 | 34-63 | 63-117 |
| 1 | 34-43 | 74-95 | 64-82 | 119-153 |
| 2 | 44-49 | 96-110 | 83-95 | 154-177 |
| 3 | 50-58 | 111-130 | 96-113 | 178-209 |
| 4 | 59-69 | 131-155 | 114-135 | 210-249 |
| 5 | ≥ 70 | ≥ 156 | ≥ 135 | ≥ 250 |

## 2.3 Airborne Systems for Hurricane Wind Measurements

Several approaches have been used to measure hurricane-force wind; but because of TC's violent surface conditions, some of the conventional surface wind measuring techniques, e.g., buoys or ships, are not useful for operational hurricanes measurement. Fortunately, a few airborne instruments are applicable for extreme wind events, and they provide very useful data for NOAA hurricane forecasters.

Airborne wind measurements can be subcategorized as *in situ* and remotely sensed. The *in situ* wind instruments ( e.g., dropwindsonde or flight-level sensors) obtain data through direct contact with the airstream. Alternatively, remote sensors such as the scatterometer, radiometer, or tail Doppler radar infer surface wind information by interpreting electromagnetic signatures of the ocean surface (e.g., ocean surface and rain backscatter, Doppler and blackbody emission).

Because of the large spatial scale of the storms (typically on order of hundreds of kilometers), their ferocious conditions, and their remoteness from land, TC observations are sparse. Also because of the expense, reconnaissance aircraft are usually dispatched only when a storm threatens landfall. *In situ* data such as GPS dropwindsondes have high accuracy and are the "standards" for wind velocity measurements; however, they are limited to discrete location. On the other hand, remote sensors provide a much wider area of coverage than the *in situ*

instruments; but both techniques are widely used in hurricane observing systems. The following subsections discuss the major hurricane observation techniques in more detail.

### *2.3.1 Global Positioning System (GPS) Dropwindsondes*

A global positioning system (GPS) dropwindsonde, or often referred as "dropsonde" for short, is an *in situ* instrumentation package designed to monitor TC systems [28]. A dropwindsonde comprises a GPS receiver, pressure, temperature, and humidity sensors and a radio transmission system. A dropwindsonde is released from an aircraft at flight altitude at various locations, including the eye-wall and in vicinity of the storm center. They are suspended by a parachute to maximize the observation period before reaching the ocean surface. Real-time data (latitude, longitude, altitude, and environmental data) are transmitted to the monitoring systems with time stamps every 0.5 second. Typically, the lowest altitude of wind measurement occurs at a few 10's of meters above the surface. Wind speeds and directions are then computed from the dropwindsondes displacements, which yields horizontal wind velocity *versus* altitude at a sample rate of 2 Hz. Dropwindsondes provide high quality *in situ* measurements of surface wind speed in extreme conditions; however, only approximately a dozen of GPS dropwindsondes are deployed per a hurricane event; hence, the observation coverage is quite limited.

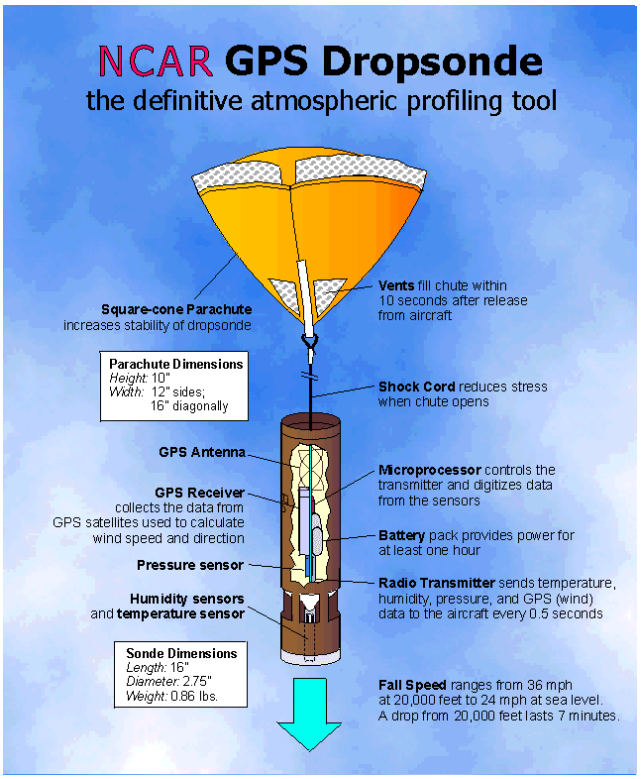


Fig. 2.3: Global Positioning System (GPS) dropwindsondes (courtesy of AOML/NOAA/HRD).

### *2.3.2 Aircraft Flight-Level Winds*

Aircraft flight-level wind observations, typically obtained at the 700 mb (~10,000 ft) level, are calculated as the difference between ground vector motion and air vector motion. The aircraft speed within the flowing air mass is determined by a dynamic pressure anemometer and the direction is recorded as the aircraft heading measured by the compass. The ground vector motion is determined from the GPS or inertial navigation system (INS). The ocean surface wind speed is then estimated by applying a reduction factor to the aircraft flight-level wind speed.

This empirical relationship between flight-level and surface wind has been established from many aircraft flights in hurricanes whereby flight-level wind measurements and collocated GPS

dropwindsonde and buoy observations were obtained. Various surface attenuation ratios, defined as a ratio of flight-level wind speed over surface wind speed, are found in the literature: a ratio of 63%-73% from reconnaissance flight-level wind observations is recommended by Powell and Black [29]; while National Hurricane Center (NHC) suggested a ratio of 80% - 90% of the flight-level wind for operational usages. In view of studies such as Powell and Black, the uncertainty of surface winds from flight-level wind measurements is relatively large.

### *2.3.3 Stepped Frequency Microwave Radiometer (SFMR)*

The Stepped Frequency Microwave Radiometer (SFMR) is a nadir-viewing C-band multi-channel radiometer designed to infer TC surface wind speeds and rain rates. It simultaneously measures microwave emission (brightness temperature) from the sea surface at multiple frequencies between 4.5 – 7.2 GHz. Hurricane one-minute sustained wind speeds are retrieved using the SFMR geophysical algorithm [30] over a wind speed range of 10-85 m/s.

There are approximately a dozen SFMR instruments that are flown on NOAA WP-3D/G-IV aircraft and the US Air Force 53$^{rd}$ Weather Reconnaissance Squadron WC-130J aircraft. A typical installation in a wing-pod is shown in Figs. 2.4 and 2.5. An example of SFMR wind speed and rain rate measurements along with flight-level winds (4 km altitude) are shown in Fig. 2.6.

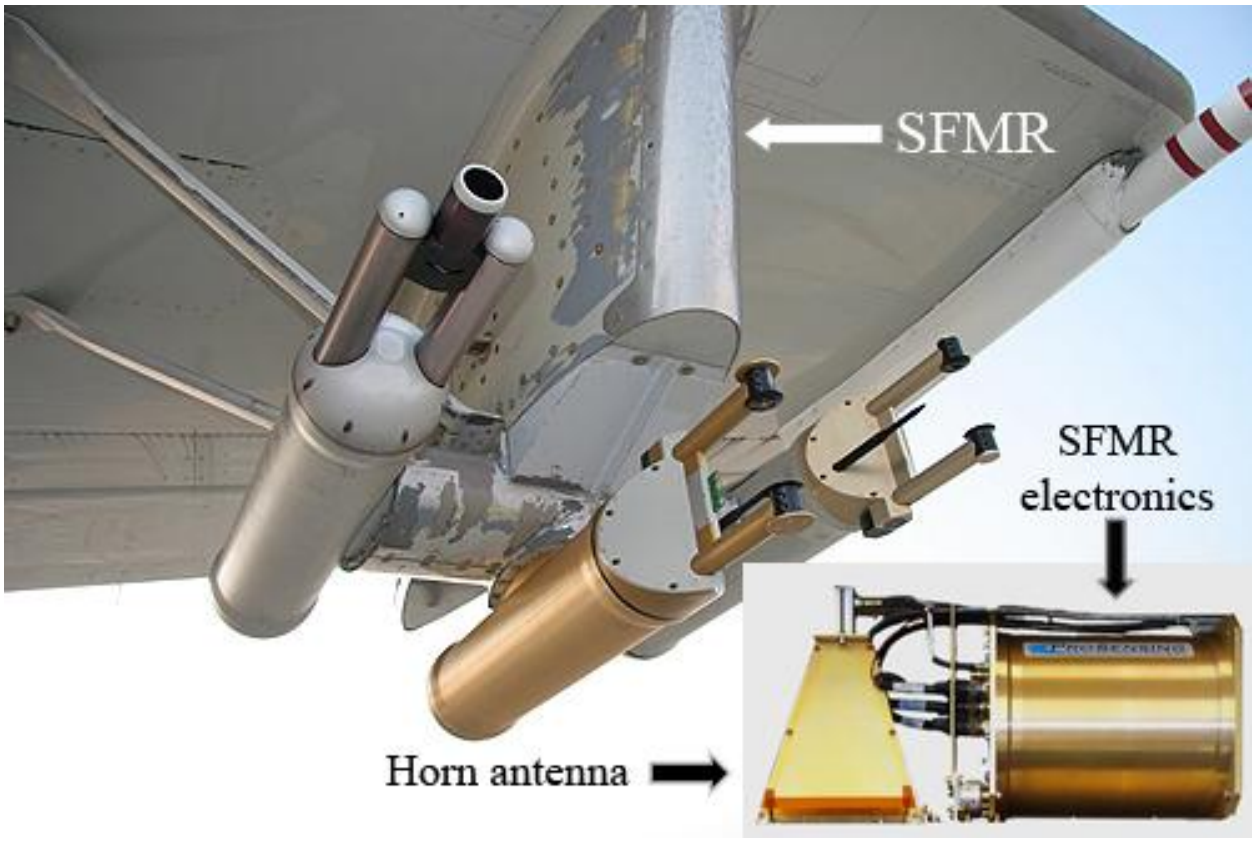


Fig. 2.4: Stepped Frequency Microwave Radiometer (SFMR) on NOAA/HRD WP-3D research aircraft and SFMR electronics hardware (courtesy of AOML/NOAA/HRD).

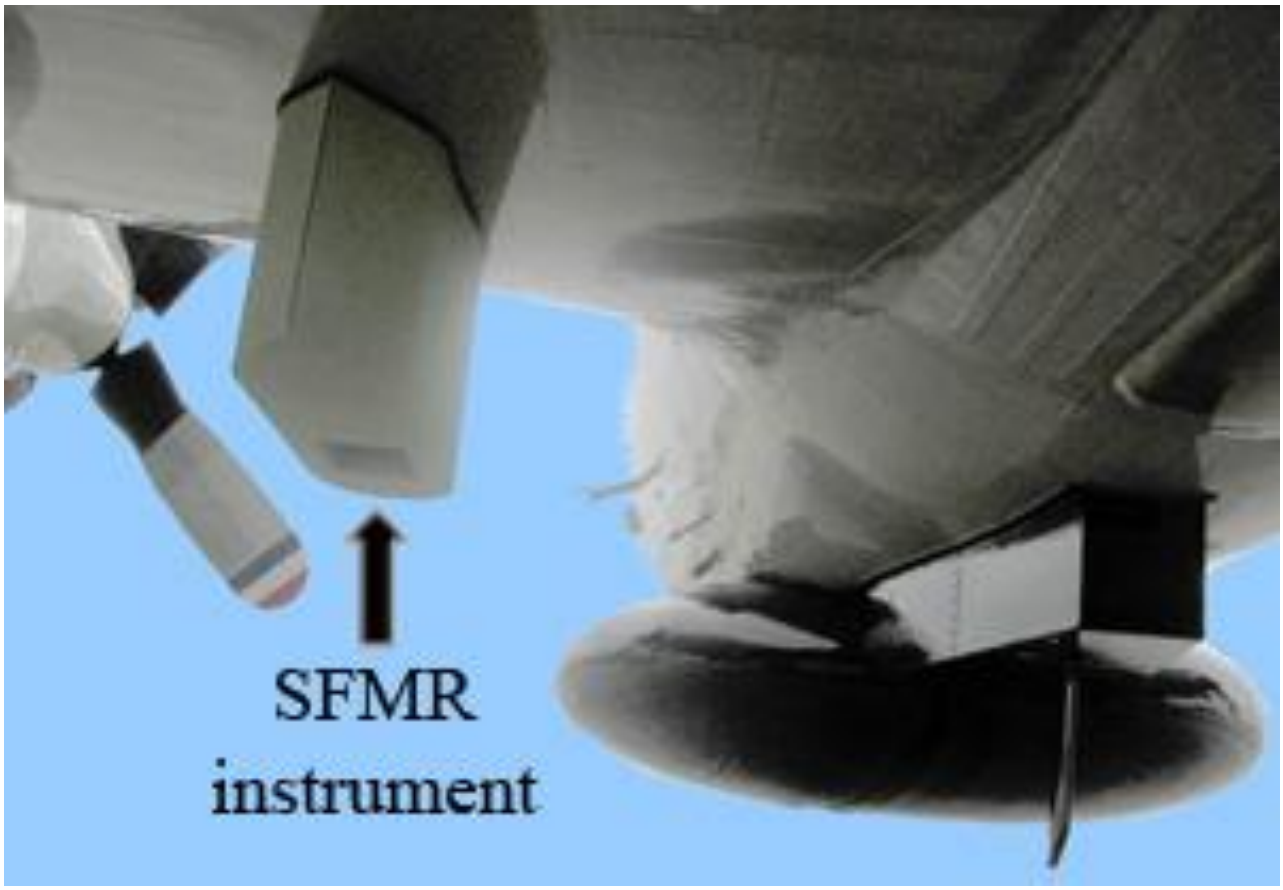


Fig. 2.5: Stepped Frequency Microwave Radiometer (SFMR) on NOAA/HRD WP-3D research aircraft wing-pod (courtesy of AOML/NOAA/HRD).

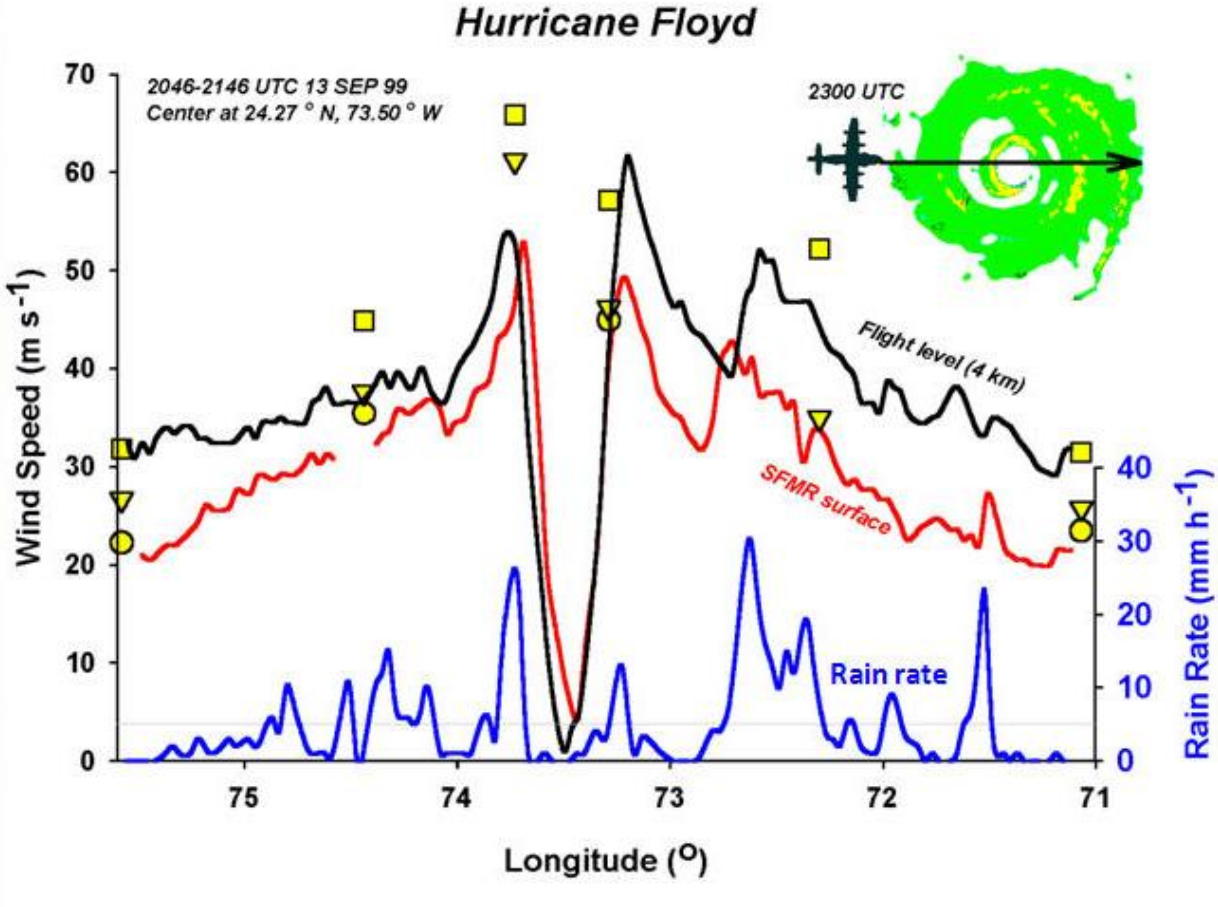


Fig. 2.6: SFMR simultaneous wind speed and rain rate retrieval during Hurricane Floyd (courtesy of AOML/NOAA/HRD).

### *2.3.4 Tail Doppler Radar (TDR)*

The tail Doppler radar (TDR) system, installed on NOAA's Gulfstream-IV (and WD-P3) hurricane hunter surveillance aircraft (Fig. 2.7), acquire three-dimensional (3-D) hurricane core wind field data.

The radar antenna is rotated to map out two conical surfaces (one looking forward and the other looking aft) about the aircraft flight path (see Figs. 2.7 and 2.8).In this manner, the radar can measure radar backscatter from rain drops from the aircraft altitude (above and below) to the surface. Because the rain drops are evicted by the local wind velocity, they become a "tracer" to measure the 3-D wind structure in the max intensity eye-wall and the spiral rain bands which surround the TC. By measuring the raindrops Doppler frequency shift at forward and aft azimuth directions, the horizontal component of wind velocity can be estimated.

An example of reflectivity from the tail Doppler radars is shown in the top panel in Fig. 2.8, and the horizontal section of interpolated reflectivity data with dual-Doppler synthesized wind vectors in the bottom panel of Fig. 2.8. The raw radar data is processed onboard the aircraft through quality control (QC) software developed by NOAA/HRD.

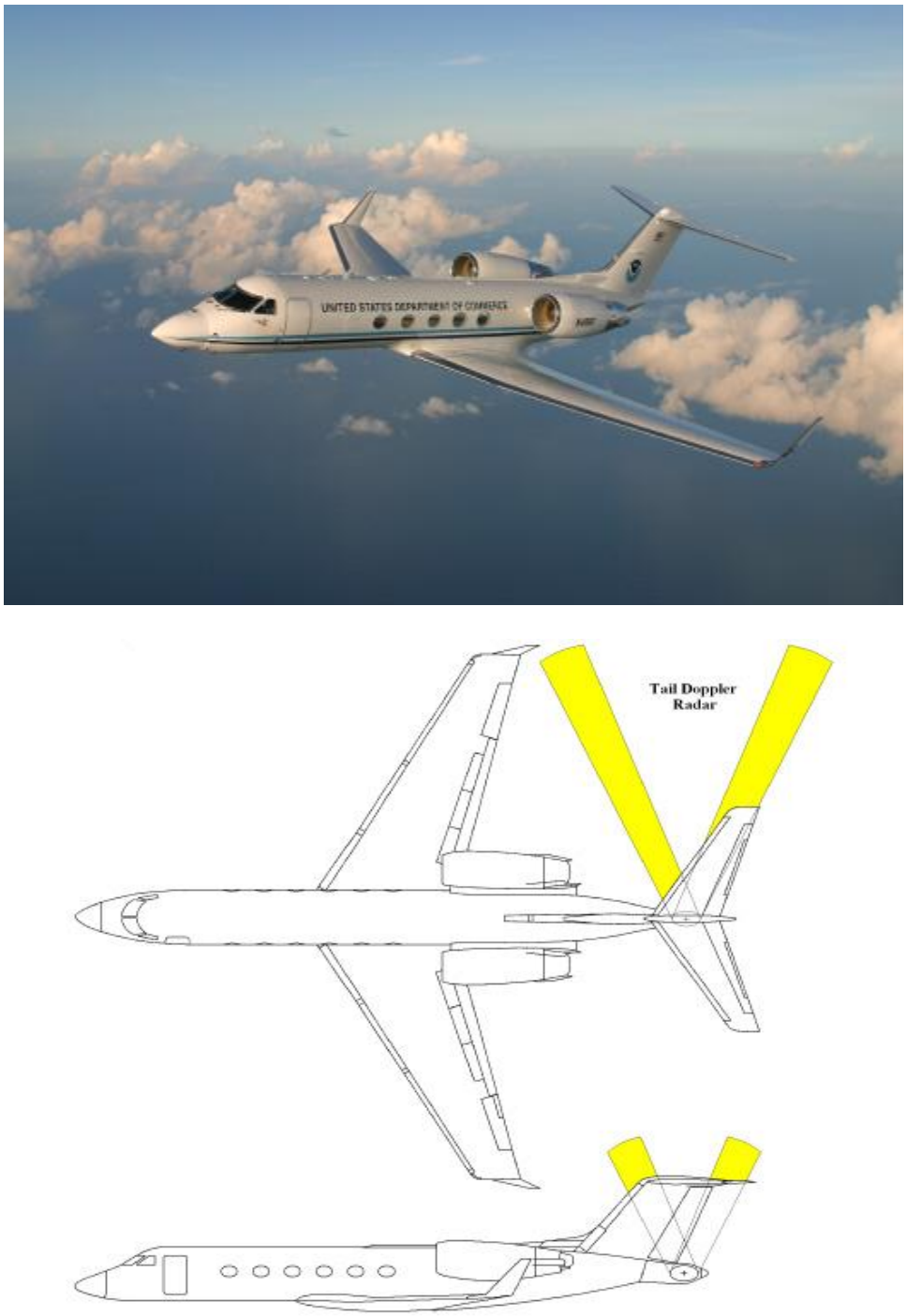


Fig. 2.7: Tail Doppler radar system onboard NOAA's Gulfstream-IV hurricane hunter aircraft (courtesy of NOAA).

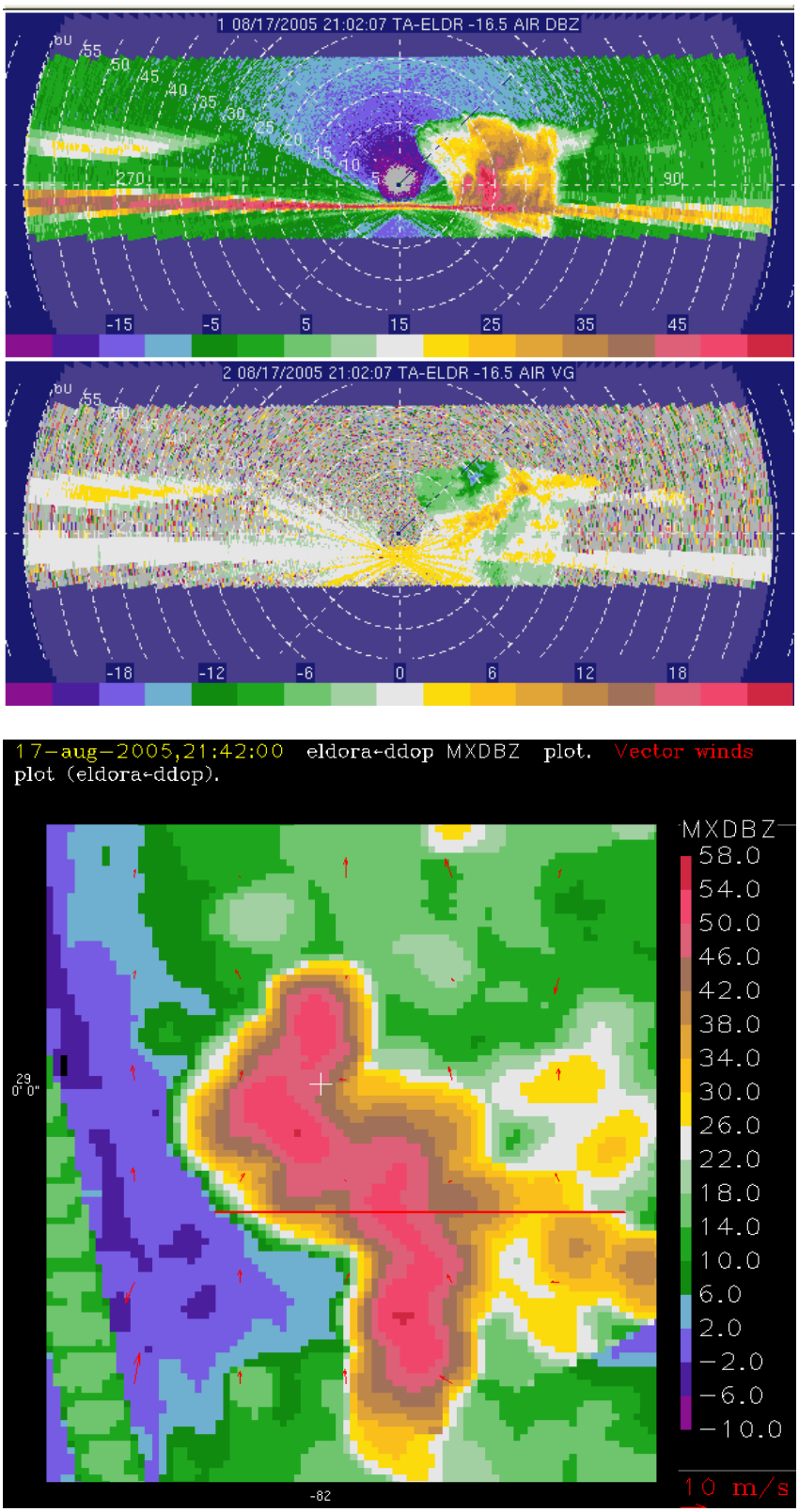


Fig. 2.8: Tail Doppler radar (TDR) reflectivity and wind measurements. Top is TDR reflectivity and bottom is interpolated data and horizontal wind (courtesy UCAR).

### *2.3.5 Imaging Wind and Rain Airborne Profiler (IWRAP)*

The Imaging Wind and Rain Airborne Profiler (IWRAP) [31] is the first high-resolution dual-band airborne Doppler radar designed to study the inner core of the TCs. It is an experimental sensor that operates from a NOAA's WP-3D aircraft during missions through storms.

IWRAP is a down-ward viewing conical scan microwave Doppler radar operating at C- and Ku-band that images the 3-D atmospheric boundary layer (ABL) winds, ocean surface winds, and rain rates. The system was designed to provide high-resolution dual-polarized reflectivity and Doppler velocity profiles of the ABL, as well as ocean surface backscatter at 30-m resolution within the inner core precipitation bands of TCs at four simultaneously separate incidence angles (30°, 35°, 40°, and 50°, see Fig. 2.9). The ocean surface wind vectors are inferred *via* scatterometry, the 3-D ABL wind field *via* Doppler measurements from precipitation, and rain rate is estimated from dual-wavelength differential attenuation.

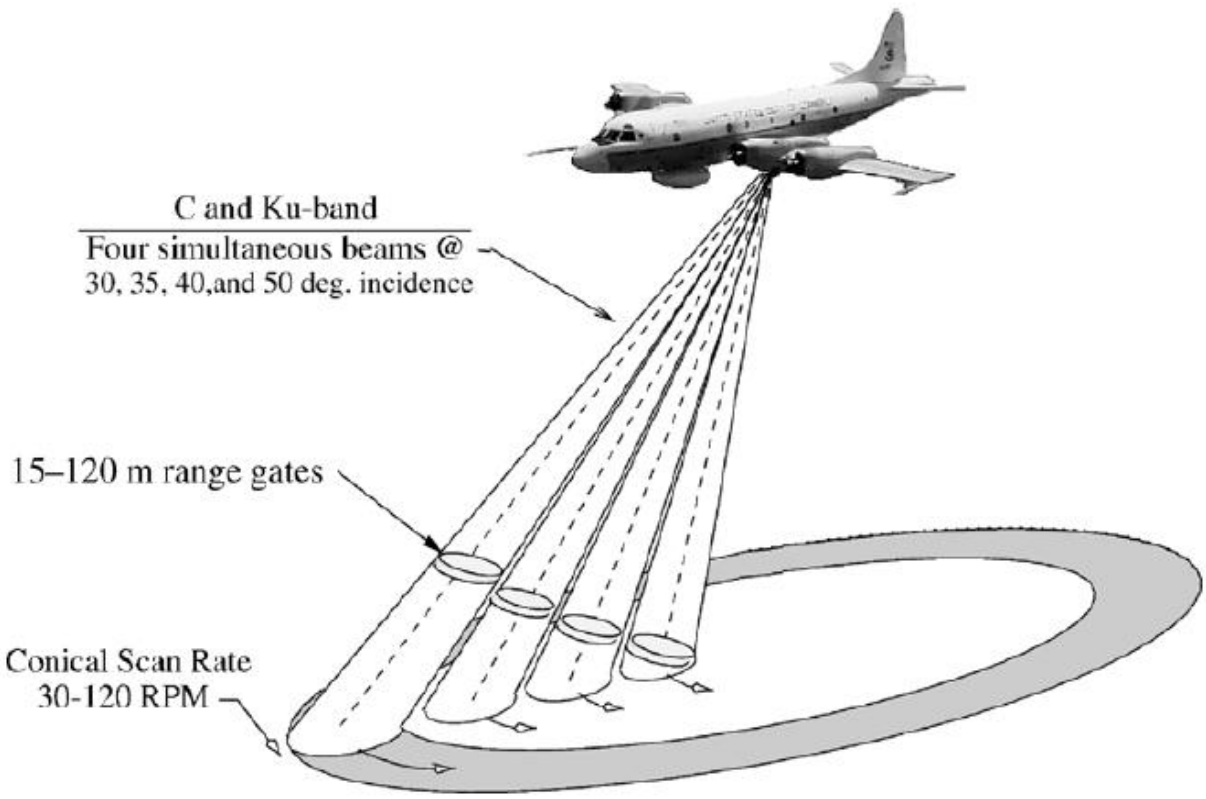


Fig. 2.9: IWRAP measurement geometry (courtesy of Fernandez et al [31].).

## 2.4 H*Wind Surface Analysis

In 1996, an integrated near real-time hurricane analysis tool, called H*Wind, was developed by NOAA Hurricane Research Division (HRD). H*Wind evolved from a series of peer-reviewed, scientific publications [29, 32-34] that analyzed a number of major hurricanes. It is designed to improve the assessment of hurricane intensity and to improve understanding of the extent and strength of the surface wind field. In this research, the H*Wind analysis is used as the "surface truth" for algorithm tuning and independent algorithm validation. A detailed description of H*Wind is provided at http://www.aoml.noaa.gov/hrd/

H*Wind assimilates hurricane wind measurements collected over several hours period from multiple platforms (aircraft and satellite) into a "storm centric" moving TC coordinates system and outputs a snap-shot of the entire TC surface wind field at 6 km resolution. This wind represents the one-minute sustained wind velocity at 10-m altitude reference. Wind measurements used in H*Wind include: SFMR wind speeds, GPS dropwindsondes, tail Doppler radar, geostationary operational environmental satellite (GOES) cloud track winds, and satellite observations (such as QuikSCAT, WindSat, and ASCAT).

Because of satellite tremendous ground speed and wide swath coverage, the entire view of storm can be measured almost instantly. Unlike the aircraft sensors which require several hours to gather adequate TC winds information. Thus, satellite observation is very useful for H*Wind to

estimate peripheral winds of the hurricane and is usually included as an input. However, since H*Wind is used to validate an algorithm based on QuikSCAT in this dissertation; therefore, H*Wind analyses used here are do not include any QuikSCAT measurements.

H*Wind accuracy is highly depends on the quality of the dataset and data coverage. Although it is imperfect, it is the current best surface truth available and is used as the "surface wind comparison dataset" for algorithm tuning and evaluation. An example of H*Wind output is presented as a wind barbs and isotach (constant wind speed contour) plot during Hurricane Fabian on September 2$^{nd}$, 2003 (Fig. 2.10 and Fig. 2.11).

The "wind barbs" plot in Fig. 2.11 is the corresponding composite wind measurements from various airborne and surface wind sensors, which were input to generate the analysis output wind isotach plot in Fig. 2.12. The orientation of the wind barbs shows the direction of the wind that blows toward the "dot". Short and long barb lines represent 5 and 10 knot (~2.5 and 5 m/s) wind speed increments respectively, and a solid triangular-shaped barb represents a 50 knot (~25 m/s) wind speed increment. The color of the plot denotes the source of the wind measurement. The "green square" and "red square" represent the start and end storm center locations (TC eye) during the period of the analysis.

A wind isotach plot in Fig. 2.12 shows a constant-wind-speed-contour with 5 knot increment. The isotach plot is equally divided into four quadrants: northeast (NE), northwest (NW),

southeast (SE), and southwest (SW). The numbers displays at the upper left corner of the figure are the radii distance of storm class (based on the SSHS). Wind speed (numbers in the second row at the upper left corner) of 34 knots is gale, 50 knots is storm, and 64 knots is hurricane; and the numbers below are the corresponding radii distance in nautical mile. The white arrows are the direction of the wind flow.

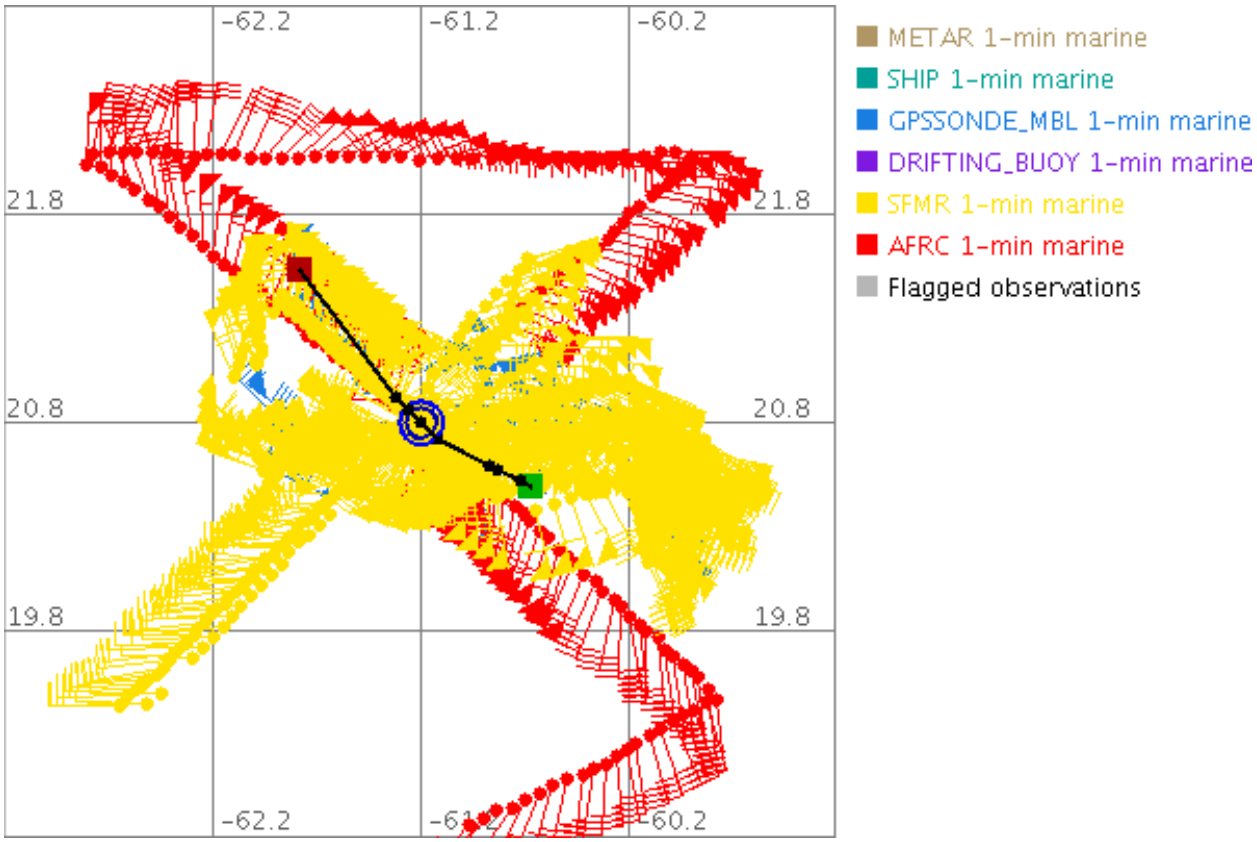


Fig. 2.10: H*Wind input wind vector observations for Hurricane Fabian on September 2nd, 2003.

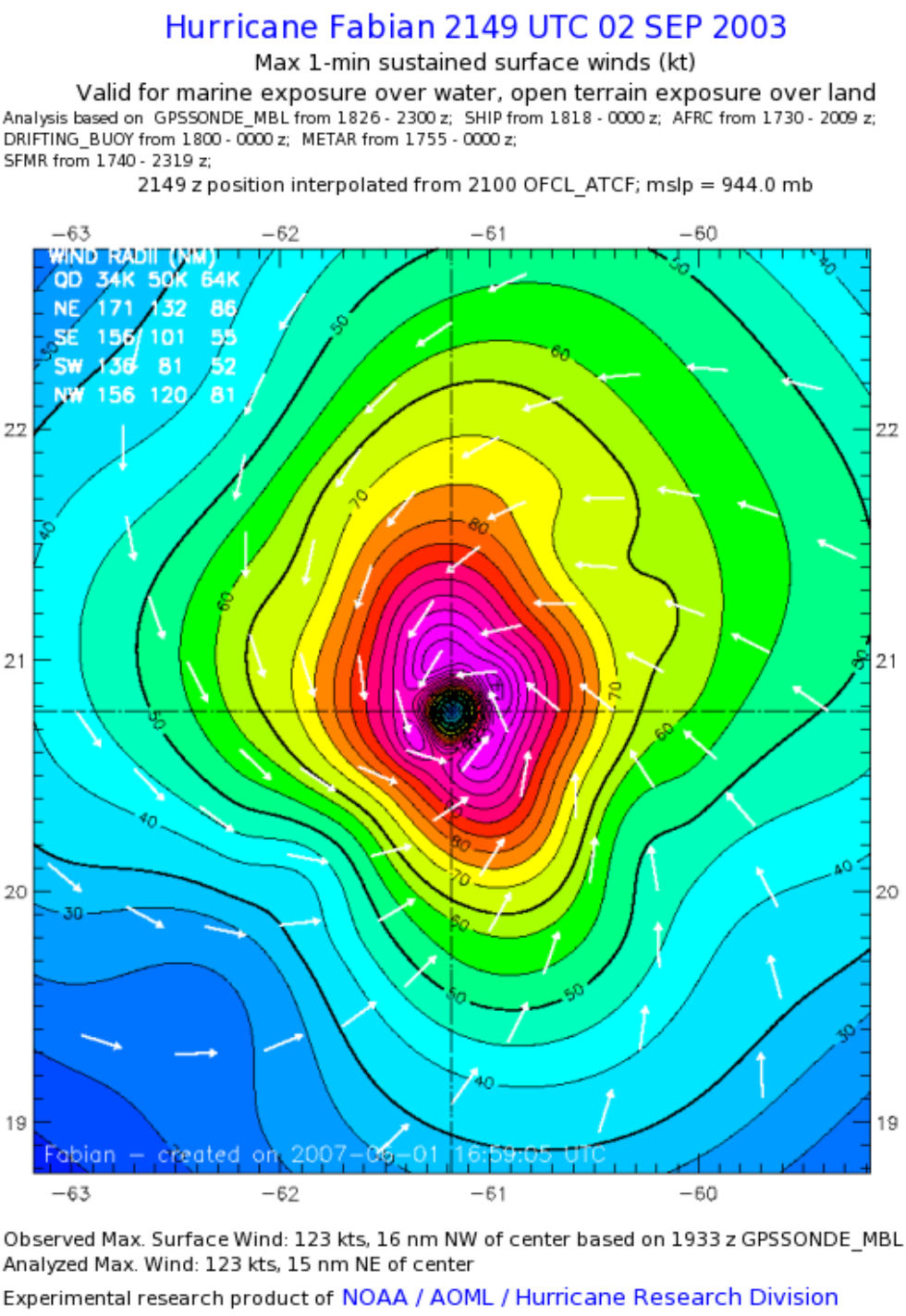


Fig. 2.11: H*Wind analysis output isotach wind field of Hurricane Fabian on September 2nd, 2003.

## 2.5 SeaWinds OVW Measurements for Hurricane

SeaWinds on QuikSCAT provides global ocean near-surface wind speed and direction measurement, which is vital for NASA in oceanographic, meteorological and climate studies for and NOAA's numerical weather forecasting.

Although, QuikSCAT OVW measurements are not optimal for extreme wind events (see Chapter-I), they are routinely used in TC analyses [1, 2]. These QuikSCAT science data products are processed and distributed by the NASA/ JPL Physical Oceanography Distributed Active Archive Center (PO.DAAC). All QuikSCAT standard products are in the Hierarchical Data Format (HDF) and referenced by WVC row and column indices. A data archive of QuikSCAT product can be obtained from the Physical Oceanography Distributed Active Archive Center (PODAAC) at http://podaac.jpl.nasa.gov/DATA_CATALOG/quikscatinfo.html.

### *2.5.1 QuikSCAT Level 2A Data Product*

The QuikSCAT Level 2A (L2A) data product contains ocean brightness temperature measurements, and radar $\sigma^0$ acquired during a full orbital revolution (rev) by location. Each L2A data element represents a 25 x 25 km resolution box, called a wind vector cell (WVC). Each WVC row of the L2A contains entire cross-track cut of the SeaWinds measurement swath. Because SeaWinds' conical scan configuration, the number of measurements may vary depend

on cross-track location in the swath and most WVC's in the swath contain approximately 12 to 30 measurements [35]. The $\sigma^0$ for each WVC is computed from the total echo energy of the ten high resolution $\sigma^0$ slices.

SeaWinds software allocates 810 measurement pulses per each WVC row to insure that all $\sigma^0$ are captured at the nominal rate. For each orbital rev, L2A data product contains 1624 rows and 810 columns in the HDF and each cell is referred by row and column indices. To avoid abrupt truncation of data, 39 additional WVC rows from the previous and after revs are included at the beginning and the end of each rev. Thus, the nominal L2A file contains a total of 1702 WVC rows and 810 columns.

### *2.5.2 QuikSCAT Level 2B Data Product*

The QuikSCAT Level 2B (L2B) Processor data processes QuikSCAT L2A normalized radar cross section measurements and produces wind vector data for each WVC in alignment with the spacecraft grid of along-track and cross-track pixels of the measurements swath. One complete satellite orbital rev contains 1624 WVC rows in the along-track direction and 76 WVCs per row in the cross-track direction. The L2B wind vector ambiguities (possible solutions) are retrieved from an empirically based model function using MLE method. The ambiguity removal algorithm is then used to determine the "best solution" estimate of the "true" wind vector. The data in L2B data are contains various geophysical parameters, e.g., retrieved wind speeds and wind directions

(aliases), numerical weather model wind speeds and wind directions, QRad retrieved rain rate. Every L2B data element can be referenced by the WVC's cross-track and along-track indices.

Since July 2006, L2A and L2B data were reprocessed to improve the measurement spatial resolutions. The improved spatial resolution Level 2 products (L2A-12.5km and L2B-12.5km) are available on a 4x WVC grid at a resolution of 12.5 km (from 25 km). Both L2A's and L2B's data products are provided from NASA PODAAC, JPL; and further information can be found at ftp://podaac.jpl.nasa.gov/ocean_wind/quikscat/L2B/doc/QSUG_v3.pdf.

# CHAPTER-III: Q-WINDS HURRICANE RETRIEVAL ALGORITHM

## 3.1 Introduction

This chapter describes a unique technique to infer hurricane oceanic surface wind vector, known as the "Q-Winds" algorithm, developed at the Central Florida Remote Sensing Laboratory (CFRSL) using solely the SeaWinds scatterometer on QuikSCAT, which is the topic of this dissertation. This algorithm is based on the conventional scatterometer wind vector retrieval with the following notable unique aspects. First, Q-Winds uses combined active/passive measurements to estimate the rain-corrected ocean surface $\sigma^0$ from the scatterometer measured radar backscatter at the "top of the atmosphere". This is a significant advancement because there is no rain correction in the conventional scatterometer wind vector retrievals. Second, unlike the traditional scatterometer algorithms that retrieve the **synoptic-scale spatial average wind speeds** over the WVC, this algorithm is designed to infer the **one-minute sustained wind speed** in hurricanes. Moreover, this algorithm is highly specialized in purpose to be used for extreme wind events; and as such it augments the conventional QuikSCAT project OVW products. Also for the final quality assurance (QC) process, rain flags are provided to identify low confidence (suspect) retrieved elements.

## 3.2 Satellite Microwave Wind Scatterometry

Satellite microwave scatterometers are well-suited for the task of global measurements of ocean surface winds. First, microwaves easily penetrate clouds to "see" the ocean surface and are capable of making measurements during day/night under nearly all weather conditions. Second, their wide swath coverage provides global measurements with frequent revisit time from polar orbiting satellites. Third, the scatterometer GMF has been proven to be robust, i.e., the ocean normalized radar cross section responds only to the speed and direction of the surface wind and is independent of other ocean surface parameters, such as sea surface temperature (SST), wave height, fetch, salinity, etc.

The fundamental concept of using microwave scatterometry to infer ocean wind vector relies on the interpretation of the ocean surface small-scale roughness from the measured ocean normalized radar cross section or ocean radar backscatter, $\sigma^0$. The ocean $\sigma^0$ depends on the power spectrum of these small-scale waves (radar scatters) driven by ocean surface wind. For near-nadir (normal incidence angle) measurements, the ocean radar backscatter is primarily from specular reflections from the tilted surface that is roughened by ocean waves in the illuminated area. Here the ocean $\sigma^0$ depends on the root-mean-square (RMS) slope that is determined by ocean waves that are significantly greater than the electromagnetic wavelength. However, for off-nadir measurements (incidence angle greater than approximately 30°), the backscatter is primarily due to Bragg scattering that occurs when the ocean wavelengths are comparable to the radiation wavelength [36]. This phenomenon is caused by periodic ocean waves with

wavelengths on the order of a few centimeters, which are named capillary waves. The local wind drag force per unit area, known as wind stress, transfers momentum to ocean surface by forming and sustaining these small-scale capillary waves. Further, these capillary waves are also anisotropic with angular characteristics caused by azimuthal spreading of the wave spectrum about the average wind direction.

To illustrate the scatterometer measurement, consider an ocean surface with small-scale ocean waves generated by wind. The scatterometer transmits an EM pulse to the ocean surface at an off-nadir angle and measures the returned echo energy as illustrated in Fig. 3.1. The ocean radar cross section, $\sigma^0$, is determined using the radar equation,

$$\sigma^0 = \frac{(4\pi)^3 R^4}{P_t G^2 \lambda^2 IFOV} P_r \tag{3.1}$$

where $R$ = distance from antenna to the ocean surface (m)

$P_t$ = transmitted power (W)

$G$ = antenna gain

$\lambda$ = operating wavelength (m)

*IFOV* = antenna instantaneous field of view, i.e., the effective area of the illuminated ocean surface (antenna footprint), $m^2$

$P_r$ = received power (W)

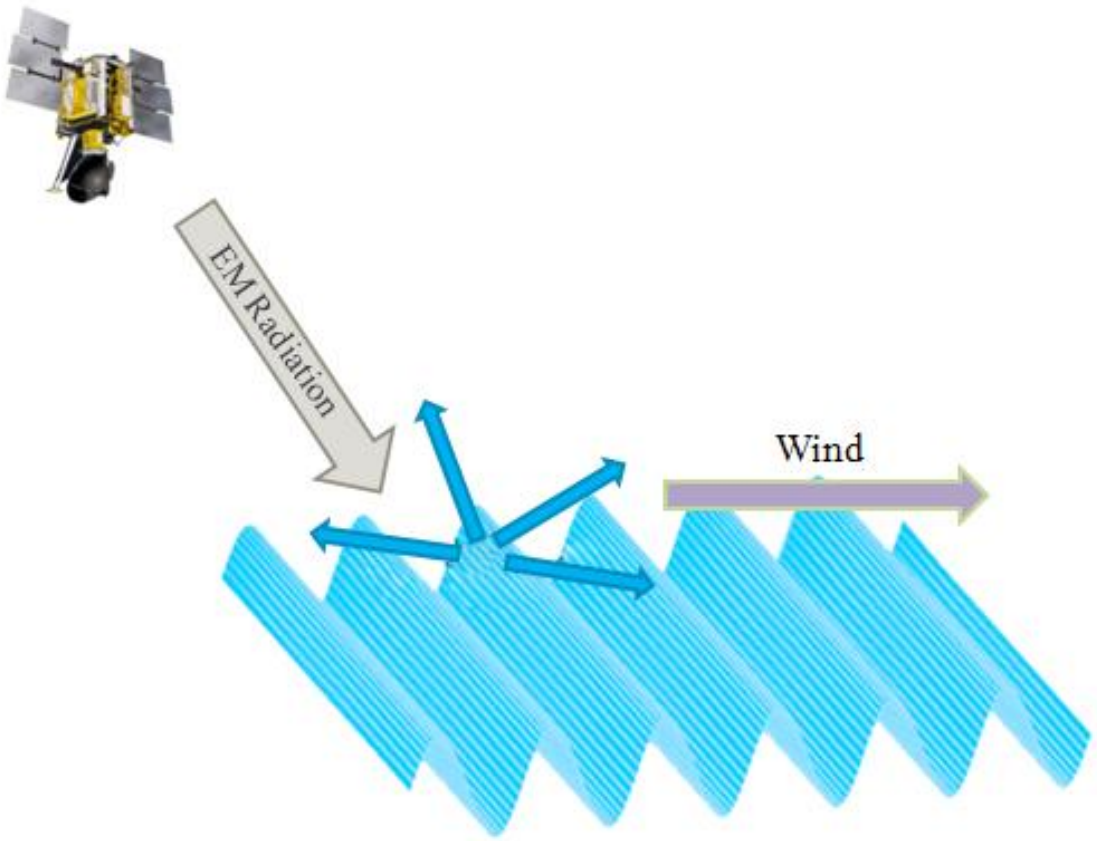


Fig. 3.1: Off-nadir scatterometer backscatter measurements from the ocean surface.

At the scatterometer off-nadir incidence angle, the Bragg resonance results in an augmented radar backscatter caused by the constructive combination of the coherent electromagnetic fields scattered from the crests of these Bragg waves. The measured radar echo amplitude is directly proportional to the amplitude of the Bragg capillary wave spectrum, which is in near-equilibrium with the local wind stress (friction velocity). By obtaining $\sigma^0$ measurements from multiple azimuth angles the near-ocean surface wind vector can be inferred using the relationship between radar "look" geometry (azimuth and incidence angles), wind vector (speed and direction) and ocean $\sigma^0$, known as the geophysical model function (GMF) [37, 38]. The ocean $\sigma^0$ also depends on many radar observation parameters, e.g., incidence angle, frequency, polarization, and azimuth angle relative to wind direction.

In radar scatterometry, the GMF is the empirical relationship that relates radar backscatter to the radar measurement geometry and the ocean surface wind vector. In practice, GMF is the ocean normalized radar cross section expressed as a power ratio that is tabulated in a look-up table as a function of the speed of the neutral stability wind at 10-m altitude and the observed relative azimuth look angle (relative to wind direction). GMF's are developed for specific radar operating frequencies, beam polarizations, and incidence angles.

The model functions for satellite scatterometers are usually empirically derived from large collection of scatterometer measurements (on-orbit) collocated with known 10-m wind speeds and relative wind directions. In the conventional GMF training process, millions of wind vectors from numerical weather models are used to provide an adequate database. Because ocean wind speeds have an approximately Rayleigh probability distribution with mean values of 6 – 7 m/s, the occurrences of high wind speeds are extremely rare. Experimentally, the GMF is well defined over all relative wind directions; but only for wind speed up to ~ 20 m/s; and beyond this point, the GMF is extrapolated to a maximum value of ~50 m/s. The general formula of GMF is defined as:

$$\sigma^0 = GMF(u, \chi, \theta, p, f) \tag{3.2}$$

where $u$ = neutral stability wind speed at a height of 10 m (m/s)

$\chi$ = the relative wind direction (deg)

$\theta$ = the incidence angle (deg)

$p$ = the EM polarization (vertical or horizontal)

$f$ = the operating frequency (Hz)

The GMF is an even function, which exhibits a strong bi-harmonic characteristic with the largest $\sigma^0$ response occurring at 0° (upwind) and a secondary maximum at $\chi$ = 180° (downwind). The minimum $\sigma^0$ responses occur when wind blows perpendicular to the scatterometer observation azimuth at 90° or 270° (crosswind). Because of the harmonic nature of the GMF, there are multiple combinations of wind speed and relative azimuth that can result in identical $\sigma^0$'s.

When expressed in dB, $\sigma^0$ may be approximated in a three-term Fourier series:

$$\sigma^0 = C_0 + C_1 cos\chi + C_2 cos2\chi \tag{3.3}$$

where $C_0$, $C_1$, and $C_2$ are coefficients expressed in dB that are functions of wind speed, incidence angle, polarization and frequency. It should be noted that this simple approximation is not used for conventional scatterometer GMF; rather the GMF is implemented as a table of "binned averages" from the experimental observations.

Figure 3.2 illustrates the QuikSCAT GMF (QS-GMF) for H-pol response (top panel) and V-pol response (bottom panel) at various wind speeds (from 10 to 50 m/s in 10 m/s increment) for all relative wind directions. Although both polarizations have similar azimuthal response patterns, i.e., upwind, downwind, and crosswinds, but the detailed values of the GMF's are different. For example, at the low wind speed region, the upwind to downwind response of the H-pol is greater than the V-pol. As wind speed strengthens, the GMF peak-to-peak response (upwind to crosswind) for the two polarizations decreases and becomes similar; but, the isotropic responses (average value over all directions) are different e.g., note that at high wind speeds, the V-pol saturates at a lower $\sigma^0$ value than does the H-pol. The magnitude of the three Fourier coefficients of the GMF *versus* the $\log_{10}$ of wind speed is shown in Fig. 3.3.

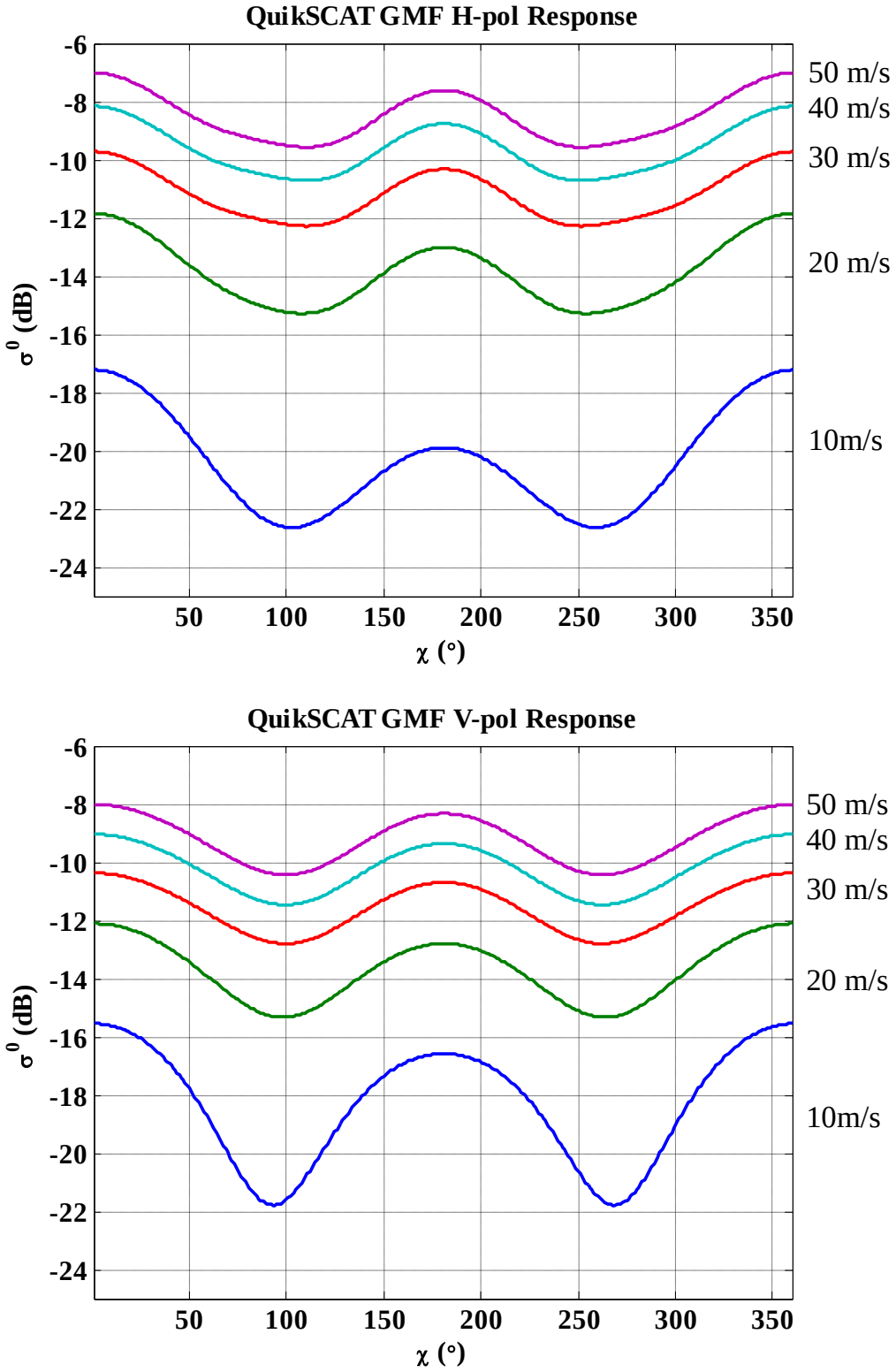


Fig. 3.2: QuikSCAT GMF response where the top panel is H-pol and bottom panel is V-pol.

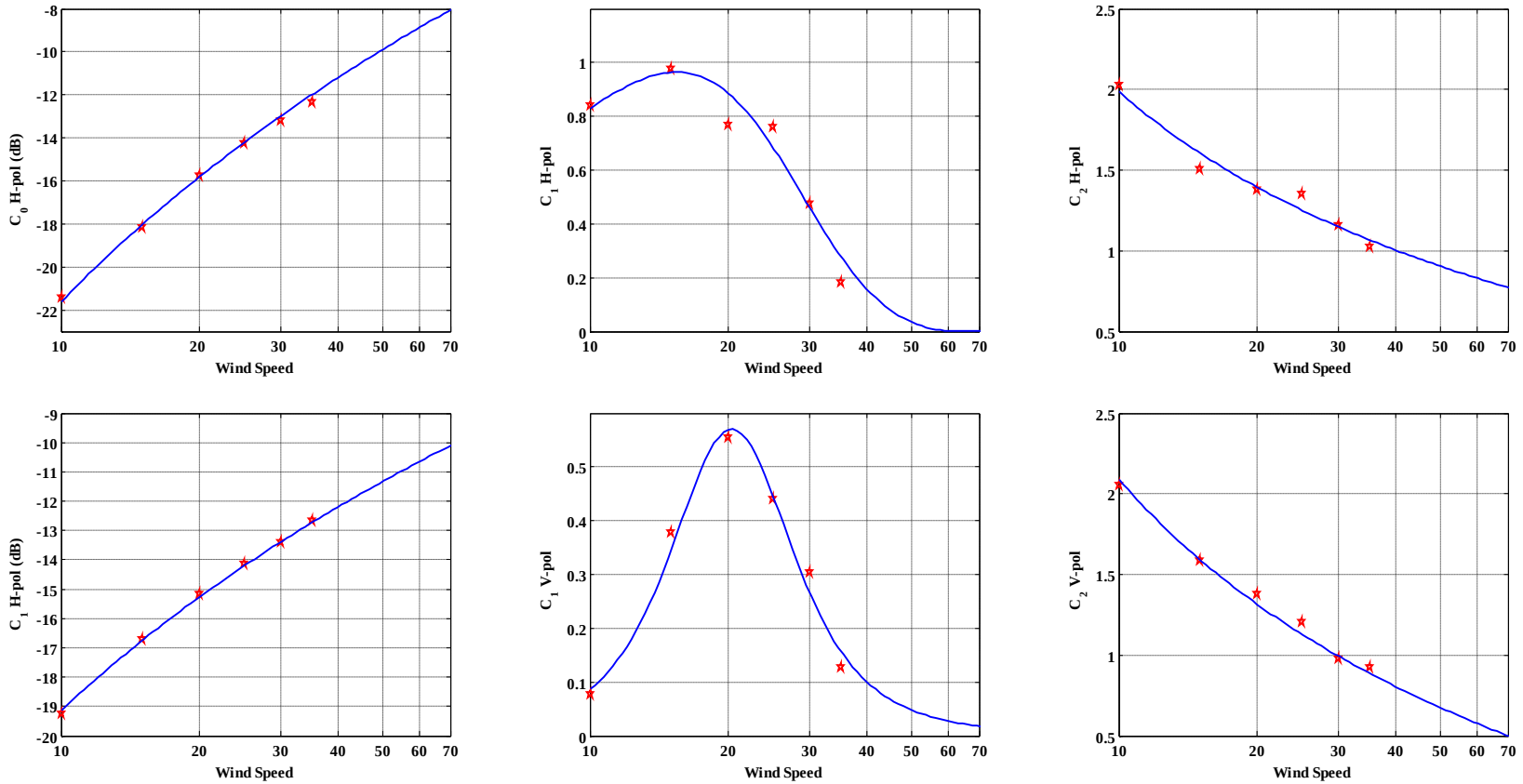


Fig. 3.3: GMF coefficients for H-pol (top panels) and V-pol (bottom panels). Symbols are derived Fourier coefficients from empirical regression analyses using binned H*Wind speed averages.

For a given wind vector cell (WVC) to solve for the wind vector, the scatterometer must make multiple $\sigma^0$ observations of the ocean surface from different azimuth angles; and an algorithm called wind vector retrieval is performed. Traditionally, scatterometers use a maximum likelihood estimation (MLE) algorithm to determine all possible wind speed and direction pairs for each WVC that best matches the $\sigma^0$ measurements and maximizes the likelihood probability of a cost function or an objective function (see Appendix-A & -B).

The wind vector solutions are obtained through an iterative search routine to optimize the objective function, i.e., to minimize the mean-square error between the "true wind vector" and estimated "wind vectors". Because of two unknowns (speed and direction), at least two $\sigma^0$ measurements from two different azimuthal looks are required to determine a wind vector solution [18]. Because of the harmonic nature of the GMF and the $\sigma^0$ variability due to instrument noise, the objective function generally produces two to four principal minima and results in non-unique solutions. These wind vector solution sets are known as wind vector ambiguities or aliases. These aliases are then ranked according to the magnitude of the accumulative residue from the MLE where the 1$^{st}$ rank alias has the minimum residue value, the 2$^{nd}$ rank as the next lowest residue, and so on. In the absence of measurement error and for an idealized GMF, the 1$^{st}$ ranked alias is always the correct wind vector; however in practice, this is not always the case. Nevertheless, there is skill in the 1$^{st}$ ranking, and on average the 1$^{st}$ ranked is the correct wind direction solution. Further, in practical situations, either the 1$^{st}$ or 2$^{nd}$ ranked alias is most likely the correct solution. Therefore, in order to select a single unambiguous wind direction (i.e., "**correct solution vector**"), an ambiguity removal algorithm is must be used.

Ambiguity removal routines are typically *ad hoc* and mainly rely on the spatial filtering (median filtering) concept. This procedure involves iterative median filtering processes begins with using 1st rank solutions only and for each iteration the next ranked alias is added to determine new direction. After the MLE retrieval is performed, median filtering with a fixed window size (7 × 7 (175 km × 175 km) for SeaWinds processing) is used to select a unique wind vector from a wind vector solutions set. Because the 1st rank solutions are correct > 50% of the times, therefore, median filter of the 1st rank can provide a "good guess" of the wind direction. Next, new wind direction is selected from the closest direction from the 1st and 2nd rank aliases. This process (median filtering and alias selection) is repeated with next ranked alias included until all aliases are considered.

## 3.3 Q-Winds Hurricane Retrieval

The functional block diagram of the Q-Winds wind vector retrieval algorithm is illustrated in Figs. 3.4a and 3.4b. This algorithm comprises four major steps: rain effects correction, wind vector retrieval, alias removal, and QC rain flagging. First, the measured $\sigma^0$ collocated in WVC's (from L2A-12.5km data product) is adjusted for rain attenuation and rain volume backscatter using the simultaneous QuikSCAT Radiometer (QRad) brightness temperatures (Tb) to estimate the wind-driven ocean surface $\sigma^0$. Second, the MLE wind vector retrieval is performed using a special empirical GMF tuned for hurricanes. Third, we use *a priori* knowledge of the TC wind direction (counter-clockwise (CCW) in the northern hemisphere) for improved wind direction

ambiguity selection. Finally, the QRad Tb is used to provide an improved excessive-rain quality flag.

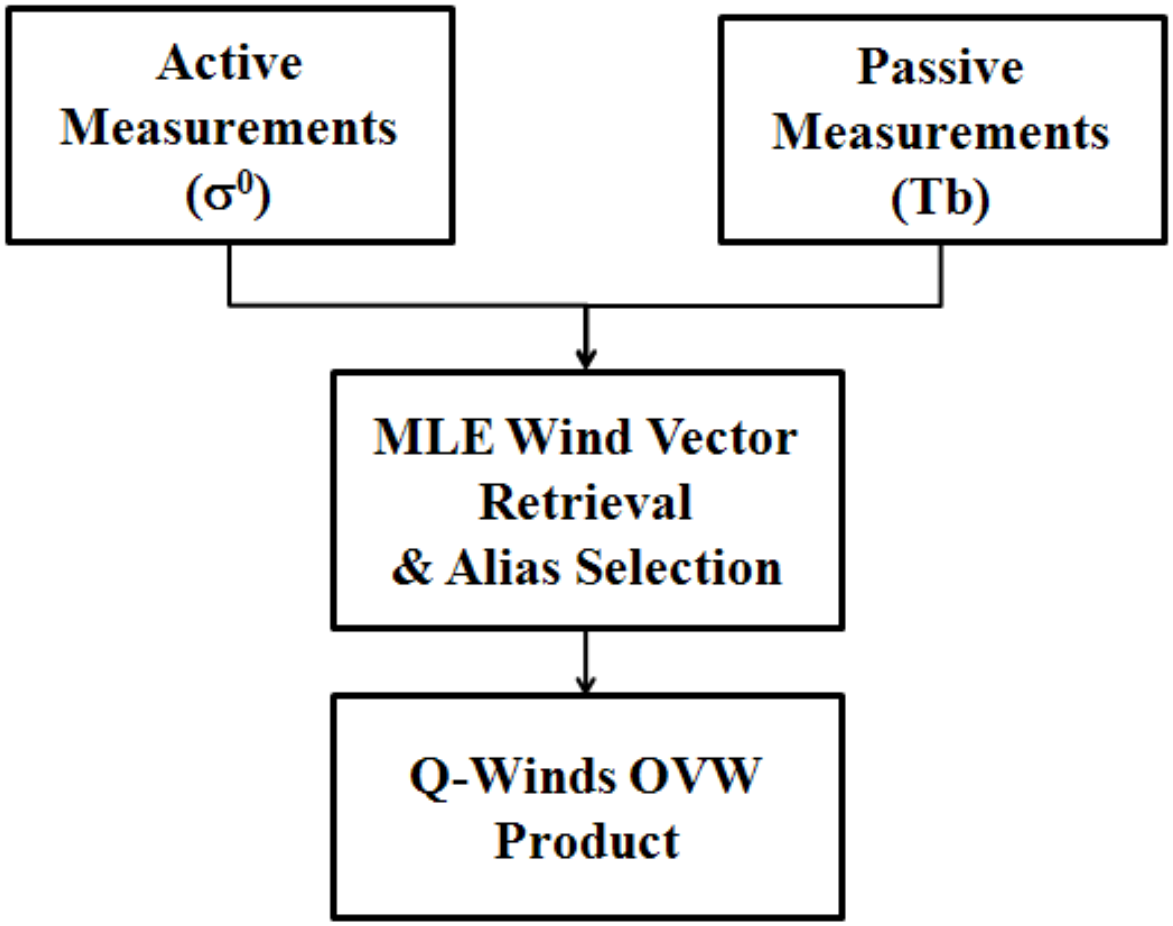


Fig. 3.4a: Simplified functional block diagram of the Q-Winds algorithm.

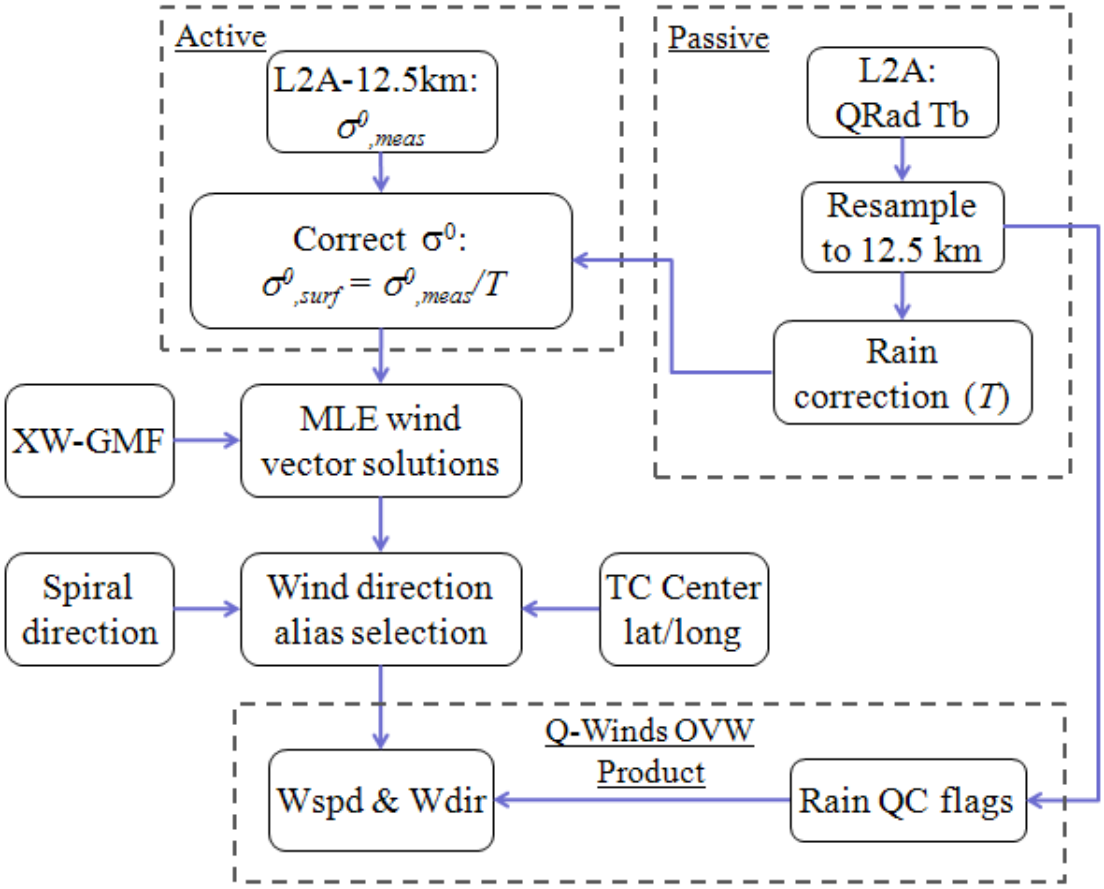


Fig. 3.4b: Detailed functional block diagram of the Q-Winds algorithm.

### *3.3.1 QRad Brightness Temperature*

Previously CFRSL developed an algorithm to infer passive ocean Tb that was derived from the SeaWinds antenna noise measurements [39-41]. This technique known as the QuikSCAT Radiometer (QRad) produces Tb's, which are included in the L2A and L2A-12.5km products. The QRad Tb's from the L2A have been validated by direct comparisons with Tropical Rainfall Measuring Mission (TRMM) Microwave Imager (TMI) [39]; however, a similar product in L2A-12.5km has not. Further, it has been observed that the additional Tb variance associated with this higher spatial resolution product causes poorer performance in the Q-Winds OVW retrieval; therefore, the QRad Tb used in this dissertation is extracted from L2A at 25 km resolution. The procedure involves resampling (smoothing) the 25 km Tb to 12.5 km, and then using this to compute two-way rain transmissivity correction for the measured $\sigma^0$'s, which is described in the following subsection. Also, the passive QRad Tb's are used to provide a quality control excess-rain flag as described in subsection 3.3.5.

### *3.3.2 Rain Effects Correction*

The SeaWinds scatterometer has remarkable accuracy for inferring ocean winds, over the range of 2 - 20 m/s, in rain-free conditions. Unfortunately, radar backscatter at 13.4 GHz is sensitive to rain and the resulting OVW retrieval performance can be adversely degraded; therefore, a rain correction is crucial in order to retrieve wind vectors accurately in the TC environment.

Rain interferes with ocean surface $\sigma^0$ measurements in three ways [42, 43]. First, atmospheric propagation through rain attenuates radar energy and reduces the apparent surface echo. Rain attenuation is an integrated two-way effect of both forward and return directions and is the dominant factor in atmospheric degradation. Second, rain volume backscatter increases the observed $\sigma^0$; and this effect is significant at low wind speed where rain volume backscatter becomes dominate even for light rain. Fortunately, in hurricane applications where wind speeds are relatively strong; the rain volume backscatter is insignificant compared to rain attenuation except, where ice (grauple) scattering becomes an issue. This occurs in the convective rain cells with high rain rates in the hurricane eye-wall region. Finally, rain splash alters the ocean surface $\sigma^0$ by rain drops striking the ocean surface and thereby modifying the reflection characteristics [16, 44, 45]. However, this splash effect is implicit in the hurricane GMF, because at high wind speeds the ocean surface characteristics are altered by flying spray generated from strong wind shearing of the ocean wave crest; therefore the additional effect of rain drops splash are not significant.

Thus, rain corrections in this dissertation are made explicitly for the first two phenomena only. The corrected surface sigma-0, $\sigma^0_{surf}$, for a wind vector cell with rain is described as:

$$\sigma^0_{surf} = \frac{\sigma^0_{meas} - \sigma^0_{rain}}{\alpha} \tag{3.4}$$

where $\sigma^0_{surf}$ = the corrected surface $\sigma^0$

$\sigma^0_{meas}$ = the measured top-of-atmosphere $\sigma^0$

$\sigma^0_{rain}$ = equivalent rain volume backscatter

$\alpha$ = two-way atmospheric transmissivity

The QRad Tb is sensitive to both rain rate and high wind speeds associated with the TC; hence, it is not possible to reliably separate the wind and rain signals. In a similar manner, the influences of rain attenuation and rain volume backscatter cannot be differentiated; thus both phenomena are modeled as a single rain-effect correction. Consequently, for our algorithm Eq. (3.4) simplifies to:

$$\sigma^0_{surf} = \frac{\sigma^0_{meas}}{T} \tag{3.5}$$

where the effective atmospheric transmissivity, *T*, in the presence of rain, is empirically derived using the procedure described below.

We estimate the effective atmospheric transmissivity using the simultaneous QRad Tb's and measured $\sigma^0$'s collocated with the associated H*Wind surface truth. From above, the transmissivity is modeled as the ratio of the "estimated" surface sigma-0, $\sigma^0_{est}$ (determined from

H*Wind surface wind vectors and the XW-GMF) and the measured sigma-0 (at the top of the atmosphere) as a function of the measured QRad Tb for each polarization as follows:

$$T = \sigma^0_{meas} / \sigma^0_{est} \tag{3.6}$$

The derivation of the transmissivity ratio model was difficult to obtain because of the relatively small number of observations and high variability in the dataset that comprised: L2A-12.5km measured $\sigma^0$, QRad V- and H-pol Tb's and the associated one-minute sustained surface wind vectors. These data were extracted from rain contaminated WVC's in the eighteen TC revs of QuikSCAT and collocated H*Winds surface truth. Because of the noisy data, we derived the mean transmissivity ratio model using least square regressions between the binned-average transmissivity (black "x" in Fig. 3.5) and the QRad Tb for each polarization. At low Tb values (clear sky), the transmissivity is approximately 0.96 (-0.18 dB); and in the presence of strong rain, it monotonically decreases to 0.66 (-1.8 dB) as Tb approaches ~ 285 K. The sigmoid function is selected because of its "S" shape curve provides appropriate fit for transmissivity as a function of Tb; and the coefficients of the total atmospheric transmissivity model are tabulated in Table 3.1.

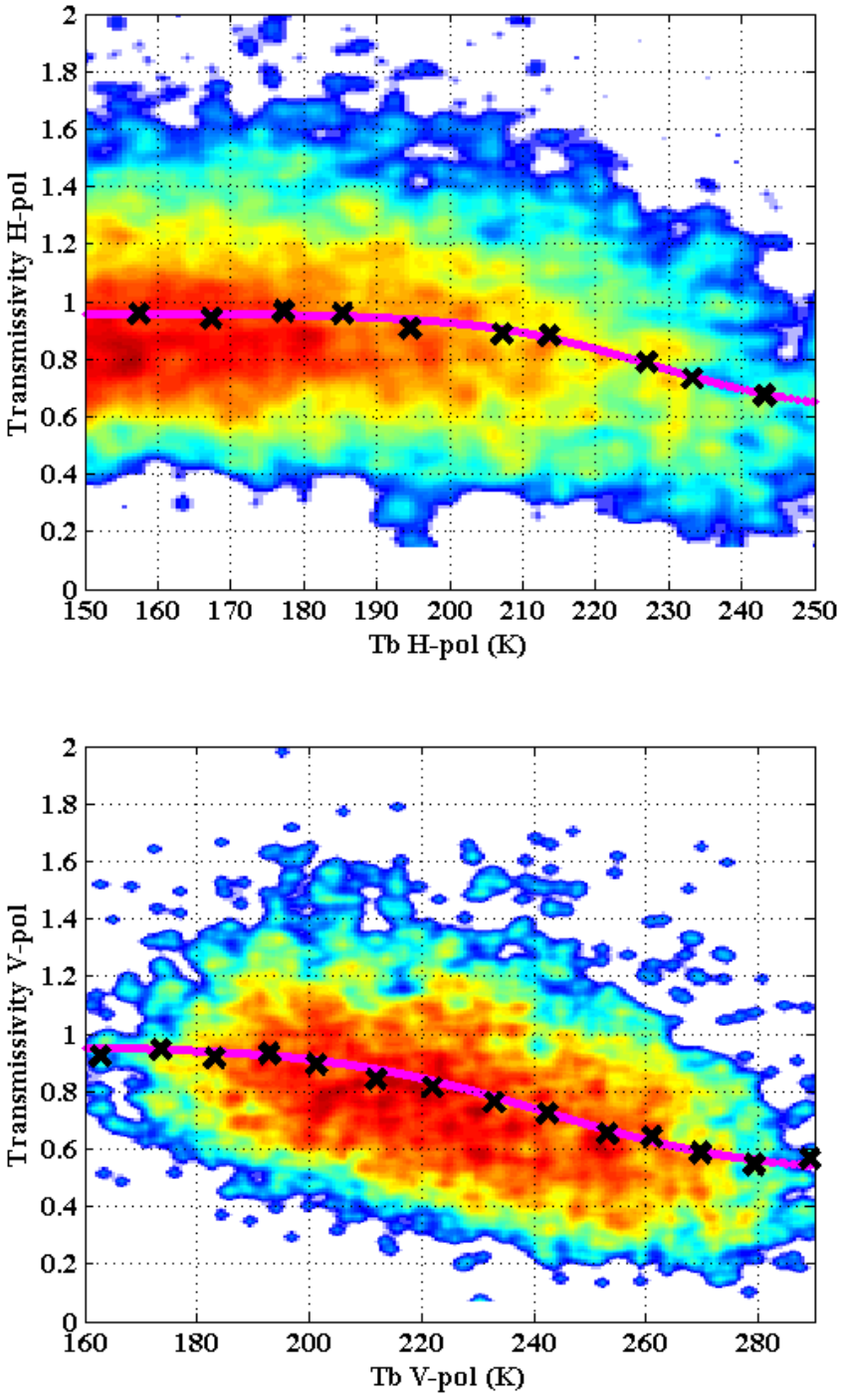


Fig. 3.5: Effective atmospheric transmissivity modeling for H-pol (upper) and V-pol (lower), where black "x" are the binned-averages on QRad Tb.

Table 3.1: Total two-way atmospheric transmissivity (*T*)

| | | |
|---|---|---|
| $T_H$ | a = 0.59<br>b = 12<br>c = 233 | $\frac{0.9594}{1+a} \times \frac{1}{1+\exp\left(-\frac{1}{b}(Tb-c)\right)}$ |
| $T_V$ | a = 0.9<br>b = 19.5<br>c = 254 | |

Unfortunately, the radar signal in the TC rain bands will be frequently highly attenuated whereby the surface echo cannot be accurately estimated. In such situations, reasonable rain correction and accurate wind vector retrieval cannot be achieved. Therefore, in practice, the transmissivity correction is limited to H-pol Tb's < ~250 K because of the excess-rain QC flags (described in subsection 3.3.5). From the user point of view, it is important to identify such low confidence data as unreliable surface wind retrievals.

### *3.3.3 Extreme Winds GMF (XW-GMF)*

As previously discussed in section 3.2, the QuikSCAT GMF was empirically defined for synoptic-scale winds up to 20 m/s, and beyond this point it was extrapolated to 50 m/s. As a result, Ku-band scatterometers are shown to be accurate for most ocean wind applications [46] but are not suitable for hurricanes. Previous studies by Carswell [46], Wentz [47], and Zec et al. [48] indicated the on-set of $\sigma^0$ saturation at surface wind speeds of approximately 30 m/s and

hard limits approaching 50 - 70 m/s. Furthermore, since conventional GMFs were trained using global synoptic scale winds, they are not applicable for measuring the transient peak "sustained gust" wind speed of the TC, which is desired in hurricane surveillance. Thus, a special GMF, known as the Extreme Winds GMF (XW-GMF), was developed using SeaWinds L2A-12.5km $\sigma^0$ and the collocated HRD H*Wind estimates of the one-minute sustained surface winds from eighteen hurricane events. In the training process, it is desirable to use all available data; but in TC conditions, high wind speeds are often associated with strong rain contamination, which is suspicious. Unfortunately, eliminating rainy pixels will also remove most high wind speed data; therefore, the data used in the GMF training procedure included both rain-free and light precipitation regions, where reasonable rain correction could be achieved. These data provided an adequate coefficient training set for wind speeds up to 35 m/s. For each wind speed bin, the $\sigma^0$ data (magenta points in Figs. 3.6 – 3.17) are collected from all relative wind directions. The wind speed bin sizes (used for averaging) were selected at ± 2 m/s for wind speed bins lower than 30 m/s, and bin size is increased to ± 3 m/s to collect an adequate number of points for regression analysis for wind speed above 30 m/s. Since the GMF is symmetrical about 180°, the data were mirrored about 180° to increase the number of points available for the regression analysis. Beyond 35 m/s, the GMF was extrapolated to approximately 70 m/s using the procedure described below.

As discussed previously, the ocean $\sigma^0$ response (in the dB domain) with wind speed and relative wind direction, $\chi$, is modeled as a three-term Fourier series (an isotropic mean plus 1$^{st}$ and 2$^{nd}$

harmonics of relative wind direction) for H- and V-polarizations, The XW-GMF is mathematically modeled as:

$$XW\text{–}GMF(u,\chi,p) = C_0(u,p) + C_1(u,p)\cos(\chi) + C_2(u,p)\cos(2\chi) \qquad (3.7)$$

The C coefficients are obtained by least square regressions of the binned-average data (red circles in Figs. 3.6 – 3.17) from all available wind speed bins for each polarization. The characteristics of the GMF are governed by these coefficients, which are: the isotropic mean $\sigma^0$ (averaged from all relative wind directions) is represented by $C_0$; the upwind-downwind characteristics are governed by $C_1$ and the upwind-crosswind characteristics are governed by $C_2$. Further, all of these coefficients exhibit a wind speed dependence as well an incidence angle and polarization dependence.

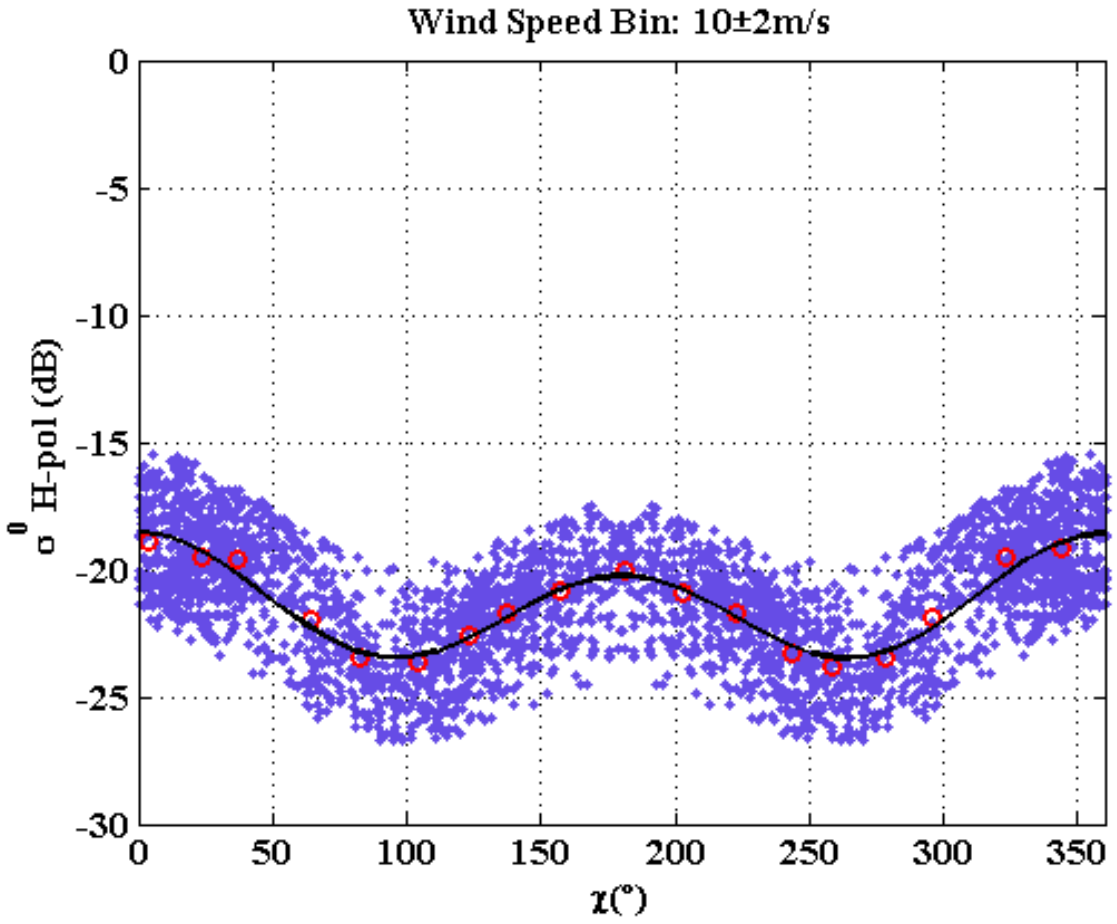


Fig. 3.6: H-pol ocean $\sigma^0$'s response to relative wind directions at wind speed bins of 10±2 m/s.

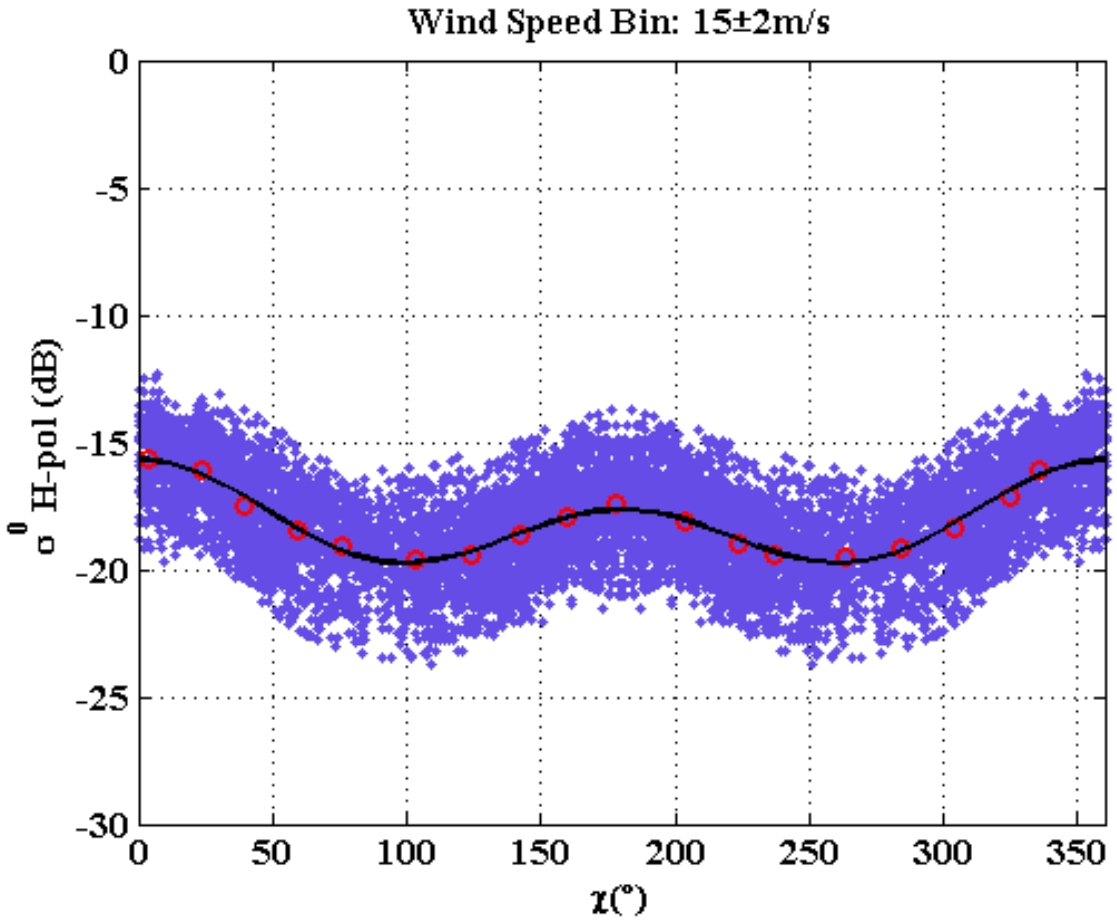


Fig. 3.7: H-pol ocean $\sigma^0$'s response to relative wind directions at wind speed bins of 15±2 m/s.

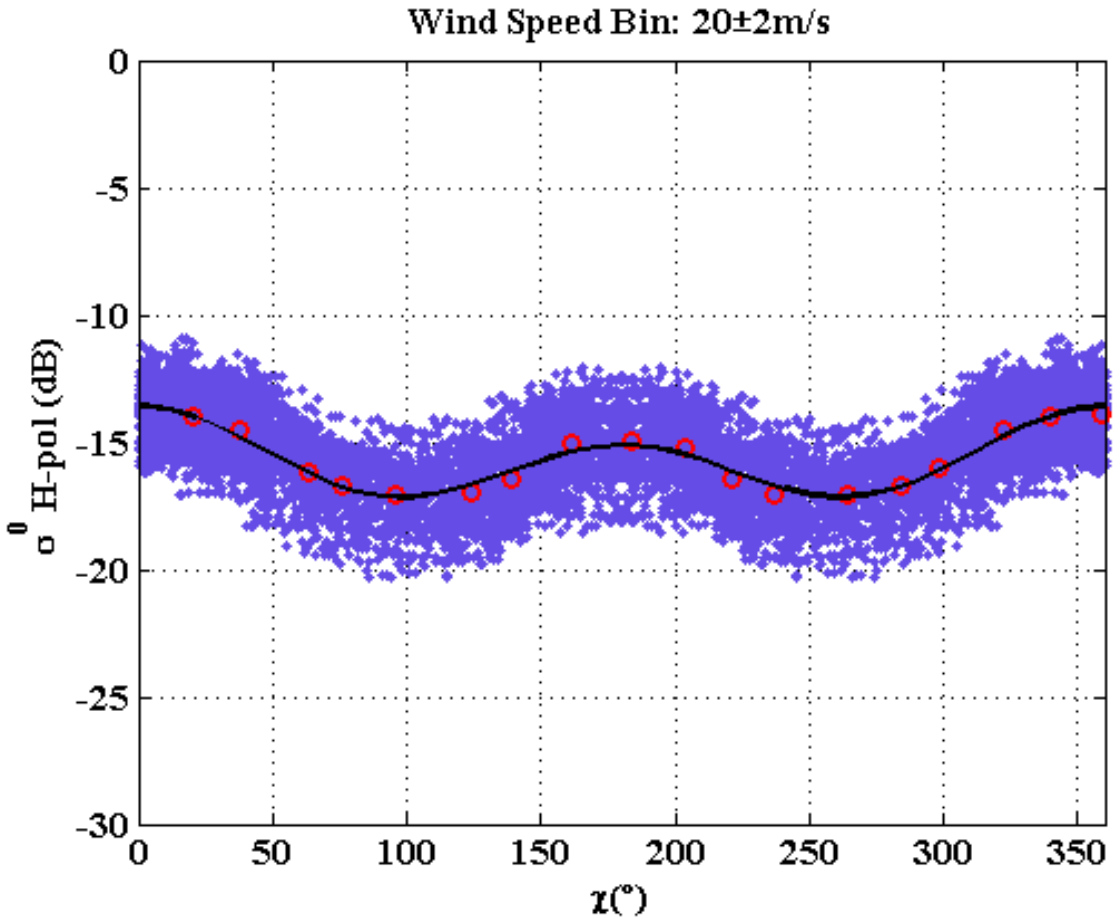


Fig. 3.8: H-pol ocean $\sigma^0$'s response to relative wind directions at wind speed bins of 20±2 m/s.

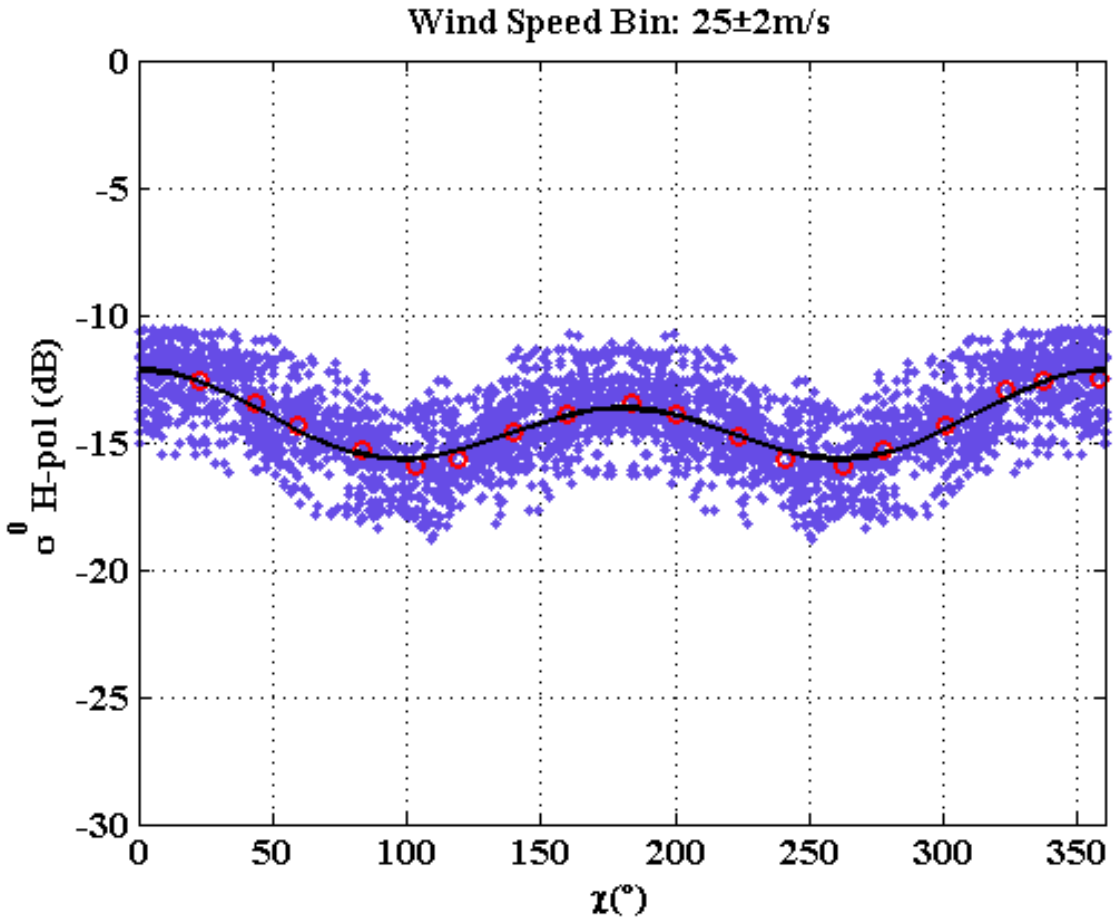


Fig. 3.9: H-pol ocean $\sigma^0$'s response to relative wind directions at wind speed bins of 25±2 m/s.

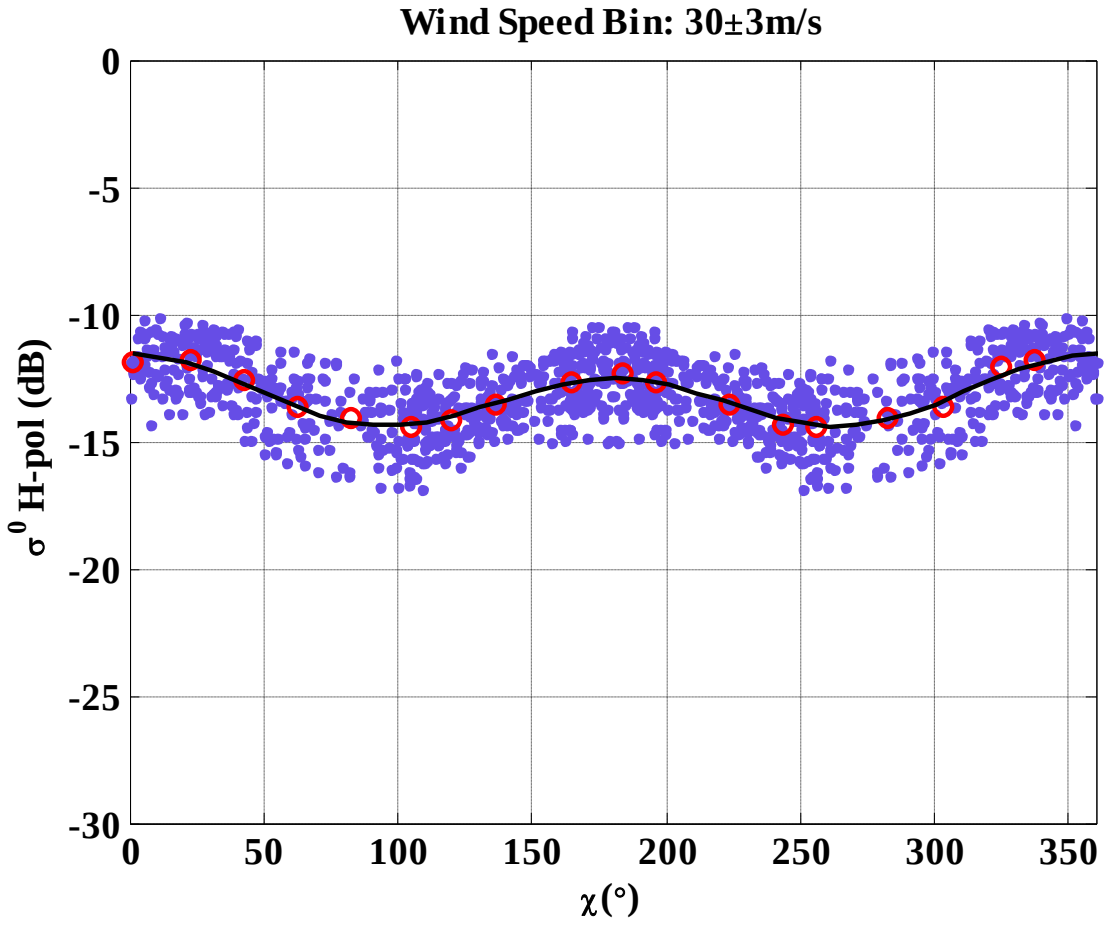


Fig. 3.10: H-pol ocean $\sigma^0$'s response to relative wind directions at wind speed bins of 30±3 m/s.

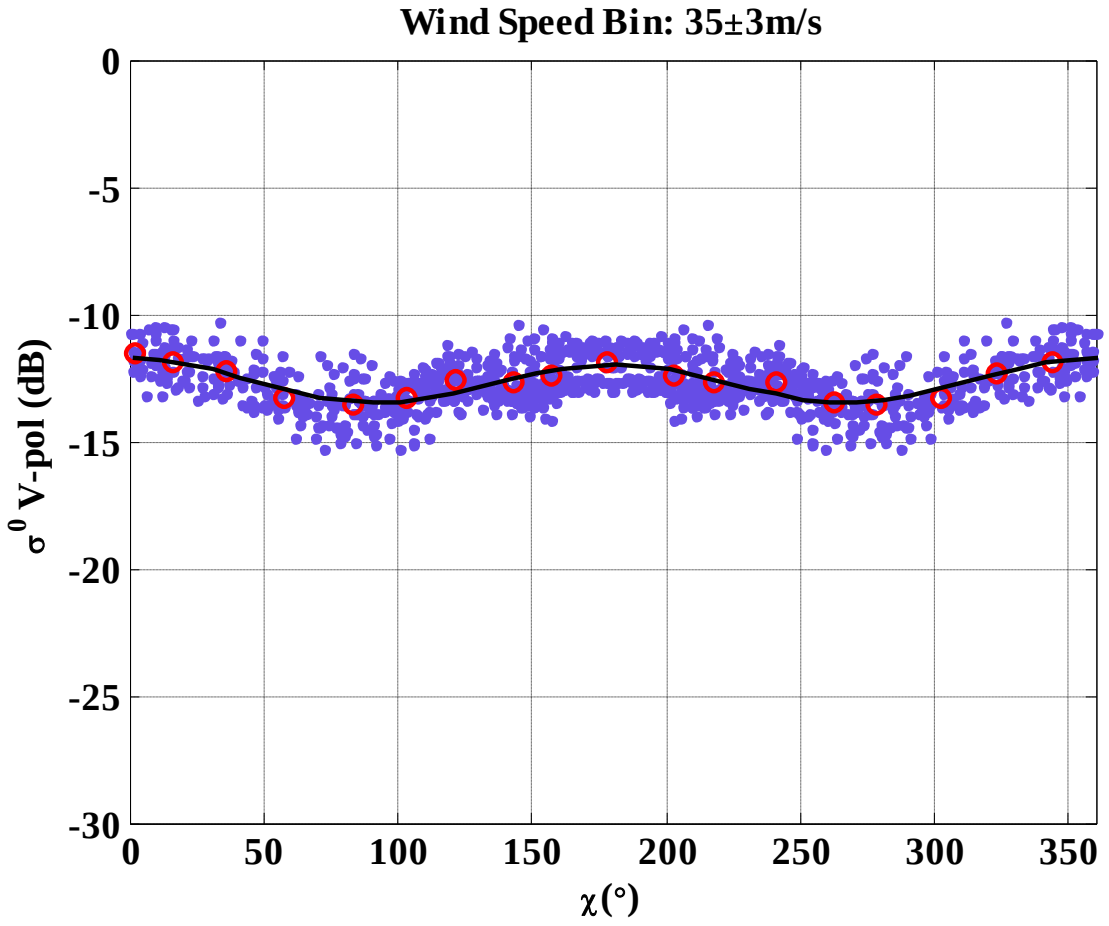


Fig. 3.11: H-pol ocean $\sigma^0$'s response to relative wind directions at wind speed bins of 35±3 m/s.

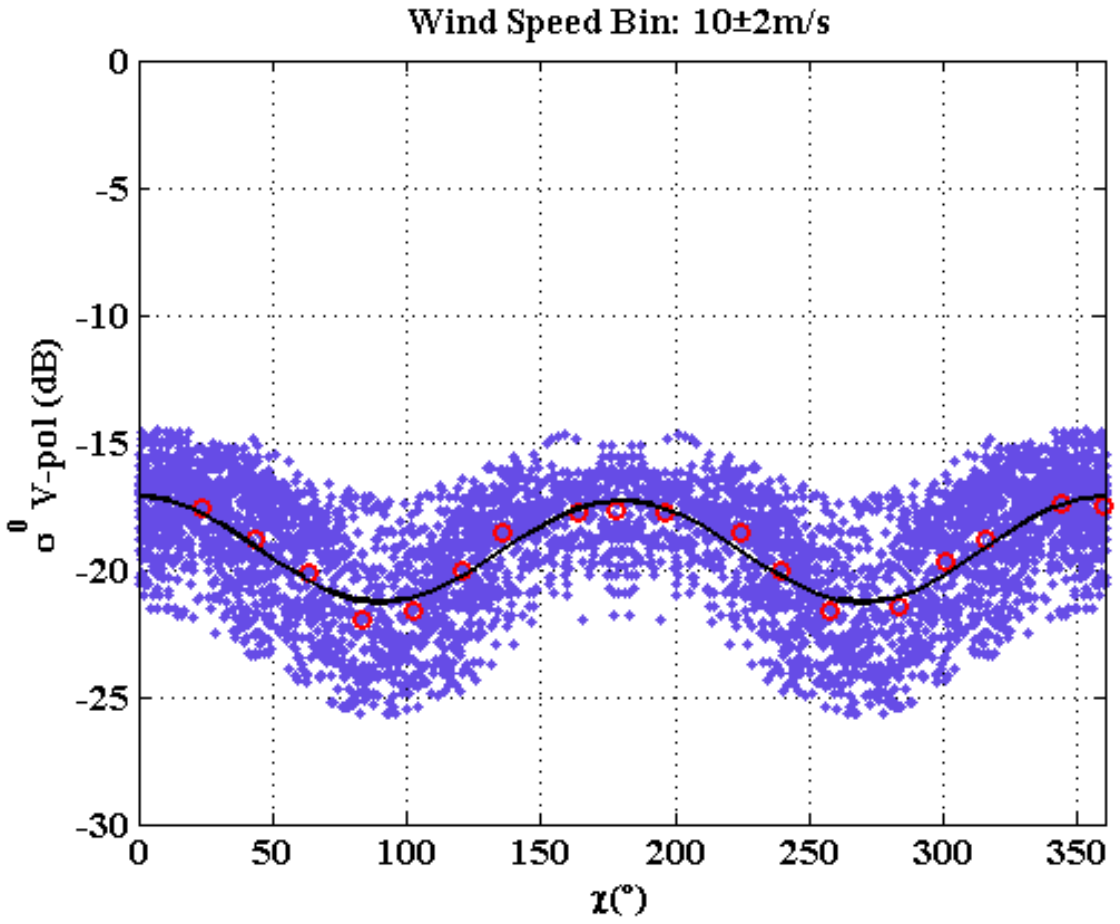


Fig. 3.12: V-pol ocean $\sigma^0$'s response to relative wind directions at wind speed bins of 10±2 m/s.

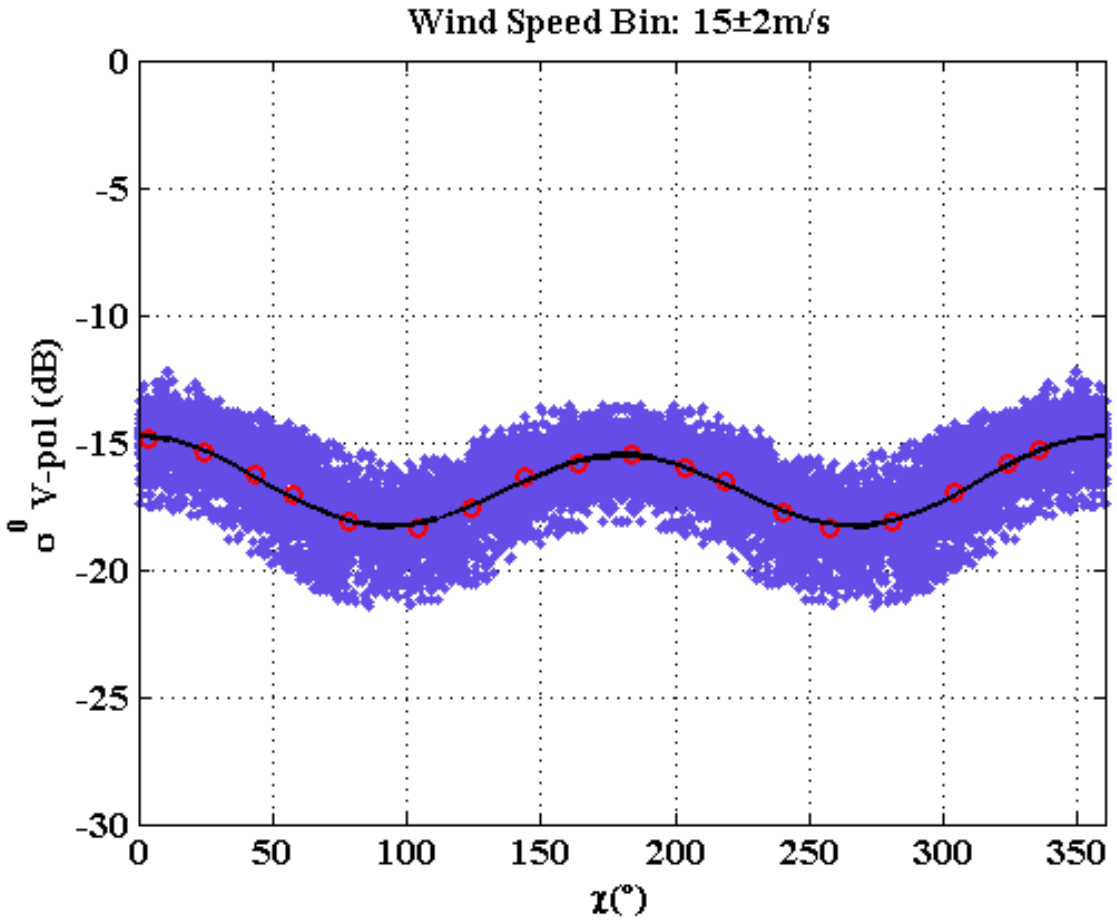


Fig. 3.13: V-pol ocean $\sigma^0$'s response to relative wind directions at wind speed bins of 15±2 m/s.

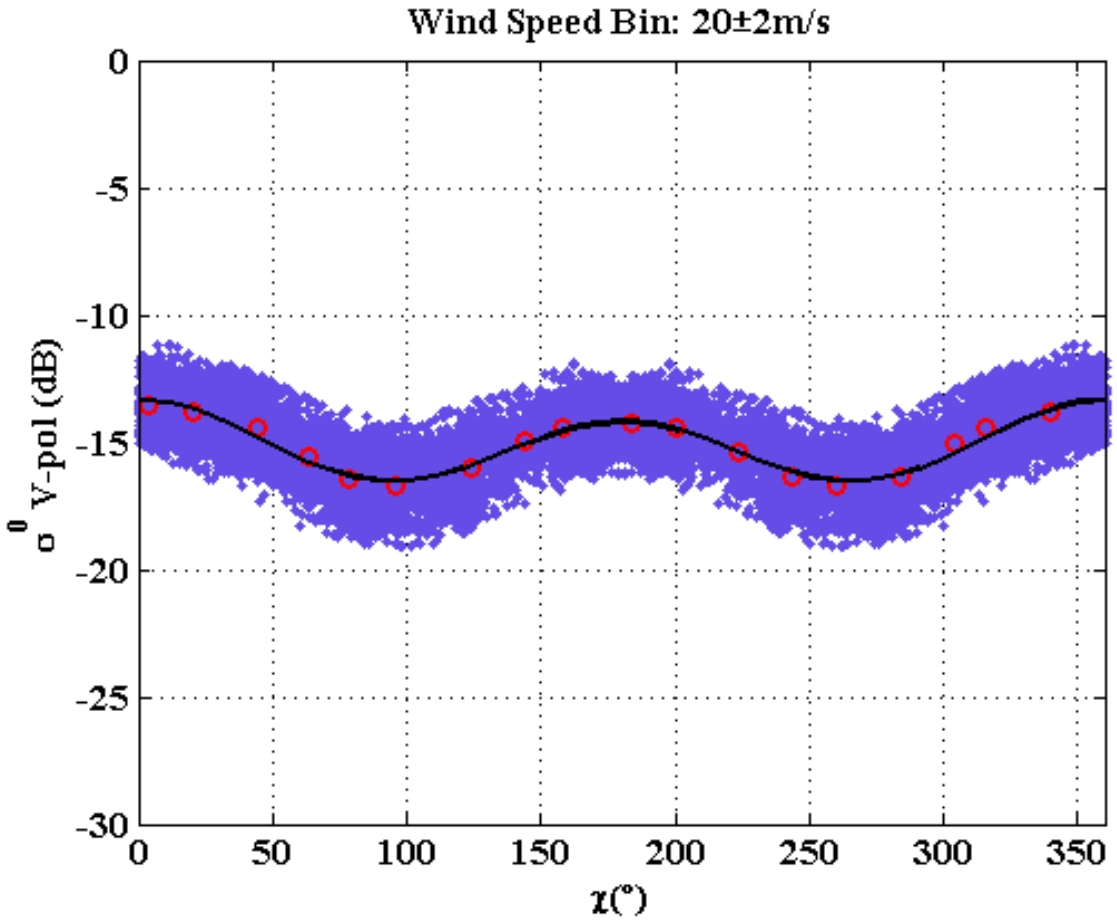


Fig. 3.14: V-pol ocean $\sigma^0$'s response to relative wind directions at wind speed bins of 20±2 m/s.

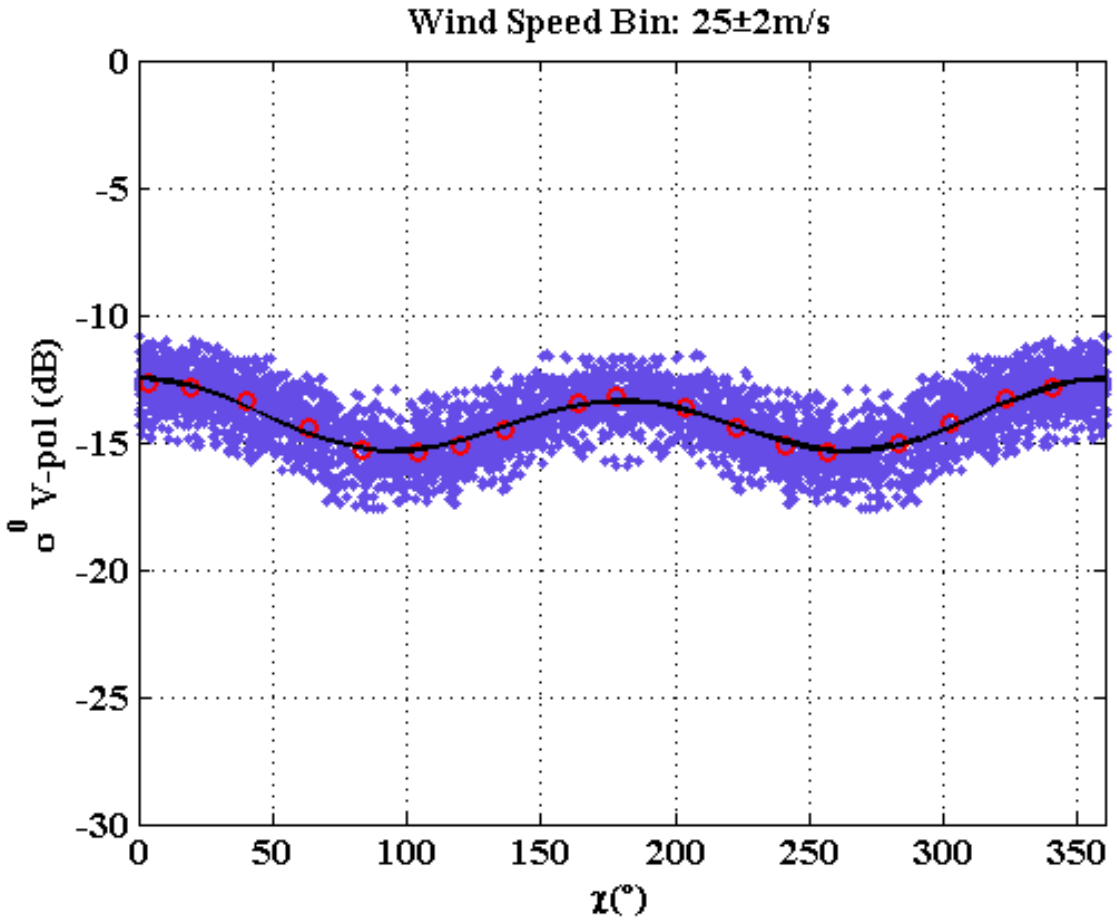


Fig. 3.15: V-pol ocean $\sigma^0$'s response to relative wind directions at wind speed bins of 25±2 m/s.

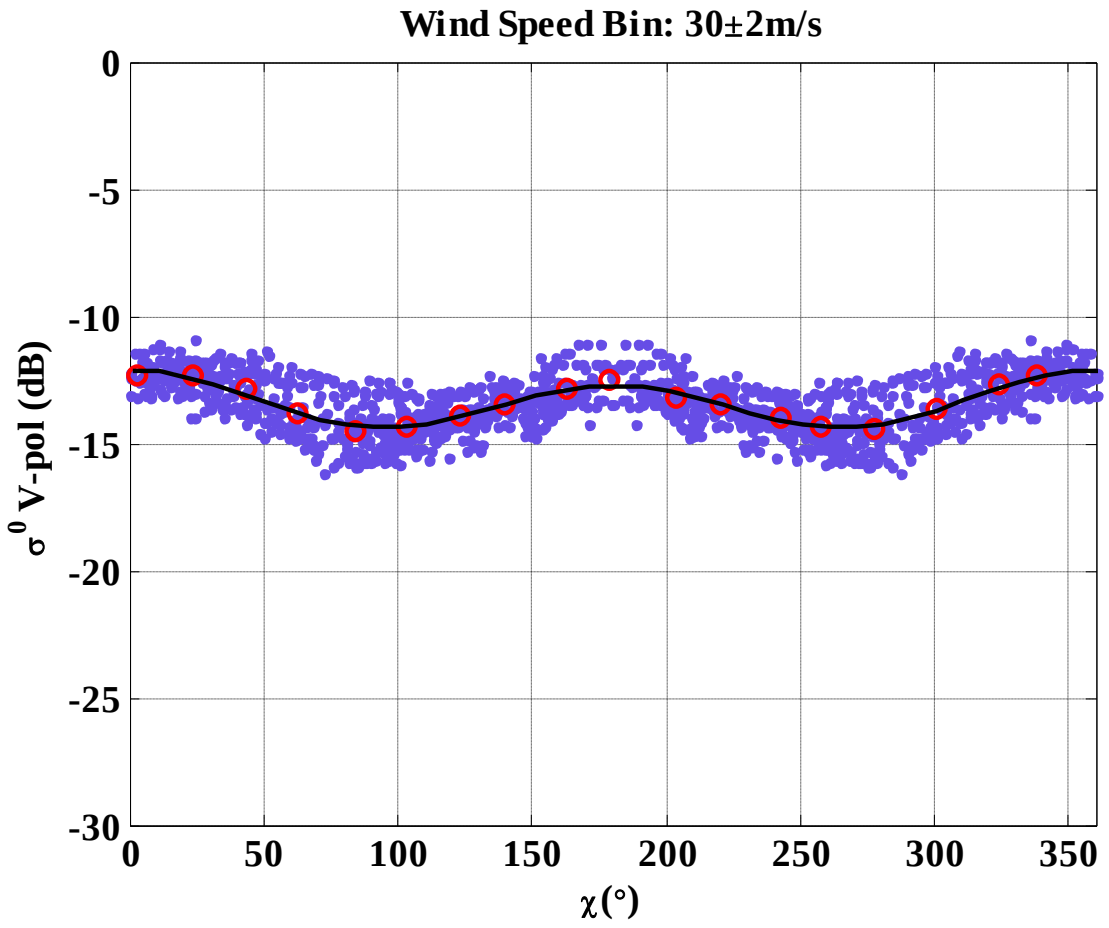


Fig. 3.16: V-pol ocean $\sigma^0$'s response to relative wind directions at wind speed bins of 30±3 m/s.

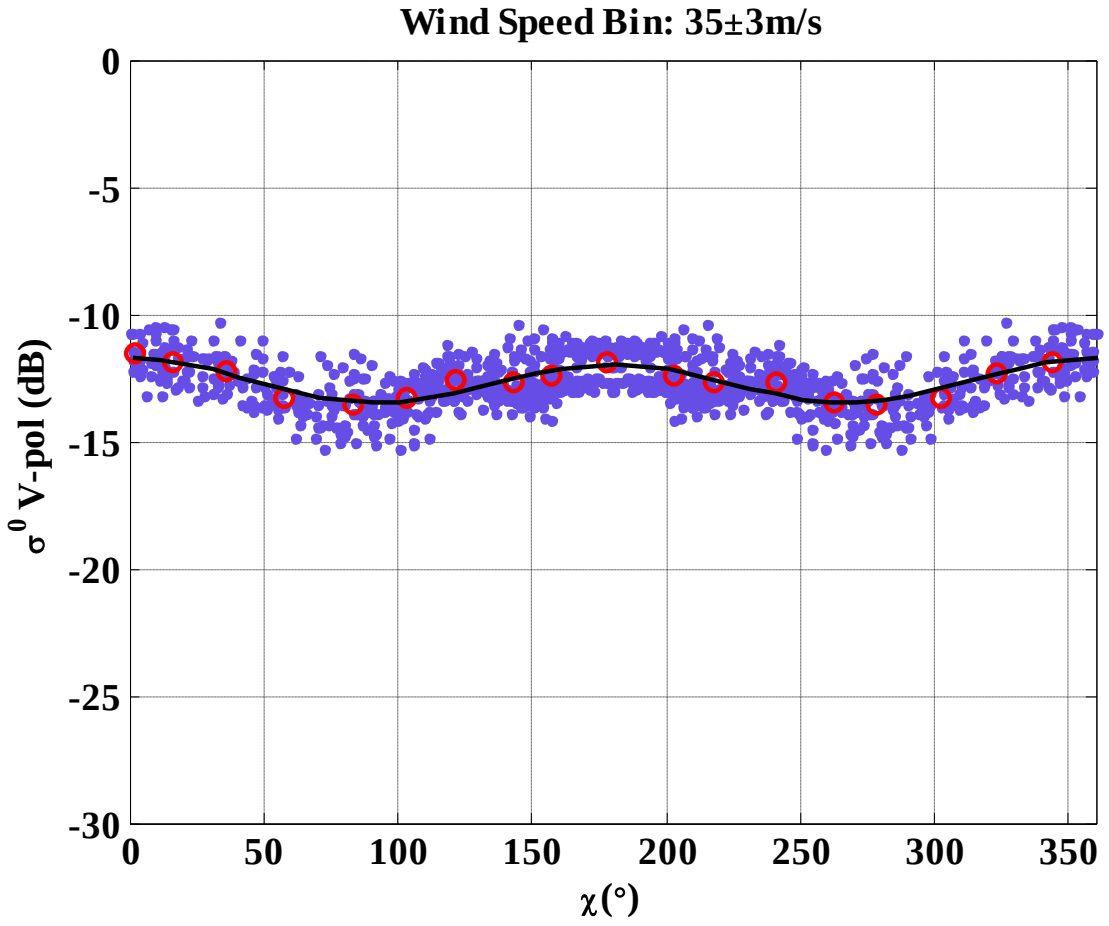


Fig. 3.17: V-pol ocean $\sigma^0$'s response to relative wind directions at wind speed bins of 35±3 m/s.

To extrapolate the GMF to higher wind speeds (> 35 m/s), we rely on airborne scatterometer measurements in hurricanes to provide guidance on the $\sigma^0$ saturation [31, 46]. For airborne Ku-band scatterometers, the ocean $\sigma^0$ increases proportionally to wind speed up to ~ 30 m/s and thereafter rapidly saturates at hurricane-force wind speeds. However, because of differences between airborne and satellite scatterometer absolute radar calibrations as well as antenna footprints (spatial scales), the $\sigma^0$'s do not directly apply; but, the assumption that both have similar ocean $\sigma^0$ saturation characteristics is valid. Given this, the XW-GMF is modeled to asymptotically approach a maximum value at similar wind speeds (50 - 70 m/s) as airborne scatterometers. Thus, to develop this GMF, the model coefficients dependences on wind speed were monotonically extrapolated up to approximately 70 m/s (see Figs. 3.18 – 3.23).

The principle effect of saturation is seen in the $C_0$ coefficient, which is modeled as a monotonically increasing logarithmic function that is extrapolated for the wind speeds in excess of 35 m/s (see Figs. 3.18 H-pol & 3.21 V-pol). On the other hand, $C_1$ initially increases at low wind speeds and after wind speeds ~ 15 – 20 m/s it asymptotically approaches zero at high wind speeds. To capture this dependence, $C_1$ is modeled as a rational function (ratio of two polynomials) and assumed to gradually diminish at high wind speed (Figs. 3.19 H-pol & 3.22 V-pol). This rational function provides a reasonable fit to the data, i.e., it offers a smooth transition and is representative of the qualitative dependence of EM theory. Finally, $C_2$ gradually decreases with wind speed and asymptotically approaches zero as the ocean surface becomes more isotropic (exhibits less wind directional anisotropy) in extreme wind conditions (Figs. 3.20 H-pol & 3.23 V-pol). The XW-GMF coefficients are tabulated in Table 3.2.

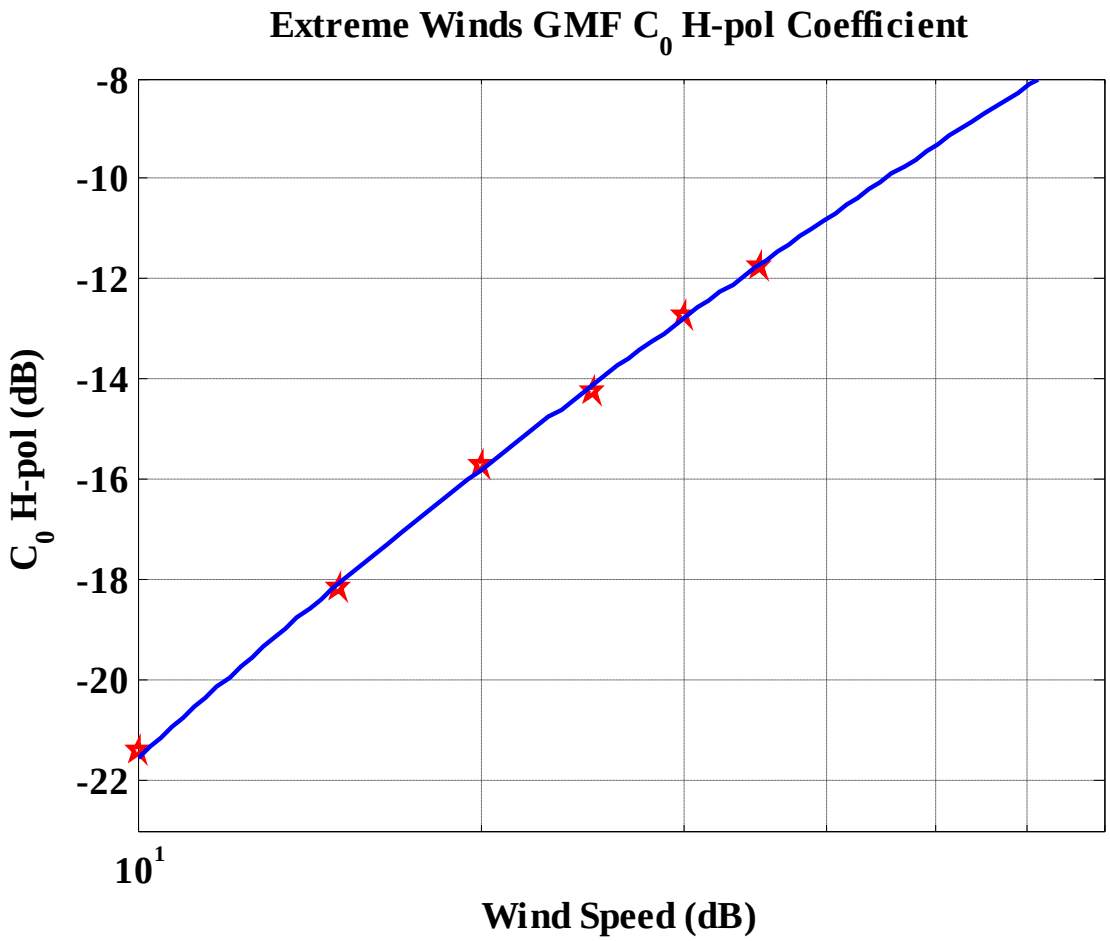


Fig. 3.18: XW-GMF $C_0$ coefficient for H-pol.

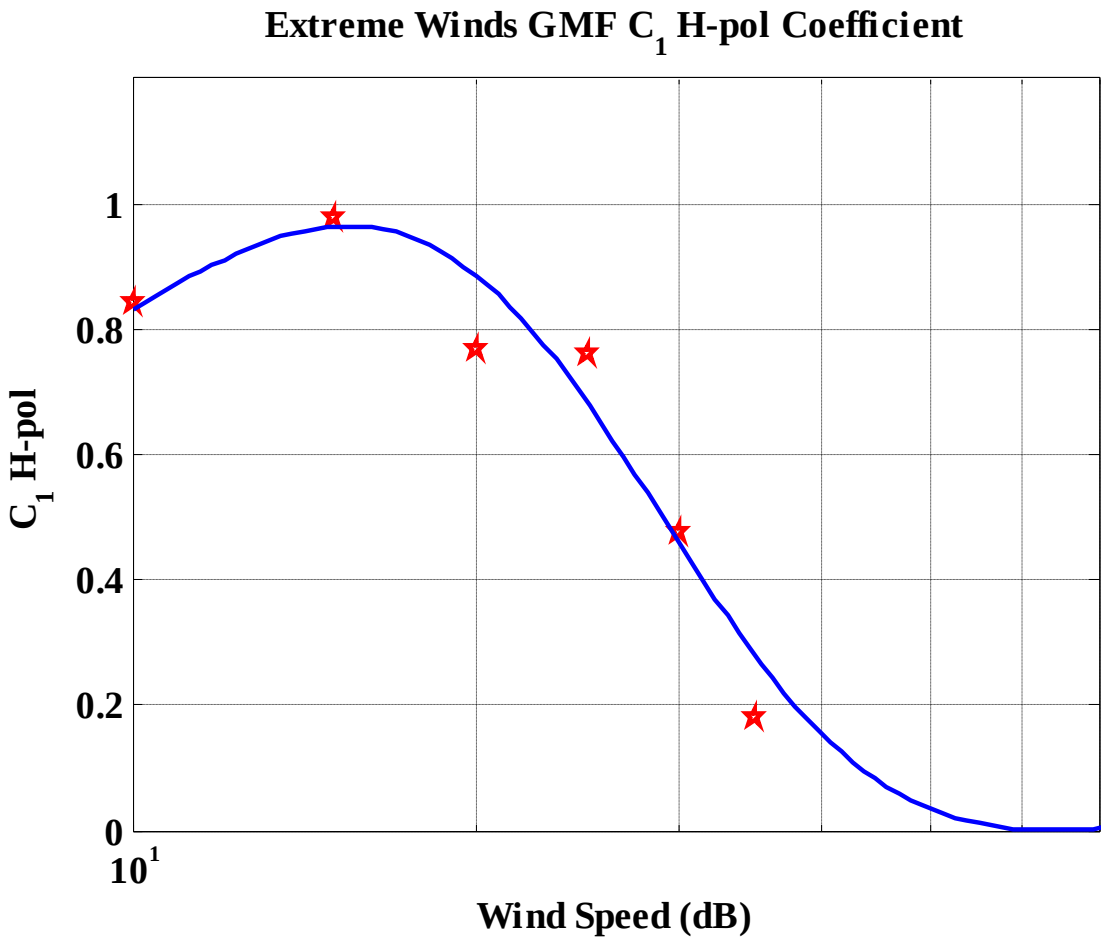


Fig. 3.19: XW-GMF $C_1$ coefficient for H-pol.

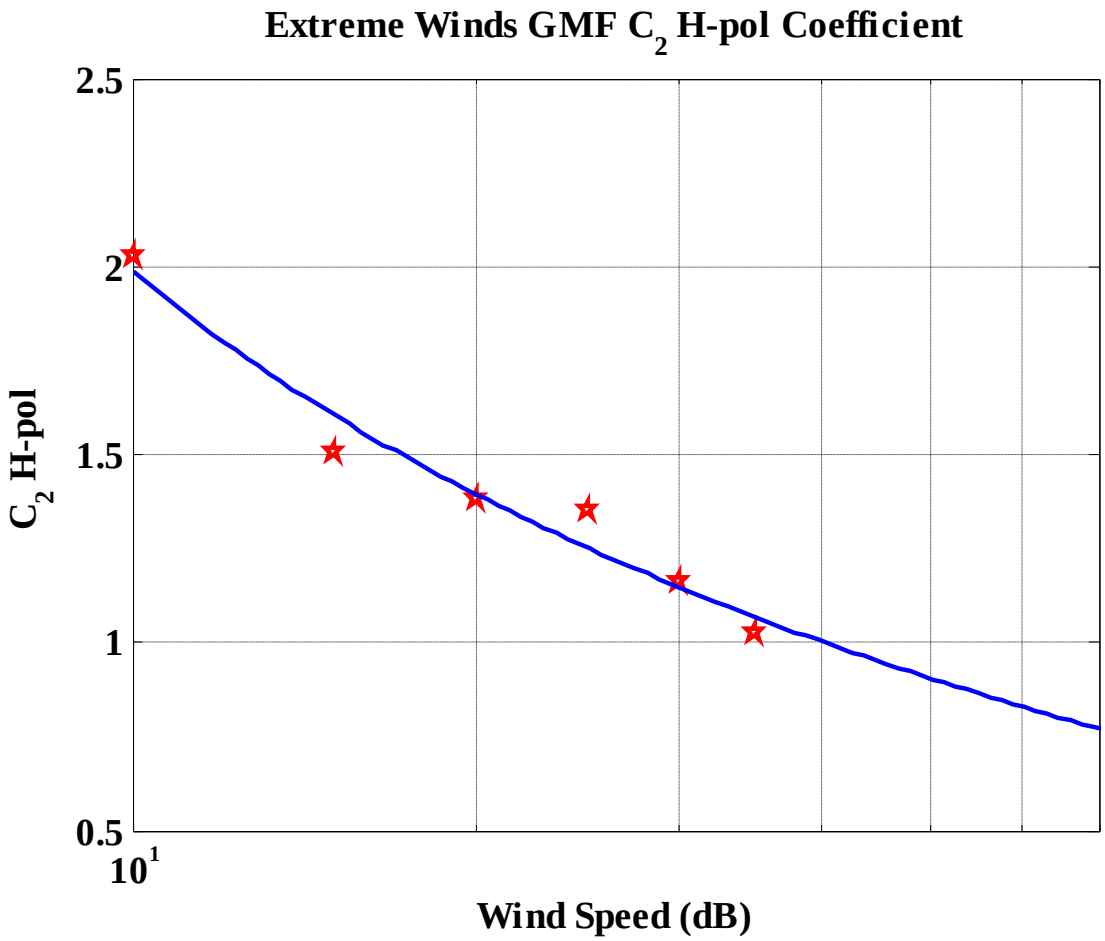


Fig. 3.20: XW-GMF $C_2$ coefficient for H-pol.

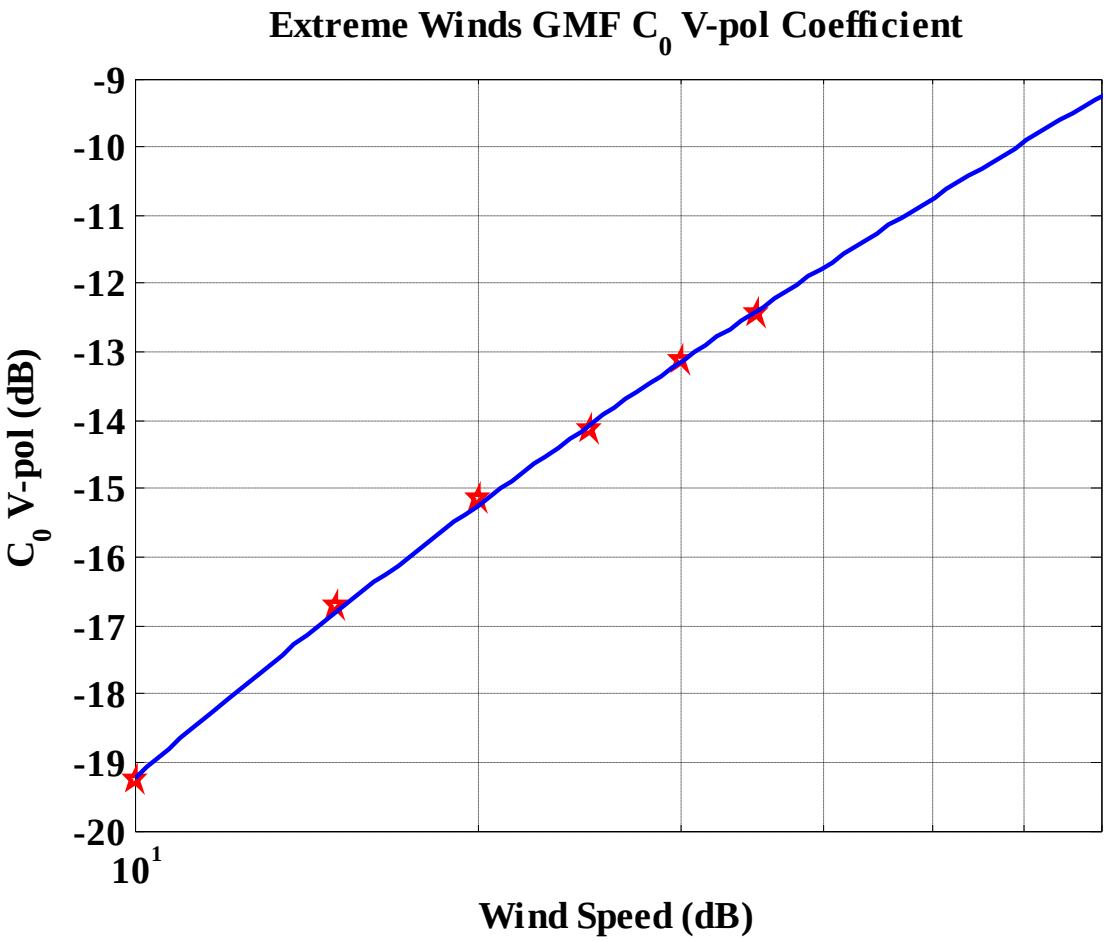


Fig. 3.21: XW-GMF $C_0$ coefficient for V-pol.

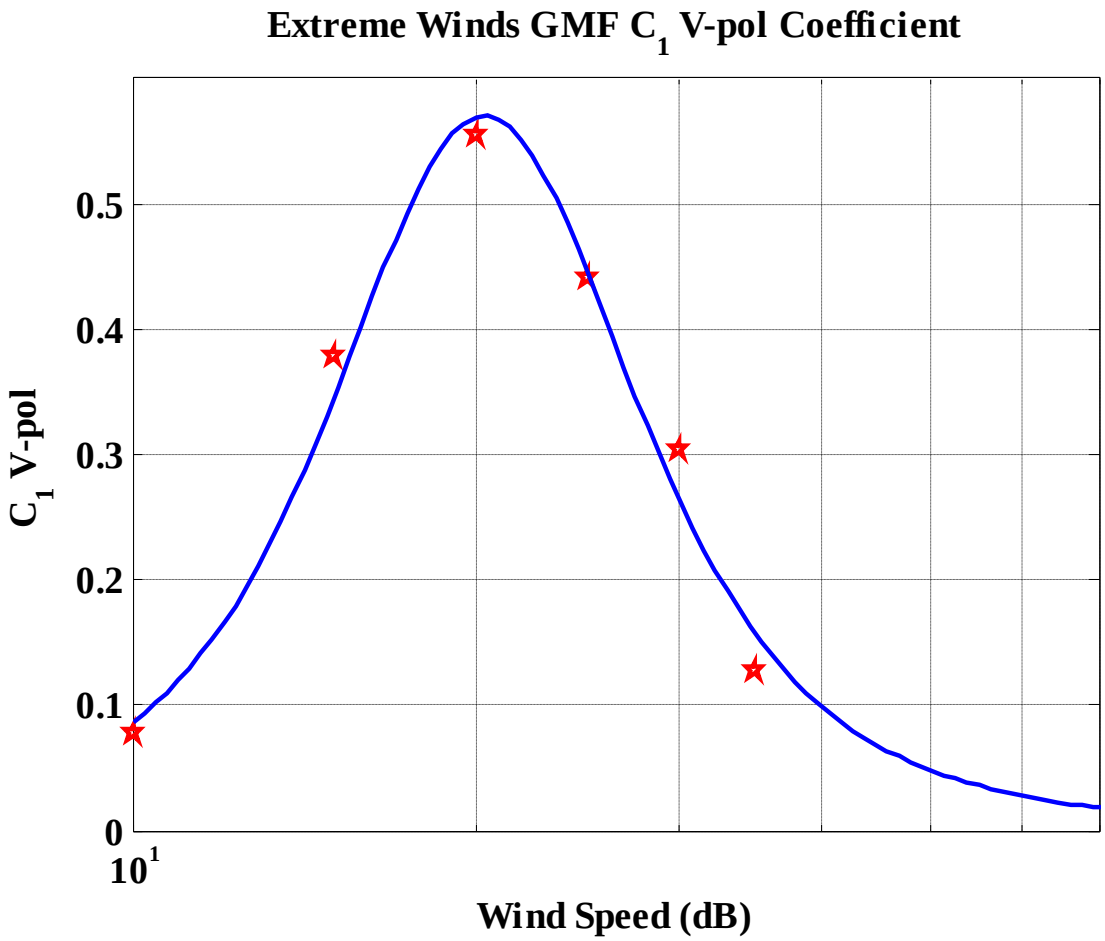


Fig. 3.22: XW-GMF $C_1$ coefficient for V-pol.

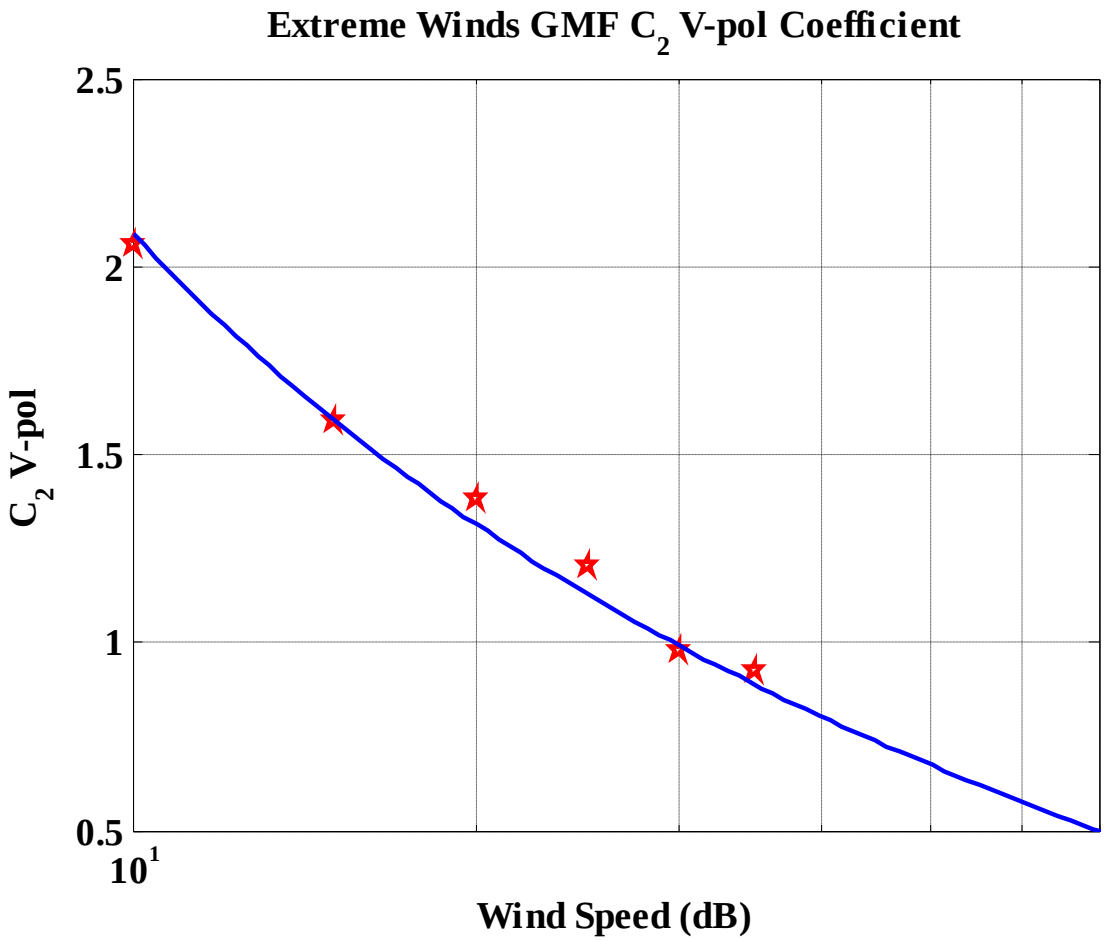


Fig. 3.23: XW-GMF $C_2$coefficient for V-pol.

Table 3.2. Extreme Winds GMF coefficients

| | | | |
|---|---|---|---|
| H-pol | $C_0$ | a = -45.3813<br>b = 4.4945 | $C_0 = a + b\,(\ln(ws))^2$ |
| | $C_1$ | a = 0.4136<br>b = -0.1207<br>c = -0.0229<br>d = 0.0041 | $C_1 = \left(\frac{a + c \cdot ws}{1 + b \cdot ws + d \cdot ws^2}\right)^2$ |
| | $C_2$ | a = -3.7990<br>b = 13.3217 | $C_2 = a + \frac{b}{\ln ws}$ |
| V-pol | $C_0$ | a = -35.7483<br>b = 3.1166 | $C_0 = a + b\,(\ln(ws))^2$ |
| | $C_1$ | a = 0.0249<br>b = -0.1477<br>c = 9.6550<br>d = 0.0057 | $C_1 = \left(\frac{a + c \cdot ws}{1 + b \cdot ws + d \cdot ws^2}\right)^2$ |
| | $C_2$ | a = 1.6451<br>b = -0.0207 | $C_2 = a + \frac{b}{\ln ws}$ |

The XW-GMF is compared with the SeaWinds project's QuikSCAT GMF (QS-GMF) at various wind speeds ranges as shown in Fig. 3.24. For wind speeds < 15 m/s, both GMF's are quite similar; however, at higher wind speeds they are noticeably different. The QS-GMF assigns higher $\sigma^0$ than XW-GMF, which results in lower retrieved wind speeds during the MLE wind vector retrieval process. For example, consider a measured $\sigma^0$ = -12 dB: for $\chi$ at 100°, QS-GMF corresponds to a wind speed of 26 m/s; whereas XW-GMF corresponds to 32 m/s.

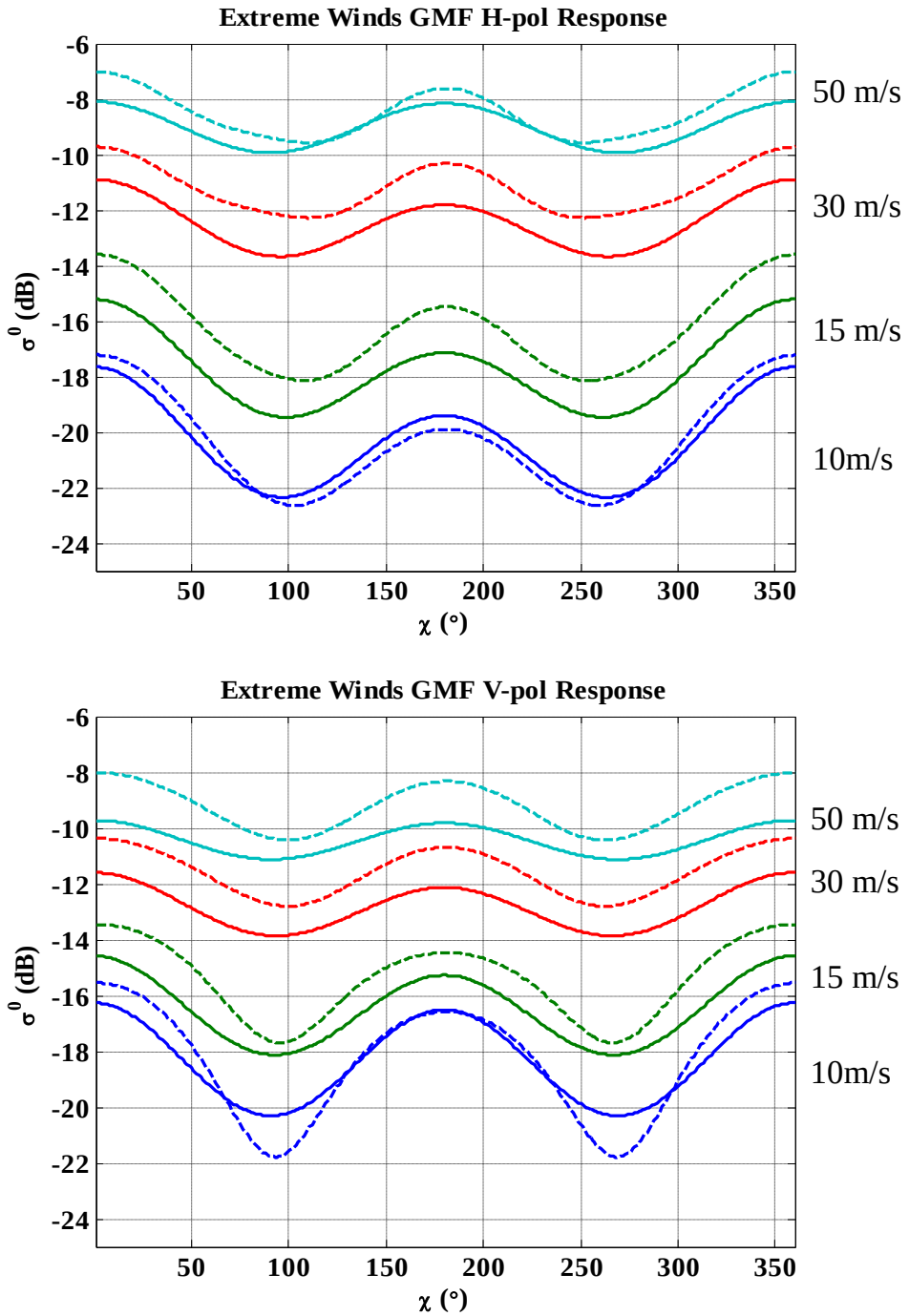


Fig. 3.24: Ocean sigma-0 response for QuikSCAT GMF (QS-GMF) and Extreme Winds GMF (XW-GMF). Broken lines denote the QS-GMF and solid lines denote the XW-GMF. Top panel is H-pol and bottom panel is V-pol.

### *3.3.4 Hurricane Wind Vector Retrieval*

Once $\sigma^0$ measurements are corrected for rain effects, they are grouped into an assigned WVC and input to the wind vector retrieval process to determine the possible wind vector solutions. The wind vector retrieval algorithm is based on the traditional MLE wind vector retrieval approach [49], which minimizes the mean square difference between $\sigma^0$ measurements and modeled $\sigma^0$'s for assumed wind speeds and directions. Because of the periodicity of the GMF and noise corruption of $\sigma^0$ measurements, multiple solutions known as "ambiguities" will occur. Hence, a post estimation procedure called de-aliasing or ambiguity removal algorithm is applied in order to select a "single wind vector" solution.

A unique ambiguity removal algorithm is developed for Q-Winds hurricane retrieval. Whereas the QuikSCAT ambiguity removal procedure requires "nudging" from an independent wind field [50], Q-Winds is envisioned as a stand-alone hurricane retrieval algorithm. Hence, a special de-aliasing scheme was developed to exploit the unique characteristics of the TC, which has a known CCW rotation in the northern hemisphere (CW in the southern hemisphere).

The alias selection or ambiguity removal algorithm for Q-Winds is an iterative procedure, which is performed on a WVC basis and involves nearest neighbor WVC's to identify "improbable wind directions" and the select the "best wind direction" for the given WVC. The first step, known as "spiral de-aliasing", operates on the output of the MLE retrieval module, which

comprises the field of "all possible aliases" wind direction solutions for each WVC. This procedure begins by superimposing an "initial guess" CCW twenty degree [51] inward spiral wind direction model field about the *a priori* storm center provided by NHC "best track" location [52]. An example of this is shown in Fig. 3.25, where for each WVC, the improbable wind direction aliases are identified and eliminated from consideration if their directions differ by more than ±75° from the spiral model wind direction. This procedure usually eliminates about half of the "possible solutions" and the "solution candidates" are the aliases who survived the initial CCW reference filtering process (see Fig. 3.26).

The next step performs a scalar wind direction (modulo 360°) average of the (two) available aliases in each WVC; after which, this is subjected to a median filter with a window size of 5 × 5 to become the "first guess" wind direction field (see Fig.3.27).

The final step of alias selection is to compare this "first guess" wind direction field with the initial solution candidates (after spiral de-aliasing shown in Fig. 3.36). The "best selected" direction for the WVC (see Fig.3.28) is the alias that is closest in direction to the "first guess" wind field.

An example wind direction selection for a SeaWinds hurricane overpass is shown in Fig. 3.29. Although, the development of this algorithm is *ad hoc*, nevertheless, the final selections are very realistic and compare well with the H*Wind directions to be shown in Chapter-IV.

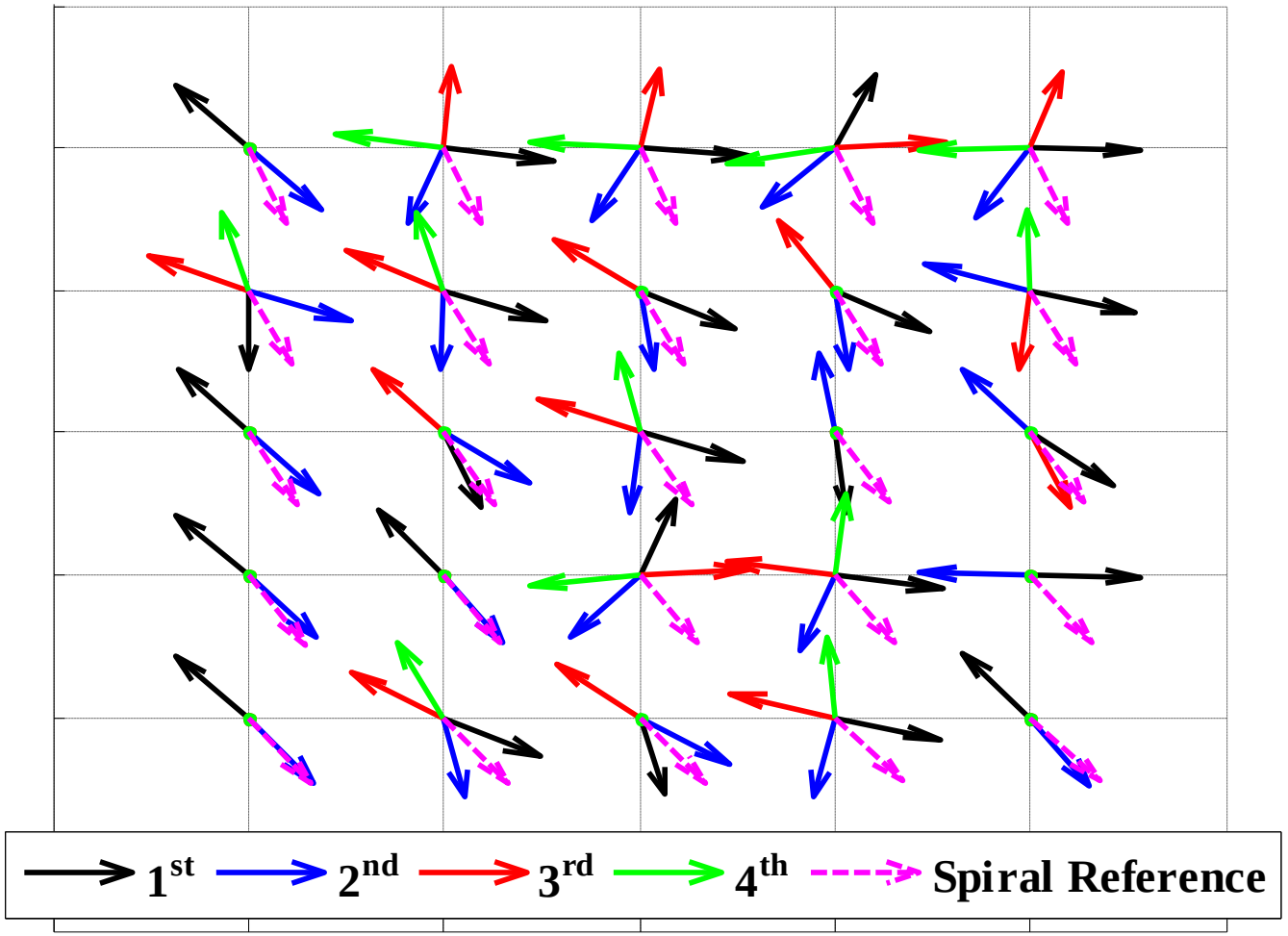


Fig. 3.25: Example of spiral de-aliasing of "all possible aliases" using a CCW spiral wind direction technique.

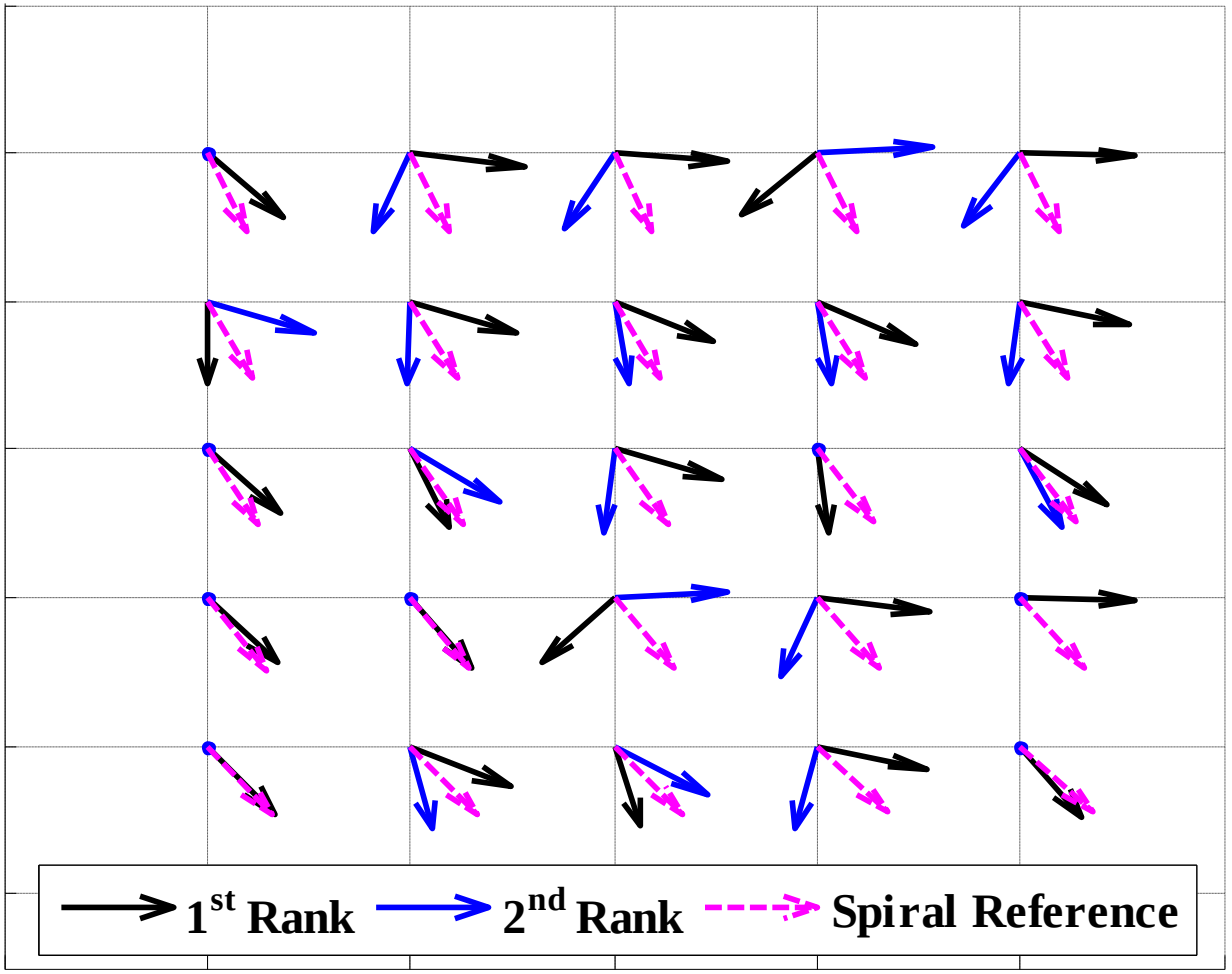


Fig. 3.26: Solution candidates after spiral de-aliasing.

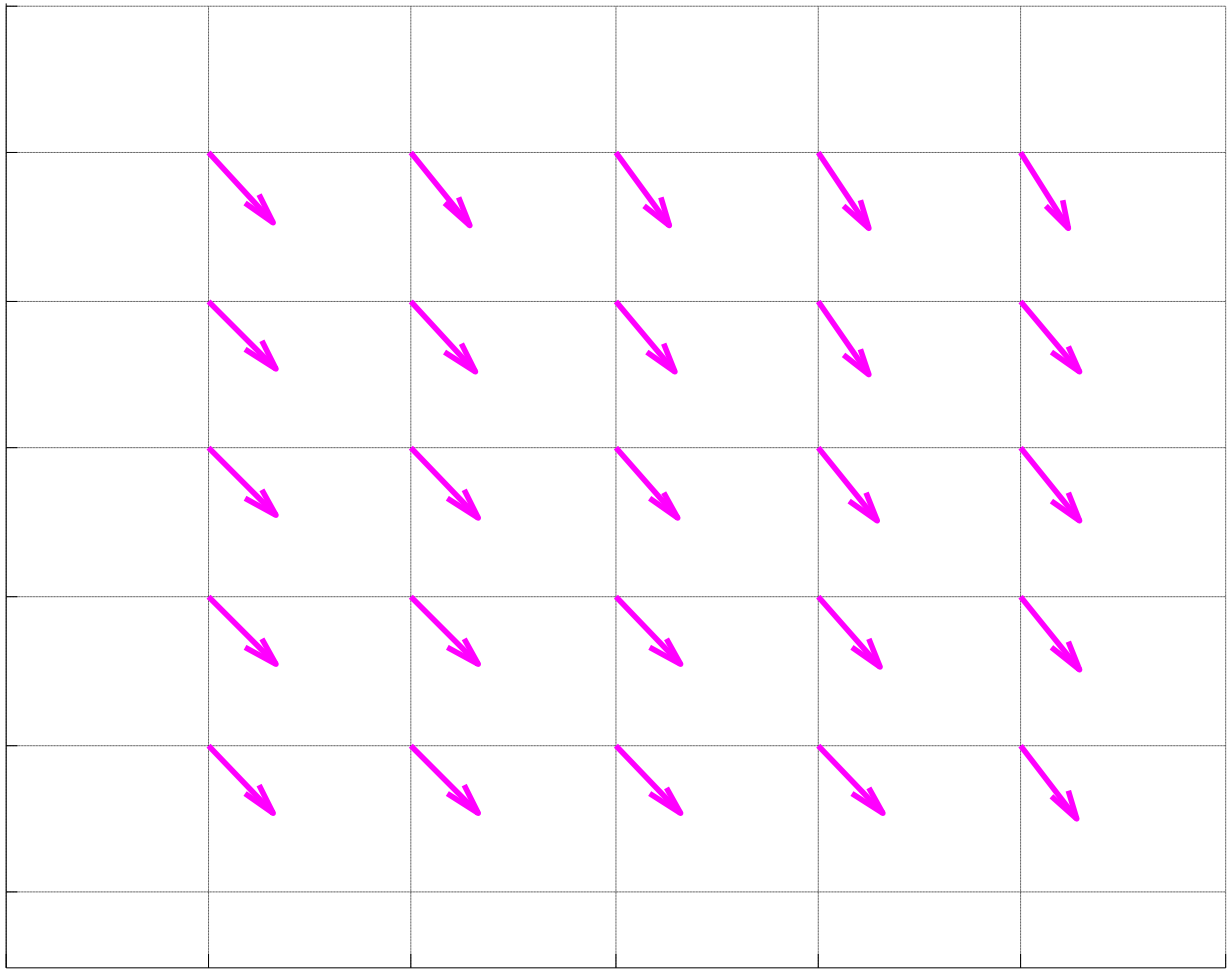

Fig. 3.27: First guess wind direction field after scalar modulo-360 deg wind direction averaging and median filtering using a window size of 5 × 5 wind vector cells.

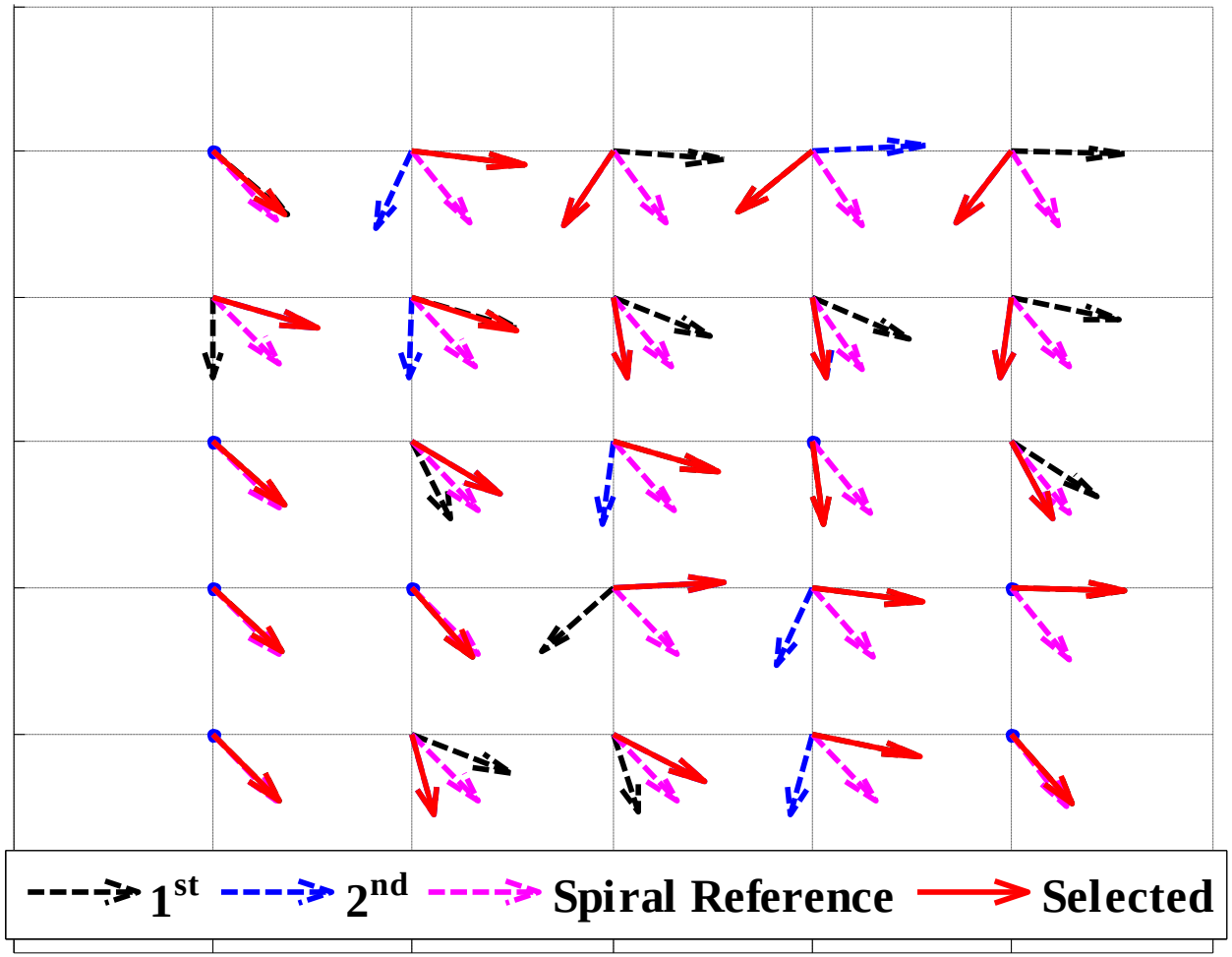


Fig. 3.28: Unambiguous “Selected” wind direction.

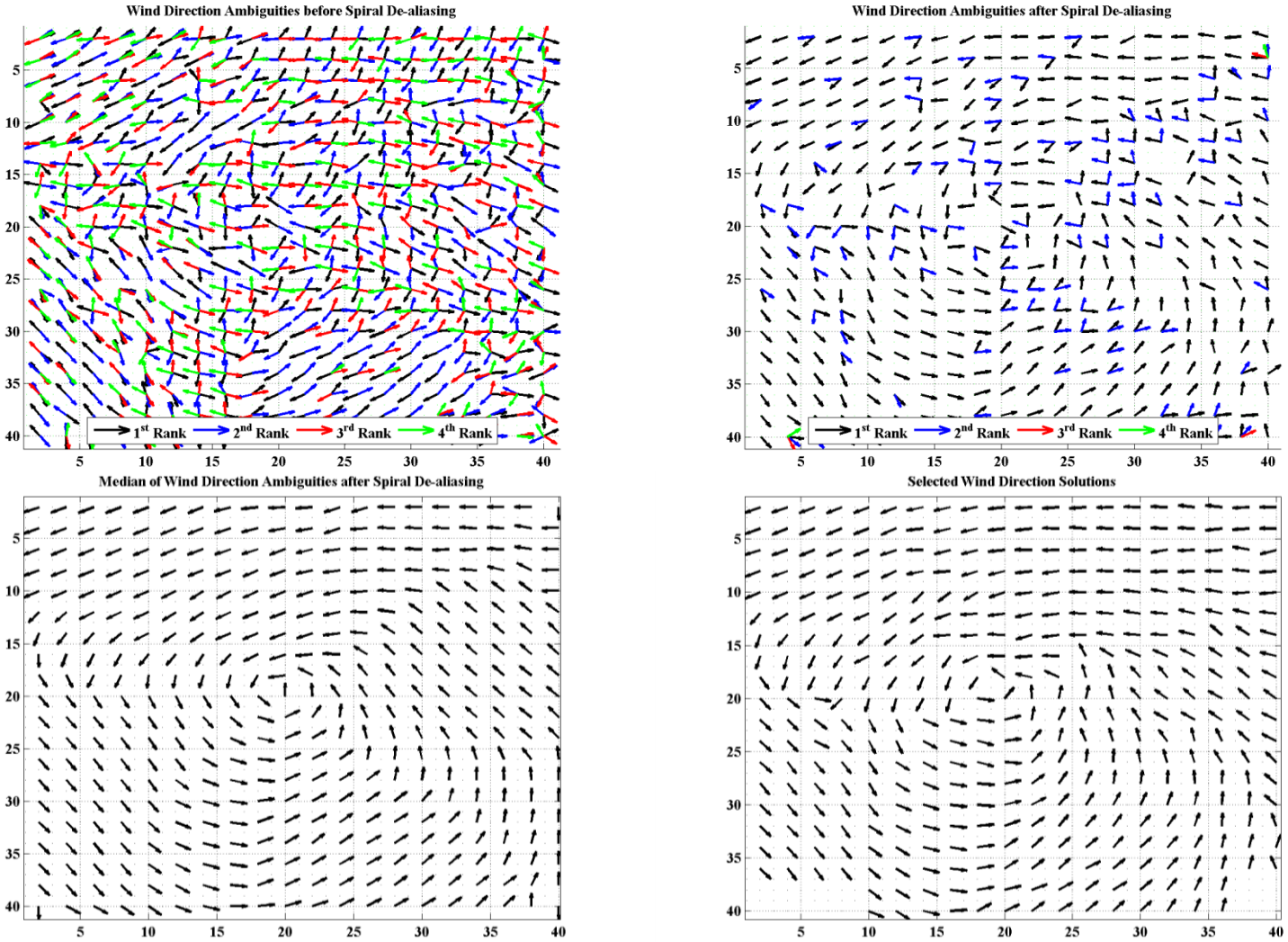


Fig. 3.29: Wind direction ambiguities selection. Upper left panel is all solutions before spiral de-aliasing, upper right is candidate solutions after spiral de-aliasing, bottom left is the "first guess" directions field, and lower right is the selected alias closest to first guess field.

Once the ambiguous hurricane wind vector field has been de-aliased, then a wind speed median filtering process is applied over a 3 × 3 window (37.5 km box) to the WVC's to reduce the variance of the wind speed retrieval. In the Q-Winds hurricane retrieval algorithm, the size of the smoothing window is selected for an optimum blend of variance reduction and maintaining spatial resolution.

### *3.3.5 Quality Flagging*

As a final quality assurance step in Q-Winds hurricane retrieval, QC "excessive rain" flags are produced to identify low confidence pixels. These flags are derived empirically from the QRad Tb (preferably H-pol except at the outer swath edges where only V-pol exists), which is very effective in distinguishing between rain and clear atmospheric conditions.

The optimum flagging algorithm is designed to eliminate suspect WVC elements while preserving the high wind speed pixels. Unfortunately, high wind speed is almost always associated with intense rain rate (brightness temperature). Its correlation is presented in Fig. 3.30, where Q-Winds retrieved wind speeds are compared against collocated H*Wind surface truth speed using colored symbols (QRad Tb H-pol color bar). The vertical lines represent hurricane wind speed categories 1 – 5, respectively, left to right. This figure shows that for wind speeds less than hurricane-force (< ~35 m/s), the results generally correspond to Tb H-pol of < 150 K (dark and light blue dots). Extreme wind speeds (e.g., hurricane force wind) are typically plotted in warm colors where the Tb H-pol exceeds 150 K, which corresponds to strong rain rate.

Further, note that for wind speeds > 40 m/s most Q-Winds retrievals badly under-estimate the true wind speeds, and these are also colored with warm colors corresponding to high Tb's with rain. Therefore, eliminating strong rain with a QC flag based upon Tb also removes most of the desirable high wind speeds pixels.

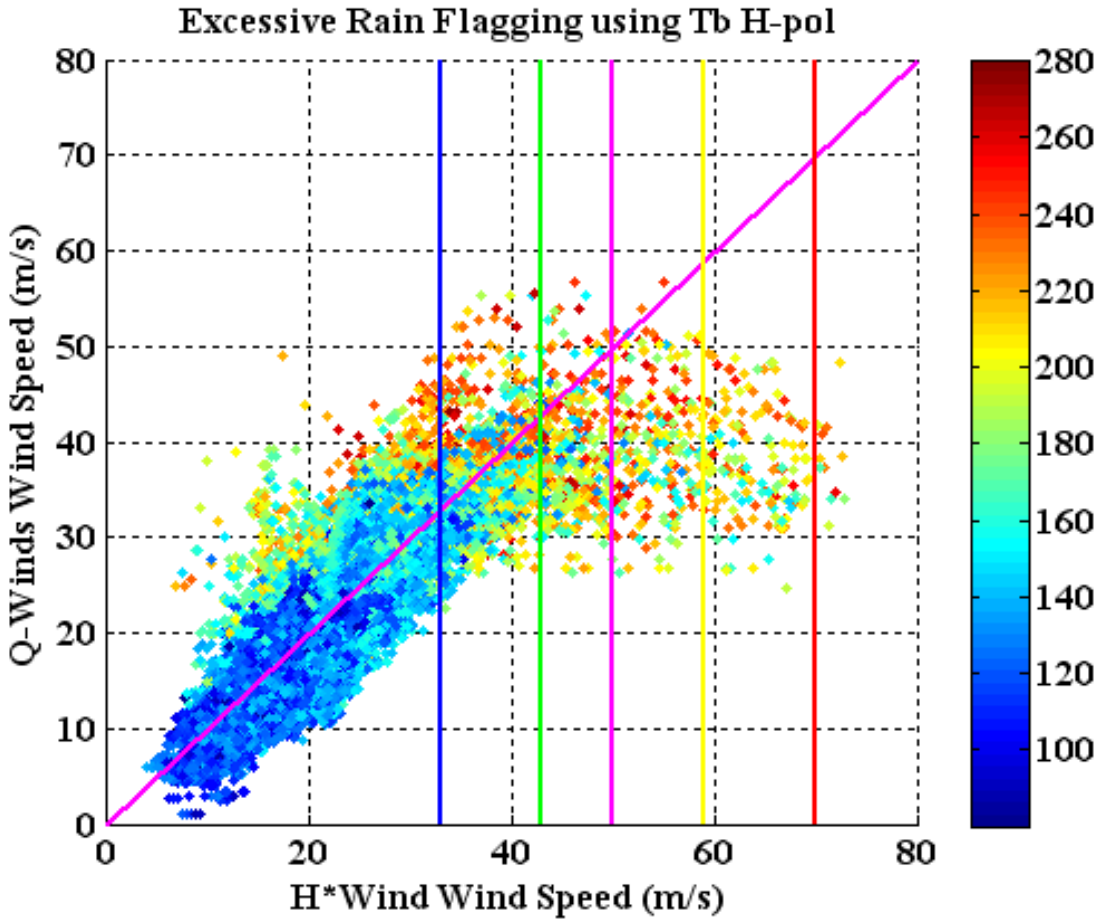


Fig. 3.30: Wind speed comparisons with corresponding Tb H-pol dependence. Colorbar is Tb H-pol in K. The vertical lines are hurricane categories 1 to 5.

To derive the optimal QC excessive rain flag cutoff (Tb H-pol threshold), a tradeoff between retrieval accuracy and number of flagged elements were assessed and this is displayed in Fig. 3.31. The normalized root-mean-square error (RMSE) of the wind retrieval (RMSE/mean-wind-speed) and flag percentage were plots as function of Tb H-pol. The Tb H-pol threshold of 190 K was selected to restrict the normalized RMSE of the retrieval accuracy under 25% and flagging percentage of ~15%. This flagging threshold preserves wind speeds of at least 42 m/s (hurricane category-2) and limits the wind speed error compared to H*Wind within 10% of hurricane category-5 (70 m/s).

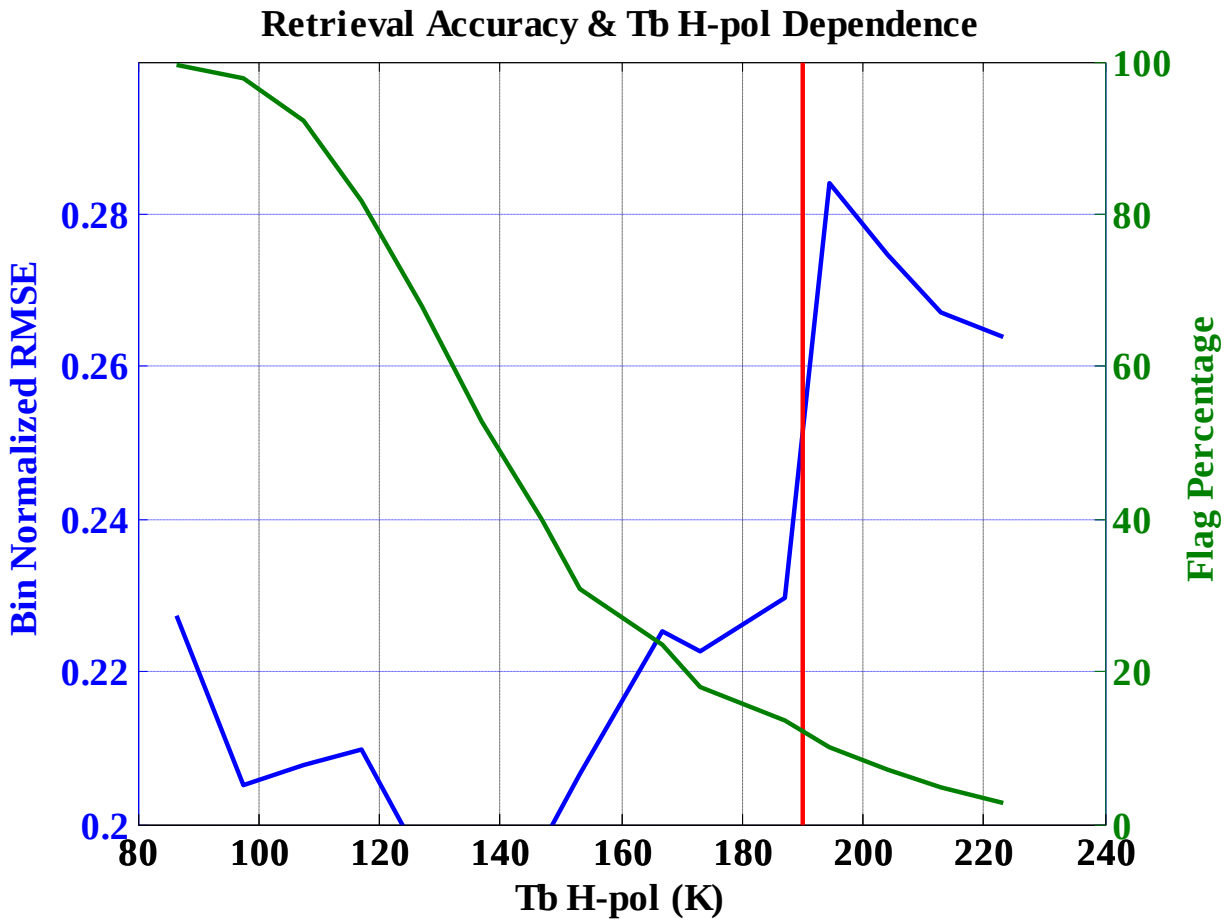


Fig. 3.31: Wind speed retrieval accuracy and flagged area tradeoff evaluation. The vertical line is the selected cutoff threshold.

## 3.4 Summary

The CFRSL Q-Winds hurricane retrieval algorithm is unique in several aspects. First, the contribution from the passive QRad Tb's are useful in providing a rain effects correction routine and also in providing a QC "excessive rain flag". This rain correction procedure is expected to partially resolve the typical observed underestimation of actual hurricane wind speed by scatterometer wind retrieval. Second, the XW-GMF is especially trained to measure hurricane peak wind speeds, which significantly raises the scatterometer maximum retrieved wind speed. Finally, the use of wind direction nudging from a spiral TC wind model improves the alias removal process.

In the next Chapter, the results of algorithm assessments will be presented. The Q-Winds output will be evaluated against other independence measurements and the current standard OVW product.

# CHAPTER-IV: EVALUATION OF Q-WINDS HURRICANE WIND VECTOR RETRIEVAL ALGORITHM

## 4.1 Introduction

This chapter is devoted to the evaluation of the performance of the Q-Winds hurricane wind vector retrieval algorithm. The Q-Winds performance evaluation is assessed by comparing Q-Winds retrievals with independent surface wind fields. Furthermore, a three-way comparison of CFRSL Q-Winds, JPL QuikSCAT L2B-12.5km winds, and the HRD H*Wind surface analysis is performed.

The results presented include comparisons of wind speed, wind direction, and hurricane wind threshold radii. Also examined are the effect of the GMF and rain correction on wind retrievals, and QC flags assessments. Among all these criteria, the wind speed is considered the most important. Statistical performance metrics are assessed and summarized; and hurricane OVW image comparisons are also presented. The overall OVW retrieval statistics presented in this chapter are based on a composite eighteen hurricane events from year 2001 – 2005. Because of the distinctiveness of each hurricane event, they were analyzed individually; but only results for four representative hurricane events are presented for per-rev basis. The hurricane events used in the research are summarized in Table 4.1.

Table 4.1: Hurricane information

| Name | Category* | Rev | Asc/Desc | Date | Time | Center (°N,°W) |
|---|---|---|---|---|---|---|
| Humberto | C1 | 11805 | D | 09/24/01 | 23:04 | (36.63,64.44) |
| Lili | C1 | 17094 | D | 09/30/02 | 23:16 | (20.45,80.98) |
| Lili | C3 | 17116 | A | 10/02/02 | 11:39 | (24.36,88.26) |
| ****Fabian** | **C4** | **21898** | **D** | **09/02/03** | **21:49** | **(20.75,61.11)** |
| Fabian | C3 | 21927 | D | 09/04/03 | 22:36 | **(26.84,64.50)** |
| Isabel | C5 | 22041 | D | 09/12/03 | 22:30 | **(21.77,58.88)** |
| ****Isabel** | **C5** | **22055** | **D** | **09/13/03** | **22:04** | **(22.74,62.90)** |
| Ivan | C5 | 27210 | A | 09/09/04 | 10:22 | **(14.11,70.33)** |
| Ivan | C4 | 27217 | D | 09/09/04 | 22:51 | **(15.12,72.63)** |
| ****Ivan** | **C4** | **27253** | **A** | **09/12/04** | **10:45** | **(18.73,81.03)** |
| Ivan | C5 | 27260 | D | 09/12/04 | 23:12 | **(19.44,82.70)** |
| Ivan | C4 | 27289 | D | 09/14/04 | 23:59 | **(24.70,87.00)** |
| Jeanne | C2 | 27431 | D | 09/24/04 | 22:59 | **(26.35,74.04)** |
| Cindy | TS | 31481 | D | 07/05/05 | 23:48 | **(28.49,90.32)** |
| Dennis | C1 | 31531 | A | 07/09/05 | 11:21 | **(24.06,83.28)** |
| Katrina | C3 | 32230 | A | 08/27/05 | 11:52 | **(24.40,84.59)** |
| ****Katrina** | **C3** | **32237** | **D** | **08/28/05** | **00:16** | **(24.85,85.90)** |
| Katrina | C5 | 32251 | D | 08/28/05 | 23:50 | **(27.18,89.12)** |

**: Hurricane category is based on the Saffir-Simpson Hurricane Scale (SSHS) provided in Table 2.1 in Chapter-II.*

*****: Selected case presented in the Chapter-IV.***

## 4.2 Hurricane Surface Truth

Previously, HRD H*Wind surface analyses were used to evaluate WindSat surface wind vectors in hurricanes [53]; and in a similar manner, H*Wind analyses are used here to validate the QuikSCAT retrieved ocean wind vectors from the Q-Winds and L2B-12.5km OVW data products.

To achieve best estimate of the TC surface winds, the H*Wind analysis time was the time of the QuikSCAT overpass, and a subjective meteorological assessment was performed to assure that the storm intensity was in a reasonably steady-state condition over the time period from which aircraft and satellite observations are included. Further, the validation sets are carefully chosen such that only QuikSCAT overpasses with ample storm coverage were used. Further, for high quality H*Wind analyses only cases with near-simultaneous and dense data sampling from one or more reconnaissance aircraft were used. These multi-aircraft flights produced a wealth of AFRC, SFMR and GPS dropsondes data, giving us confidence that the uncertainties in our H*Wind analyses were on the low end of a 10% to 20% uncertainty range [54], which have been shown to be the most accurate OVW observations in a hurricane environment.

Despite of the merits of H*Wind analyses, caution is advised when it is used as “surface truth” for scatterometer validation. First, the accuracy of H*Wind is strongly depends on the quality of the observations, their temporal/spatial coverage relative to the satellite overpass, and the skills

and judgment of the analyst in selecting the applicable aircraft and satellite observations. Furthermore, due to the large spatial extent of hurricanes (typically > 800 km diameter), high quality surface winds are usually not available for the entire storm domain. Because, the H*Wind procedure utilizes interpolation to fill the analysis window, as a result, it often exhibits an unrealistic "symmetrical" wind field structure, which introduces error, typically in the outer regions of the storm.

## 4.3 Q-Winds Wind Speeds Evaluation

In this subsection Q-Winds wind speeds are evaluated and statistical results are presented. The study was based on the collection of eighteen QuikSCAT hurricane overpasses during years 2001 – 2005 with near-simultaneous aircraft underflights with high quality measurements, e.g., SMFR and GPS dropwindsondes. Q-Winds and L2B-12.5km OVW wind speed intensities and spatial distributions are compared to H*Wind. A qualitative assessment was performed through storm images comparison (Q-Winds, L2B-12.5km, and H*Wind); and a statistical evaluation was performed using mean binned-average wind speeds comparisons in scatter plots. At the end of this subsection, results are summarized in a table of the composite statistics determined from the eighteen revs. The mean wind speed error and standard deviation (STD) for each binned wind speed range are used as metrics for evaluation of Q-Winds hurricane wind vector measurement performance.

For illustrative purposes, Q-Winds and JPL L2B-12.5km wind speeds are compared with the HRD H*Wind surface wind speeds for four representative hurricane events. These are presented below in Figs. 4.1 – 4.4 as TC image comparisons. Each sub-panel is a hurricane image of a 5° by 5° latitude/longitude box with the hurricane eye centered at relative coordinates (20, 20), where the relative distance scale is 0.25° (~25 km) increments. Wind speeds are presented in a color scale ranges from 0 to 50 m/s; the arrows are the decimated wind direction quiver plots, which plot only one vector for two pixels. Further the white regions (missing data) are the regions where land masks or quality excess-rain flags are applied.

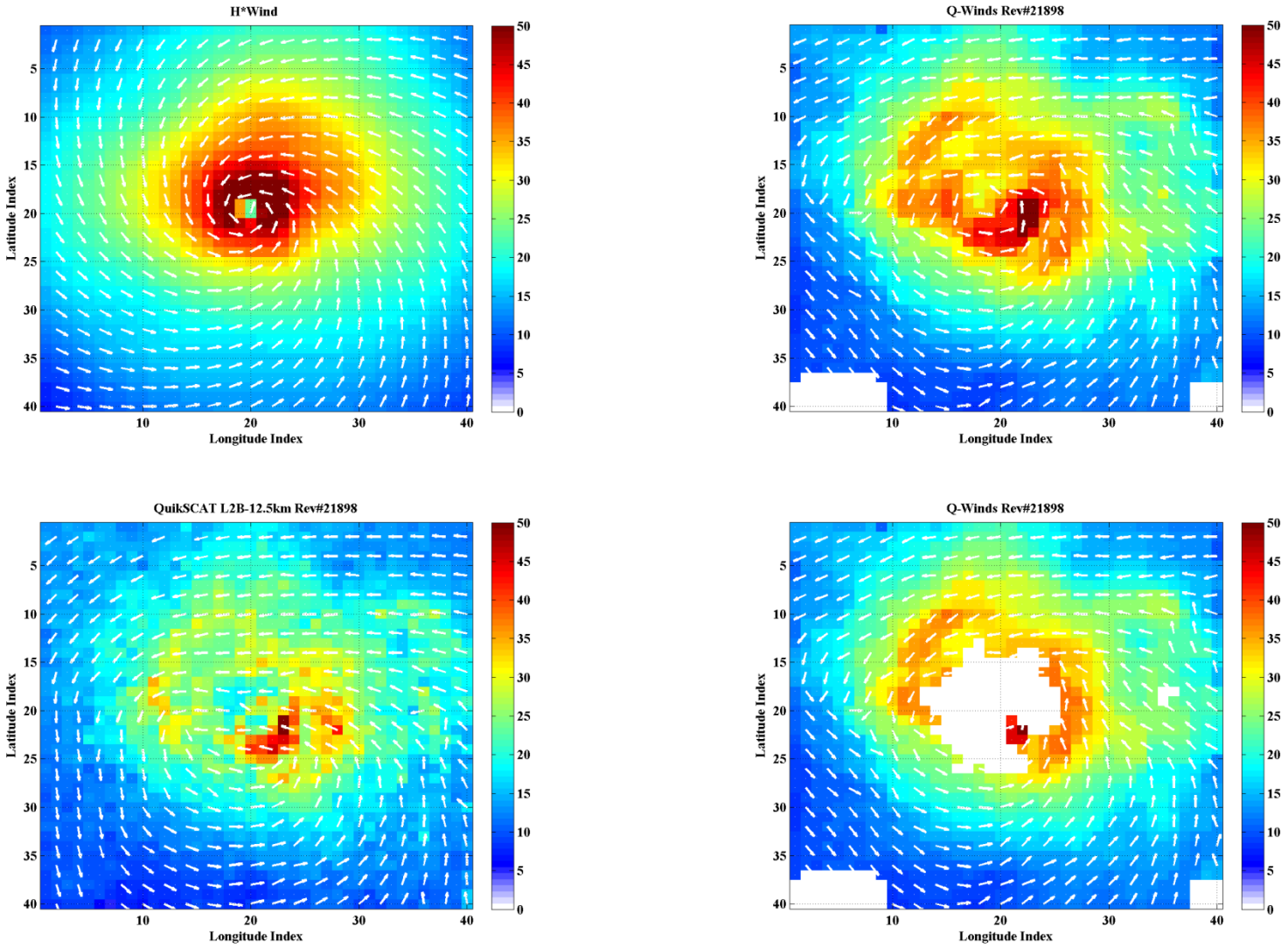


Fig. 4.1: Hurricane images for Hurricane Fabian (C4) rev#21898 on September 2nd, 2003, 21:49 UTC. H*Wind (upper left), Q-Winds (upper right), L2B-12.5km (lower left), and Q-Winds with rain flags (lower right).

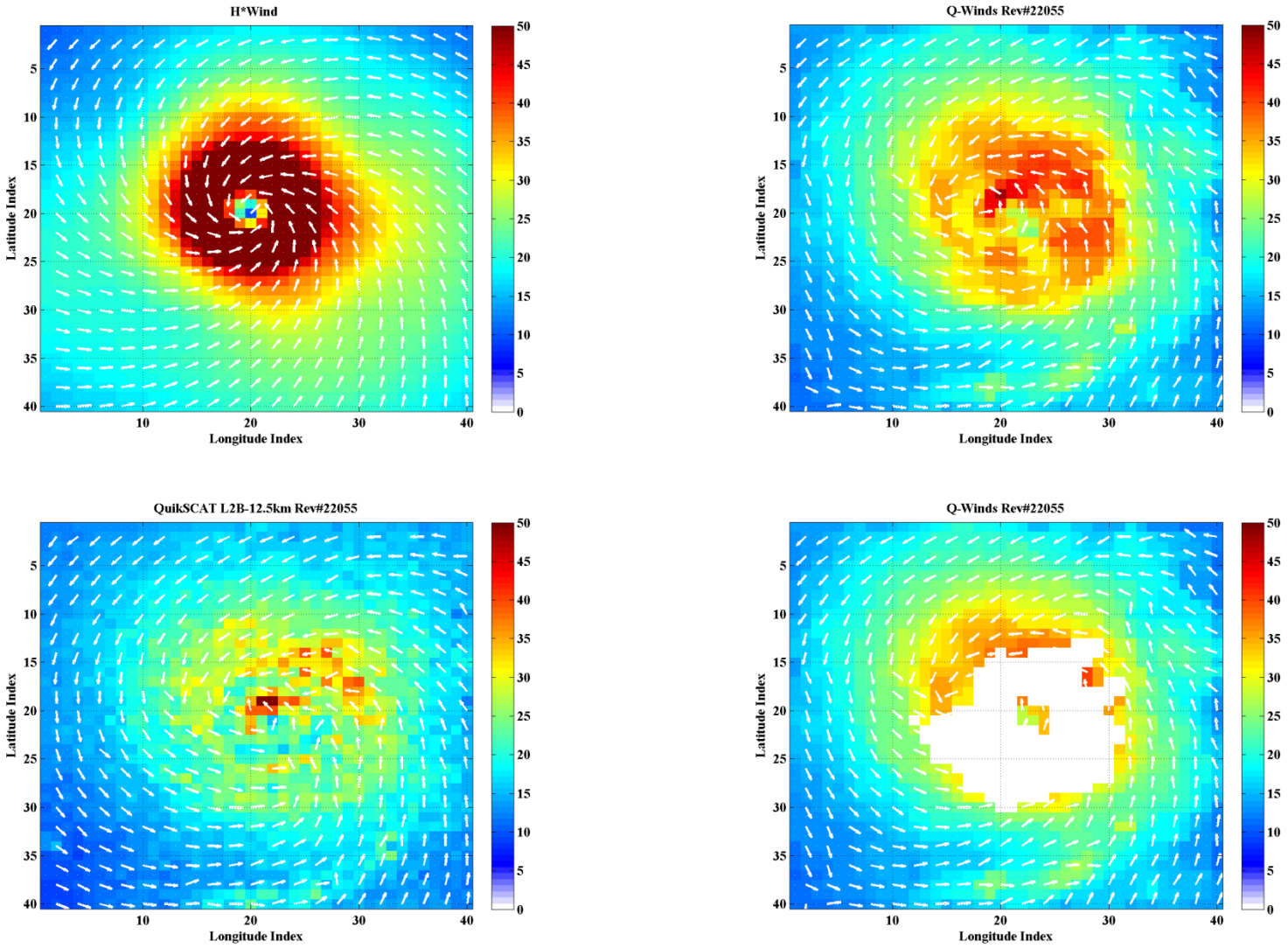


Fig. 4.2: Hurricane images for Hurricane Isabel (C5) rev#22055 on September 13th, 2003, 22:04 UTC. H*Wind (upper left), Q-Winds (upper right), L2B-12.5km (lower left), and Q-Winds with rain flags (lower right).

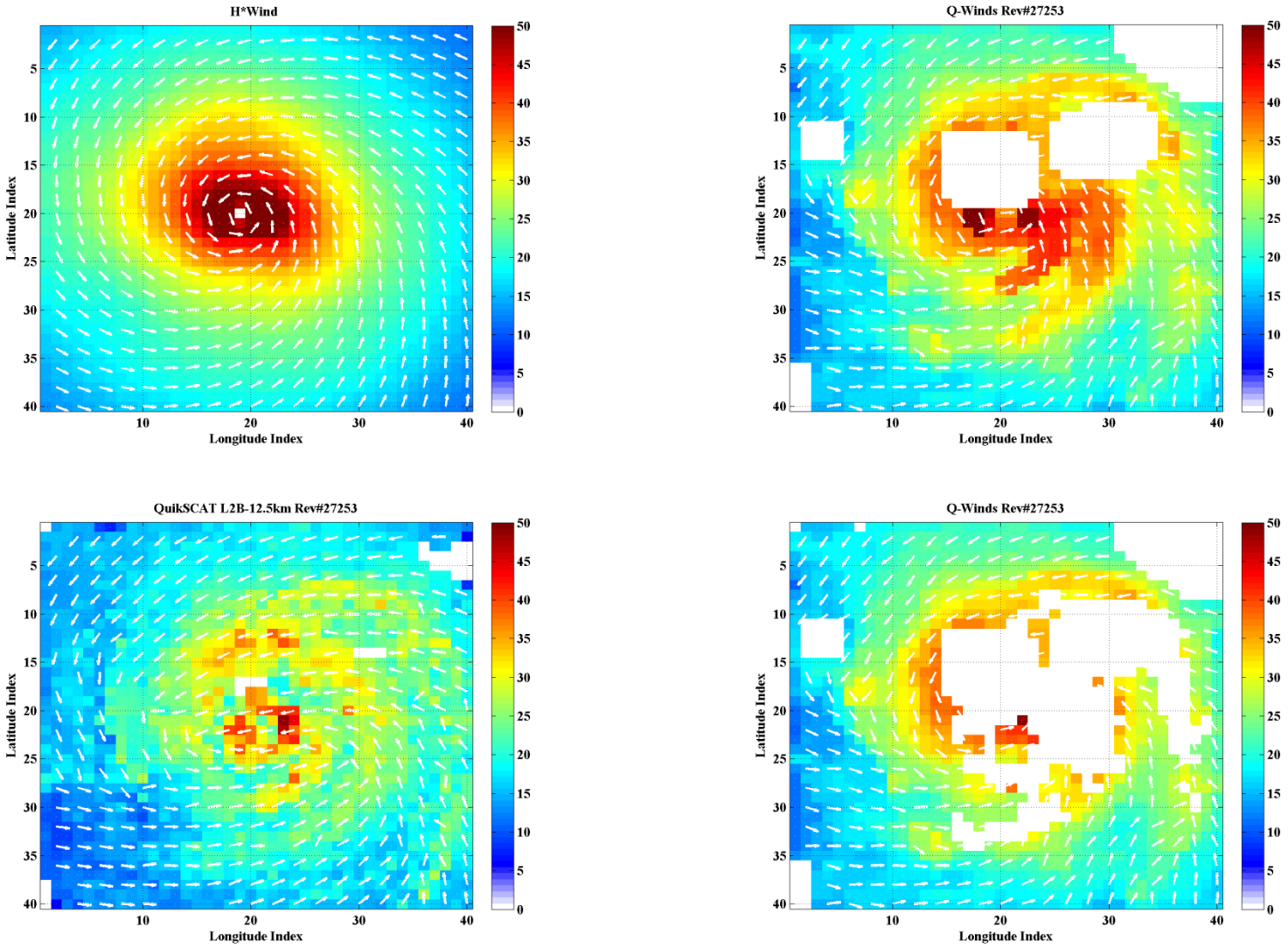


Fig. 4.3: Hurricane images for Hurricane Ivan (C4) rev#27253 on September 12nd, 2004, 10:45 UTC. H*Wind (upper left), Q-Winds (upper right), L2B-12.5km (lower left), and Q-Winds with rain flags (lower right).

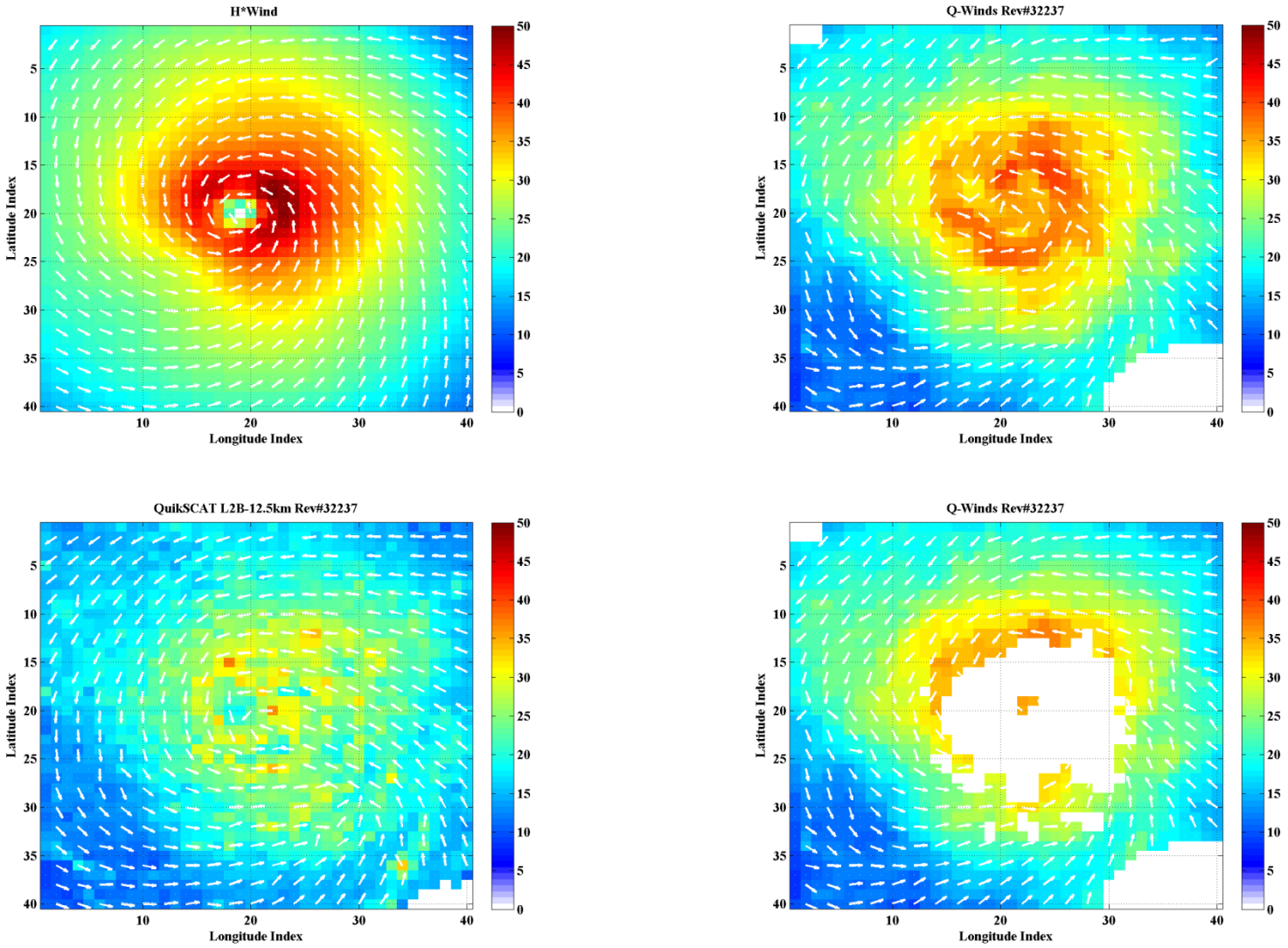


Fig. 4.4: Hurricane images for Hurricane Katrina (C3) rev#32237 on August 28th, 2005, 00:16 UTC. H*Wind (upper left), Q-Winds (upper right), L2B-12.5km (lower left), and Q-Winds with rain flags (lower right).

Although each OVW product shares some similarities, they are distinctive in detail. H*Wind tends to have a circular symmetric storm structure and smooth wind direction flow. In contrast, Q-Winds and L2B-12.5km wind fields, composed of retrieved wind vectors from independent 12.5 km WVC's, exhibit a more asymmetric shape. Furthermore, for H*Wind the low wind speed hurricane eye is clearly visible; however for Q-Winds and L2B-12.5km, because of their coarser instrument spatial resolution, the hurricane eye regions are more difficult to locate.

Overall, Q-Winds retrieves considerably higher wind speeds and agrees better with the H*Wind surface truth than does the L2B-12.5km product; which frequently severely underestimates the peak hurricane wind speed (especially when the wind speed exceeds hurricane force). The poor performance of L2B-12.5km can be attributed to both the QS-GMF and lack of rain (attenuation) correction. Because the QS-GMF was designed to measure the "average" wind speed, which exhibits $\sigma^0$ saturation for wind speeds above 32 m/s [46], it is not well-suited for TC conditions. Conversely, the Q-Winds' XW-GMF, which was tuned to the "peak" one-minute sustained wind speed from H*Wind, yields improved wind speed comparisons.

Because the peak wind intensity, size and the shape of the eye-wall varies for each hurricane event, each storm was analyzed separately. Binned-average wind speeds for Q-Winds and L2B-12.5km retrievals are compared to H*Wind surface wind analyses for the four representative hurricanes and results are shown in Figs. 4.5 – 4.8. These wind speed results are shown *via* scatter diagrams between Q-Winds (L2B-12.5km) and H*Wind, with density plots in "hot" colors representing dense (large #) populations. Symbols are the binned-average wind speed

values for Q-Winds with rain flags applied (blue) and of the corresponding values for L2B-12.5km (red).

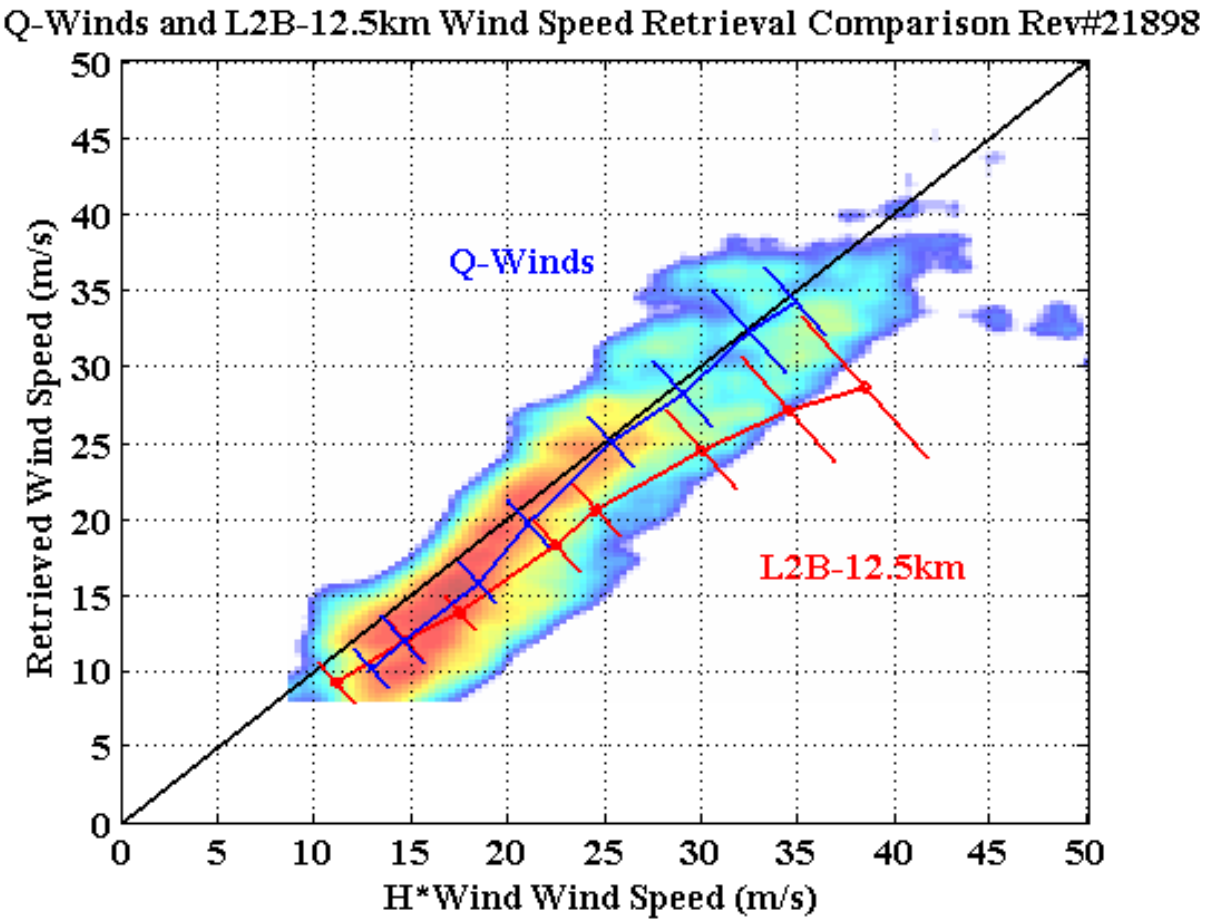


Fig. 4.5: Binned-average wind speed comparisons of Q-Winds and L2B-12.5km with H*Wind surface truth for Hurricane Fabian rev#21898. The blue symbols are Q-Winds with rain flags applied and the red symbols are the binned average wind speeds of L2B-12.5km.

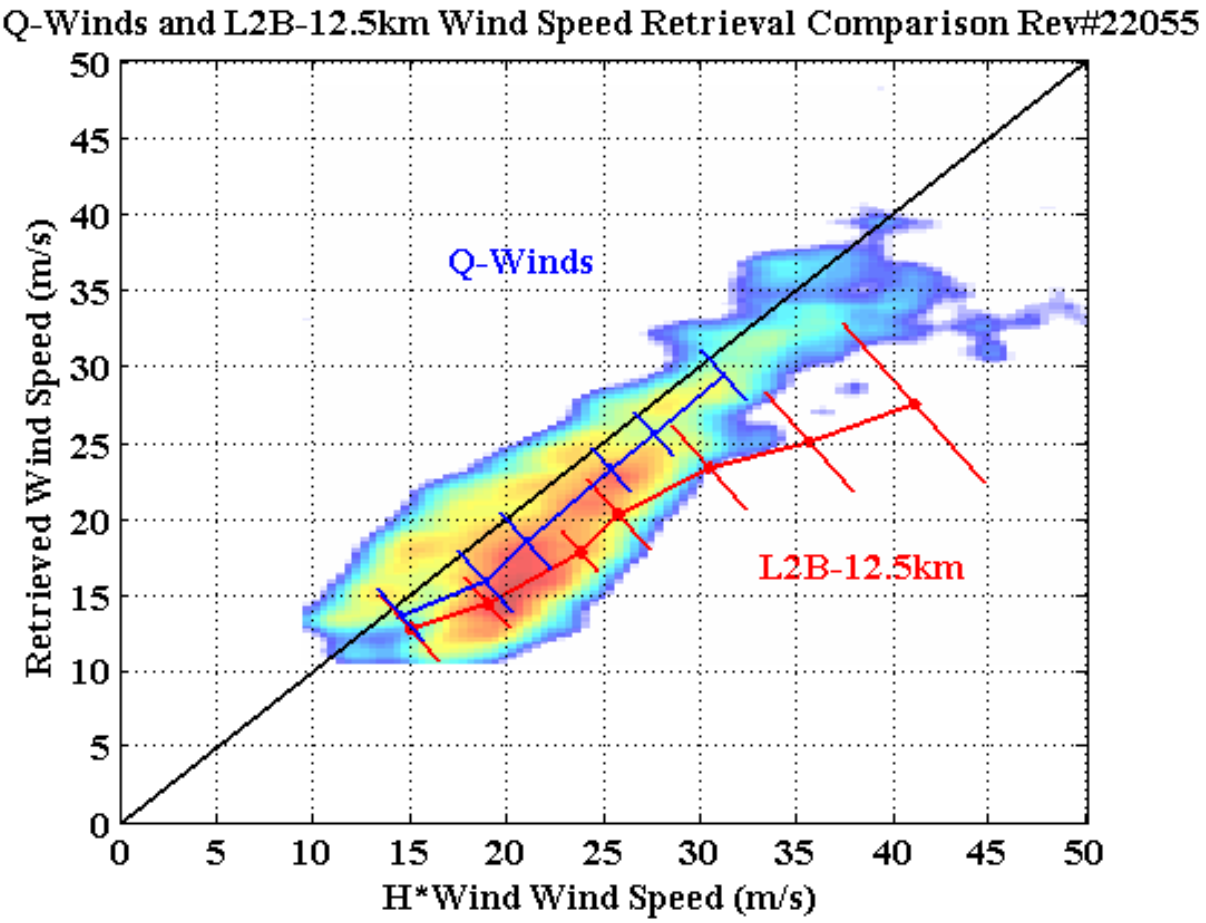


Fig. 4.6: Binned-average wind speed comparisons of Q-Winds and L2B-12.5km with H*Wind surface truth for Hurricane Isabel rev#22055. The blue symbols are Q-Winds with rain flags applied and the red symbols are the binned average wind speeds of L2B-12.5km.

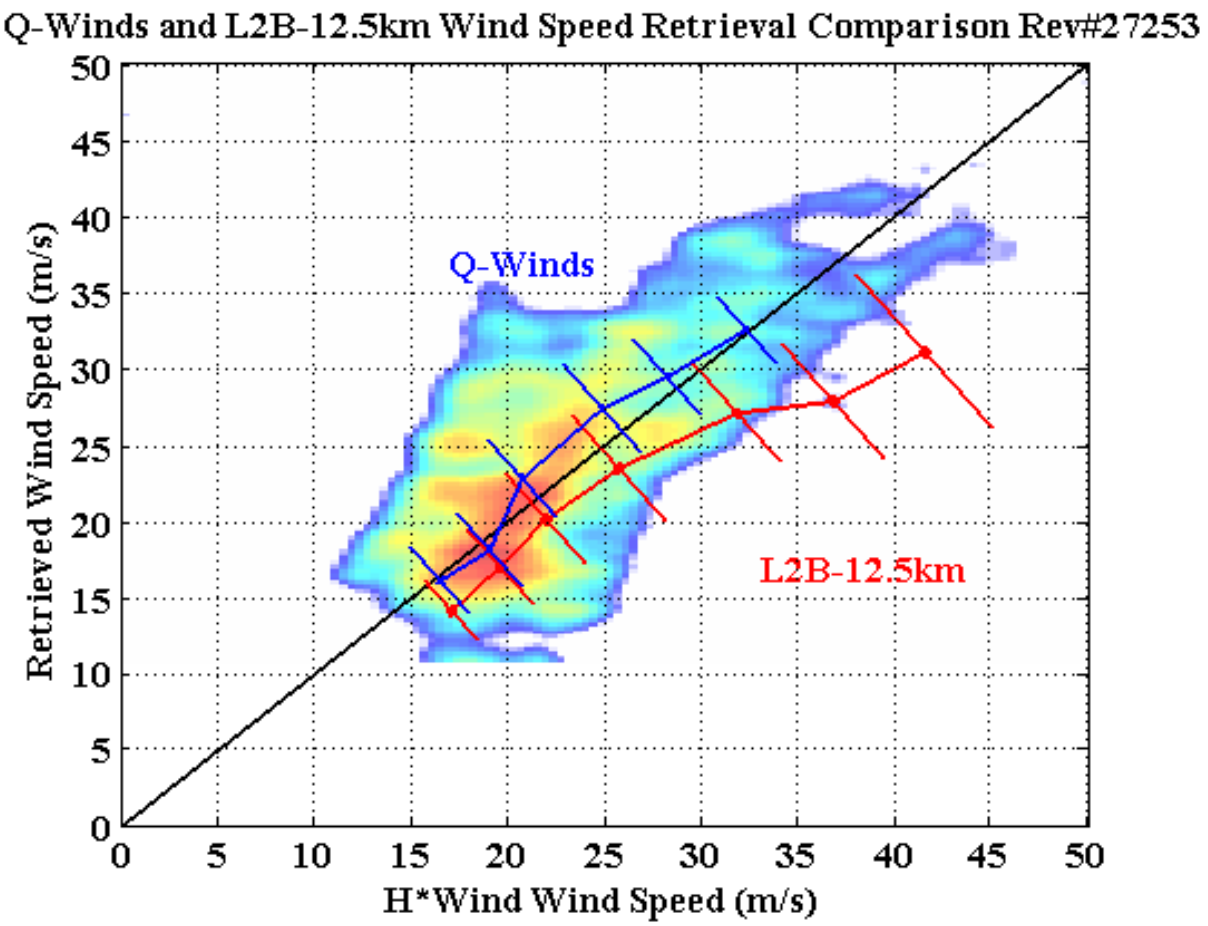


Fig. 4.7: Binned-average wind speed comparisons of Q-Winds and L2B-12.5km with H*Wind surface truth for Hurricane Ivan rev#27253. The blue symbols are Q-Winds with rain flags applied and the red symbols are the binned average wind speeds of L2B-12.5km.

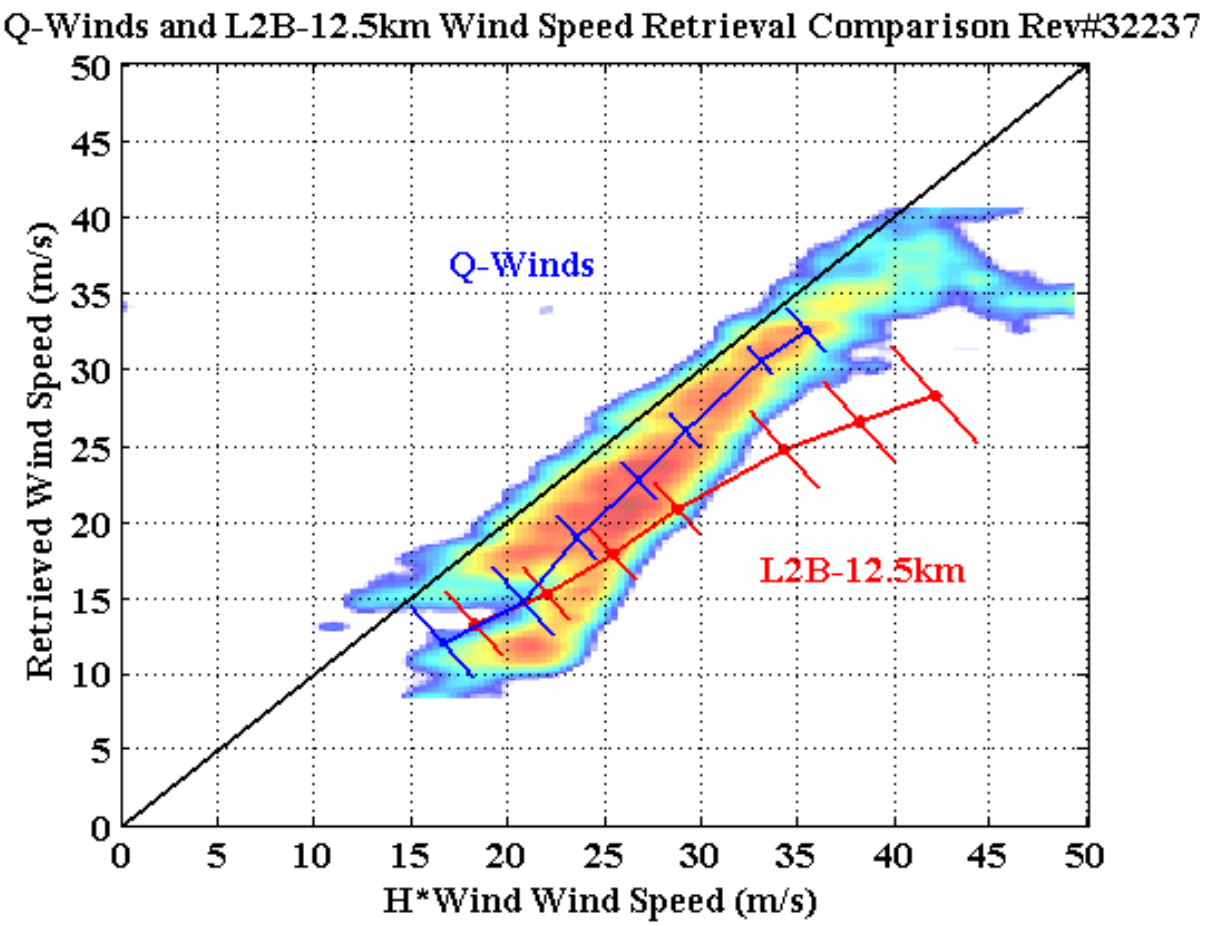


Fig. 4.8: Binned-average wind speed comparisons of Q-Winds and L2B-12.5km with H*Wind surface truth for Hurricane Katrina rev#32237. The blue symbols are Q-Winds with rain flags applied and the red symbols are the binned average wind speeds of L2B-12.5km.

These results show that the mean wind speed of Q-Winds and L2B-12.5km both agree quite well with H*Wind surface truth for low to moderate wind speeds (< ~20 m/s). On the other hand, for H*Wind wind speed exceeding tropical storm force > 24.5 m/s (55 mph), the L2B-12.5km product significantly underestimates the peak wind speed while Q-Winds maintains good agreement (within ~10% error). The overall wind speed statistics (18 revs) for both Q-Winds and L2B-12.5km with H*Wind (with and without QC rain flags) are shown in Fig. 4.9, and their error statistics for each binned wind speed ranges are summarized shown in Table 4.2.

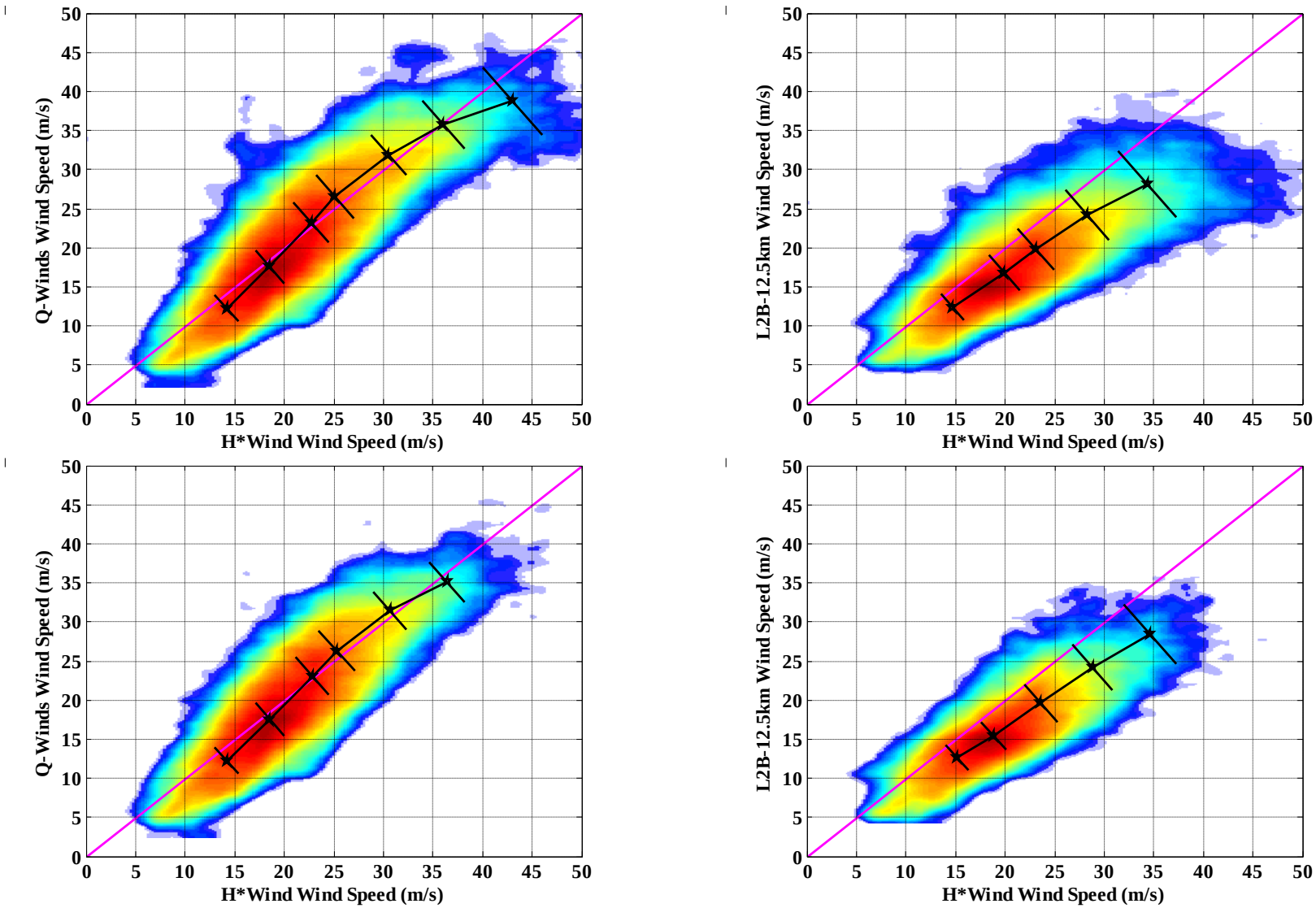


Fig. 4.9: Wind speed comparisons with H*Wind for eighteen hurricane revs. Upper left panel is Q-Winds without excess-rain flags, upper right panel is L2B-12.5km, lower left is Q-Winds with excess-rain flags applied, and lower right is L2B-12.5km with MUDH rain flags. Color is number of measurements in log scale

Table 4.2: Composite Wind Speed Comparisons to H*Wind for Eighteen Revs

| Wind speed (m/s) | Q-Winds minus H*Wind | | | JPL L2B-12.5km minus H*Wind | | |
|---|---|---|---|---|---|---|
| | All | Rain Flagged | | All | Rain Flagged | |
| | Mean (STD) | Mean (STD) | # points: (flagged/all) | Mean (STD) | Mean (STD) | # points: (flagged/all) |
| 10-15 | -1.95 (2.06) | -1.96 (2.06) | 24/2216 | -3.18 (2.53) | -2.49 (1.98) | 1012/1526 |
| 15-20 | -0.98 (2.59) | -1.02 (2.56) | 9/4118 | -2.64 (2.29) | -3.48 (2.19) | 205/5001 |
| 20-25 | 0.51 (3.15) | 0.22 (2.94) | 244/3656 | -3.23 (3.13) | -3.96 (2.89) | 2418/4761 |
| 25-30 | 1.43 (3.38) | 0.98 (3.19) | 326/2647 | -3.35 (3.54) | -4.66 (3.54) | 2930/3800 |
| 30-35 | 1.32 (3.14) | 0.79 (2.95) | 569/1842 | -5.08 (4.20) | -6.20 (4.67) | 1407/1717 |
| 35-40 | -0.33 (3.76) | -1.33 (3.11) | 495/896 | -8.12 (5.78) | N/A | 803 |
| 40-45 | -4.27 (5.30) | N/A | 371/371 | N/A | N/A | N/A |

According to results from Fig. 4.9 and Table 4.2, the mean wind speed agreements of Q-Winds and H*Wind are superior to L2B-12.5km for both "with" and "without" rain flags applied. However, it is noted that both OVW products have comparable precisions (i.e., STD's). For example, for the H*Wind wind speed bin range of 30 – 35 m/s, Q-Winds statistics are: mean = 1.32 m/s and STD = 3.14 m/s compared to L2B-12.5km mean = -5.08 m/s and STD = 4.20 m/s. After applying the quality control rain flags, approximately ~31% of elements in this Q-Winds bin were flagged and the mean wind speed improves to 0.79 m/s; and L2B-12.5km flagged ~82% and the mean wind speed slightly degrades to -6.20 m/s.

## 4.4 Extreme Winds GMF (XW-GMF) Assessment

To understand the reason for differences between Q-Winds and L2b-12.5km wind retrievals, we examine the two GMF's. Consider the dc or isotropic value of the XW-GMF (averaged from all 360° relative wind directions) compared with the corresponding SeaWinds project's isotropic QS-GMF for H- and V-pols shown in Figs. 4.10 – 4.11, respectively. For low wind speeds regions (~10 m/s), both models are almost identical; however, at higher wind speeds, the XW-GMF exhibits smaller $\sigma^0$ values than the QS-GMF, which in turn, results in higher retrieved wind speeds.

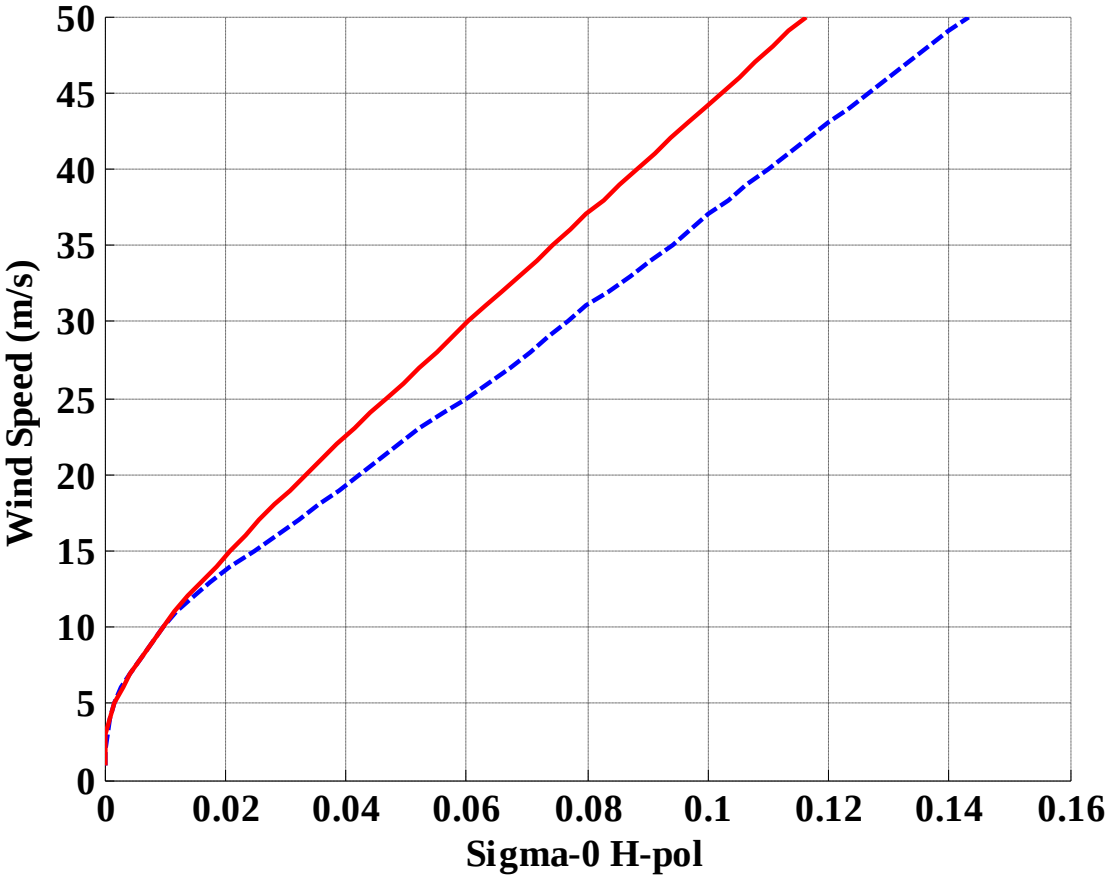


Fig. 4.10: Horizontally polarized isotropic Geophysical Model Function for QuikSCAT GMF (QS-GMF) and Extreme Winds GMF (XW-GMF). Dashed blue line denotes the QS-GMF and solid red line denotes the XW-GMF.

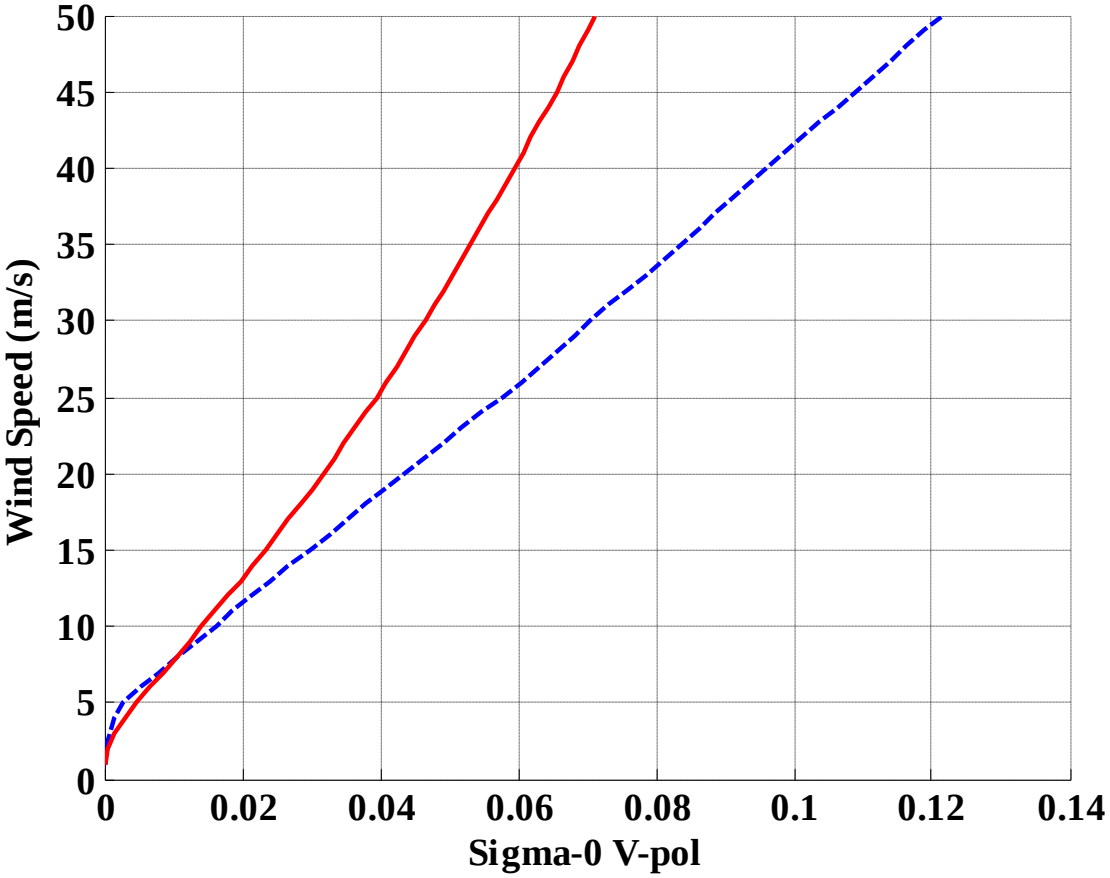


Fig. 4.11: Vertically polarized isotropic Geophysical Model Function for QuikSCAT GMF (QS-GMF) and Extreme Winds GMF (XW-GMF). Dashed blue line denotes the QS-GMF and solid red line denotes the XW-GMF.

The contribution of the GMF on wind speed retrieval is evaluated by repeating identical wind vector retrieval processing (i.e., applying the same rain effect correction and ambiguity selections) using the two different GMF's: XW-GMF and QS-GMF. The resulting wind speeds using the XW-GMF (Fig. 4.12 upper left panel) are greater than those of the QS-GMF (lower left panel), and they also have better agreement with the H*Wind surface truth (upper right panel) as shown in the scatter diagram (lower right panel). The QS-GMF wind speeds exhibit saturation with increasing hurricane wind speed, which grows to ~ 8 m/s at 35 – 40 m/s.

Although the XW-GMF is available for wind speed up to 70 m/s, the use beyond 50 m/s is not recommended for following reasons. First, only data with maximum wind speeds of 35 m/s are adequate for model training; beyond this point the model was extrapolated. Second, $\sigma^0$ at Ku-band becomes more isotropic (appears identical from all directions) at higher wind speeds and responds more weakly. Finally, high wind speeds are almost always contaminated by heavy rain and is the limiting factor in the retrieval; the uncertainty in rain correction would be too large to achieve a reliable retrieval even with a perfect GMF.

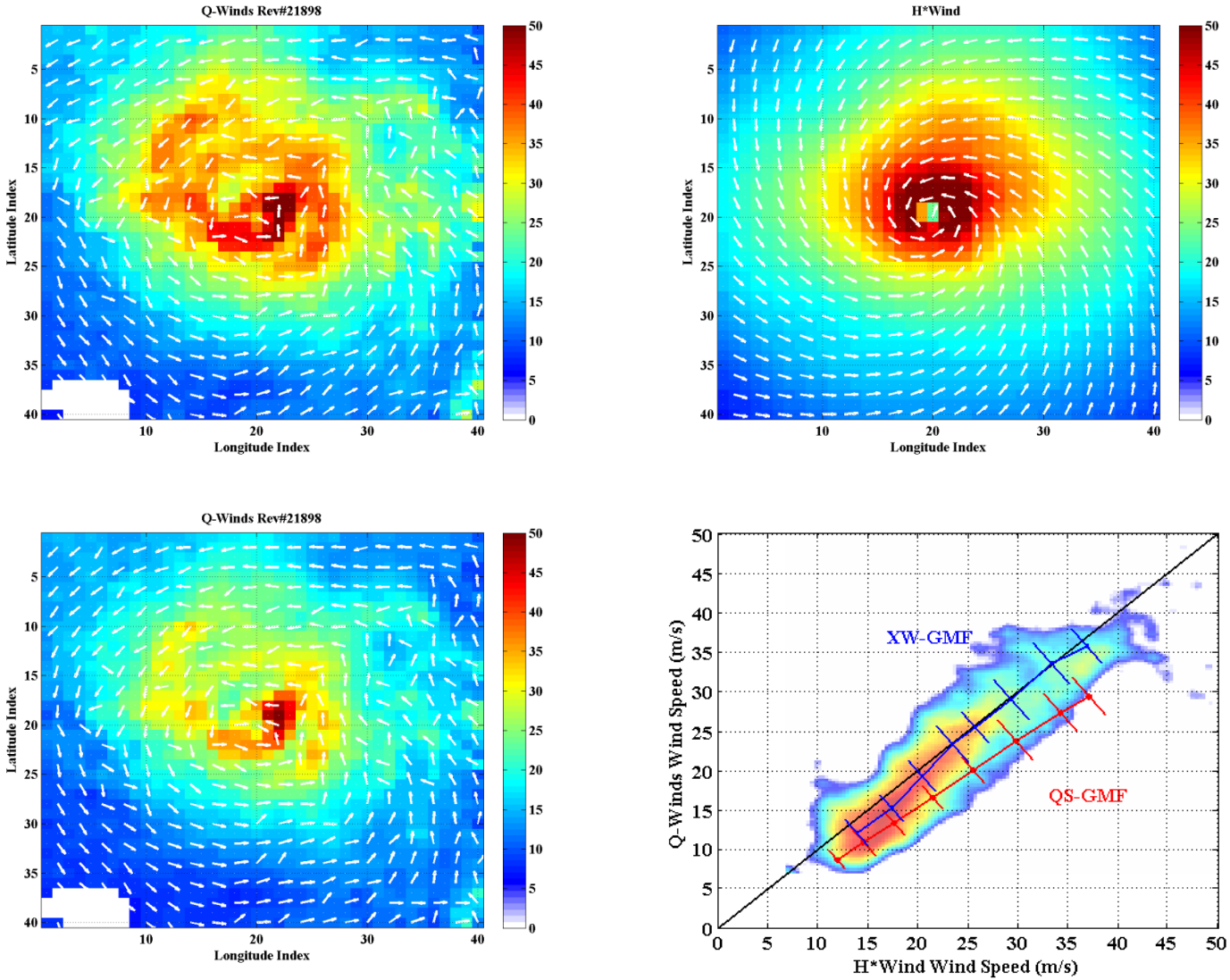


Fig. 4.12: Wind speed comparison for Hurricane Fabian using different GMF. Upper left is XW-GMF, lower left is QS-GMF, upper right is H*Wind, and lower right is wind speed scatter plot comparison.

## 4.5 Rain Correction Effectiveness

The effectiveness of the rain correction is assessed based on eighteen hurricane events by comparing Q-Winds retrieval "with" and "without" rain correction applied with H*Wind wind speeds without any constraint on rain rate. The improvement due to rain correction can be evaluated by comparing the difference between the binned-average values "with" (black stars) and "without" (blue dots) rain correction *via* the scatter diagram in Fig. 4.13.

Because severe rain conditions are usually associated with high wind speeds, we observed that rain correction has negligible effect on wind retrieval performance for wind speeds < 25 m/s; but for higher wind speeds the rain correction becomes progressively more significant. Without the correction, the binned-average wind speeds exhibit saturation, resulting in wind speeds that are too low (denoted by red circles). Alternatively, Q-Winds retrieval with the correction applied matches H*Wind surface wind speeds well in the mean up to ~45 m/s.

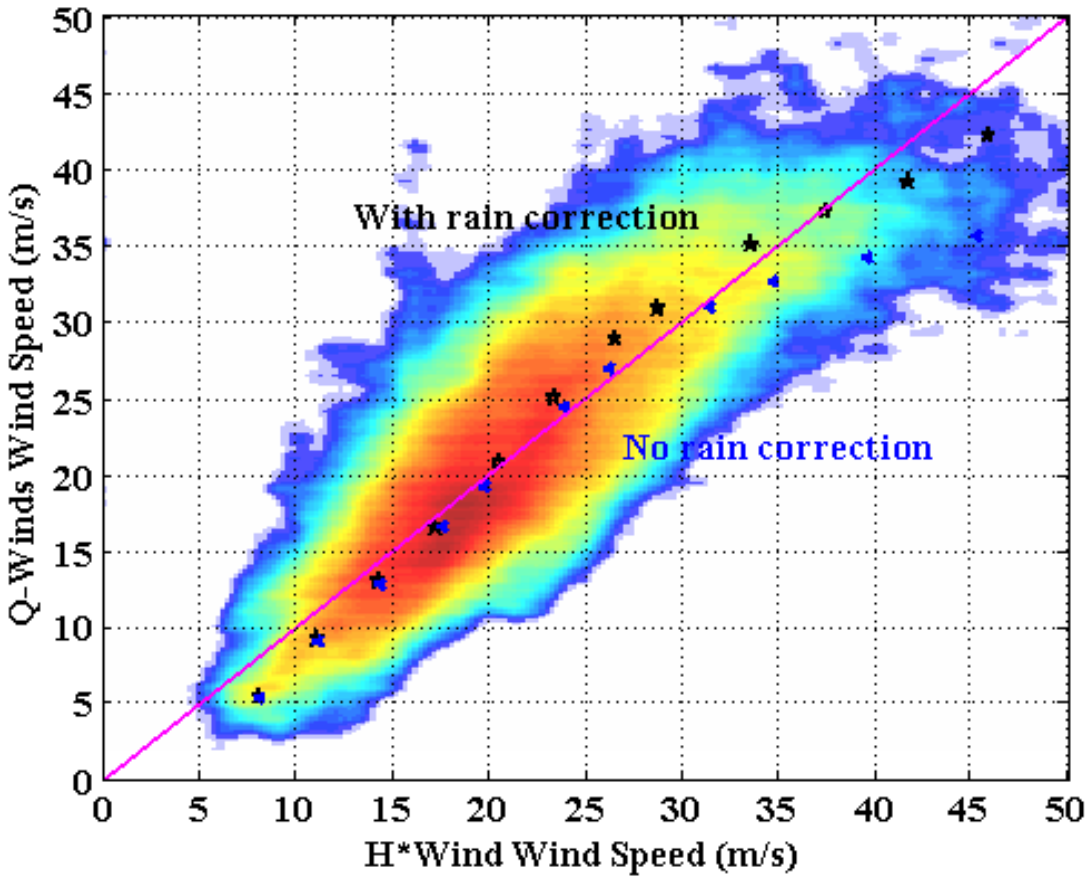


Fig. 4.13: Effectiveness of rain correction for wind speed retrieval. Scatter plot is H*Wind and rain adjusted Q-Winds retrieved wind speeds. Black stars denote binned-average wind speed with rain correction. Red circles denote binned-average wind speed without rain correction.

Unfortunately, the rain correction has to be used with caution. When implemented properly, this correction considerably improves the performance of Q-Winds OVW; otherwise, it can introduce large uncertainty in the retrieval. In order to limit the error from correcting rain and imperfect rain retrieval, an empirically derived excess-rain flagging algorithm was developed, which will be described in quality flagging section 4.7.

## 4.6 Q-Winds Directions Evaluation

Because the wind speeds for the various retrieval aliases are not the same, it is necessary to select the correct wind direction in order to retrieve the correct wind speed. In this section, Q-Winds and L2B-12.5km wind direction retrieval performance was assessed by comparing them with H*Wind directions for combined eighteen hurricanes as presented in Fig. 4.14. Overall, Q-Winds and L2B-12.5km directions agree well with H*Wind in non-raining regions and outside the eye-wall regions. However, in the presence of rain, L2B-12.5km retrieved wind directions point cross-swath (perpendicular to flight direction) [55], where the $\sigma^0$ is dominated by isotropic rain volume backscatter (see "red "boxes" in Fig. 4.14 upper panel). Furthermore, the L2B-12.5km product also occasionally miss-locates the storm center because of incorrect ambiguity selections due to rain contamination and the high wind speed gradient. Unfortunately, these errors tend to propagate over the area and magnify the erroneous ambiguity selection. In contrast, Q-Winds wind directions are in good agreement with H*Wind regardless of rain intensity, as presented in the bottom panel of Fig. 4.14.

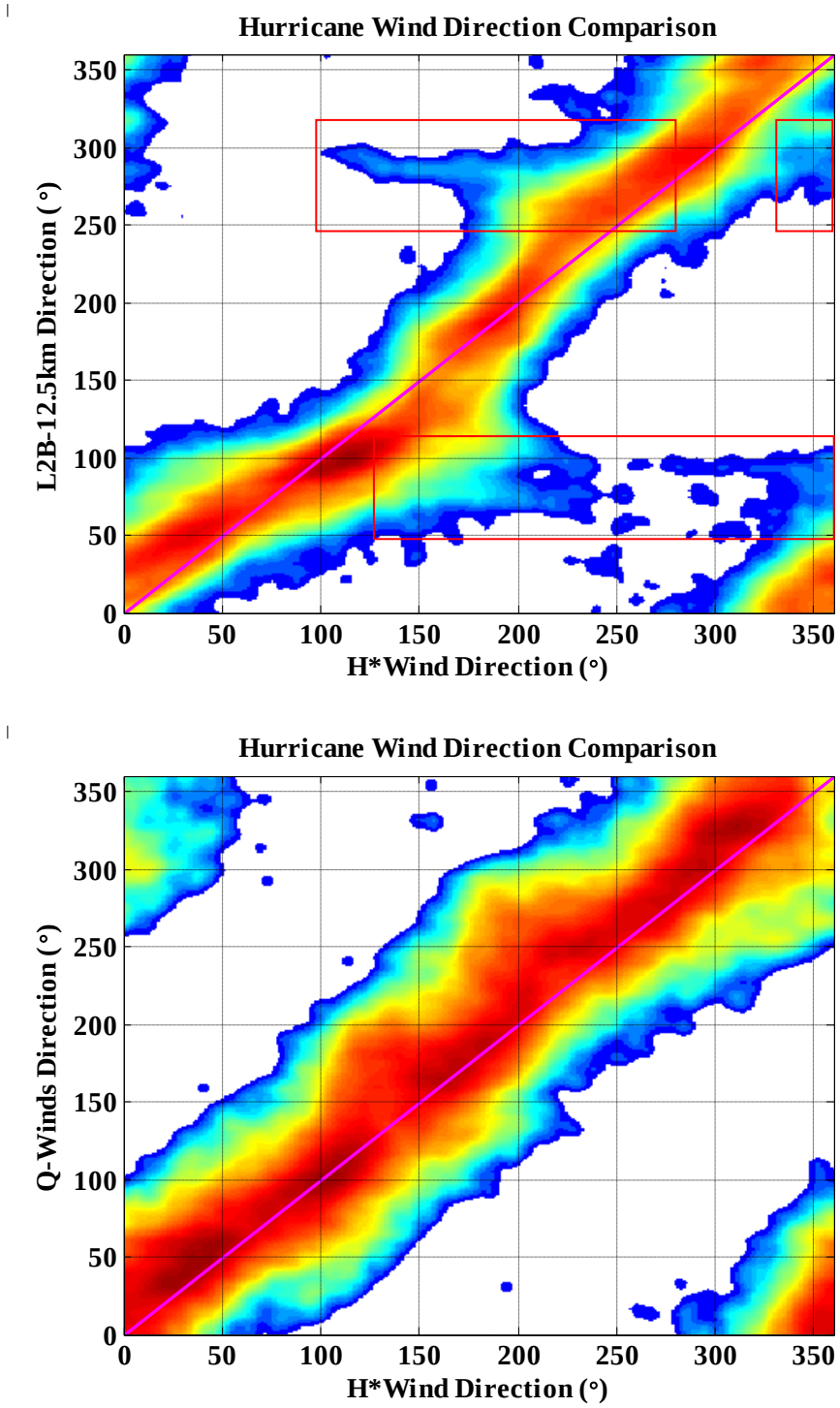


Fig. 4.14: Wind directions scatter plots compared to H*Wind directions for eighteen hurricane revs without rain flagging. Top panel is L2B-12.5km wind directions and bottom panel is Q-Winds wind directions.

## 4.7 Quality Control Rain Flagging Comparison

As the final quality assurance process, quality flags are applied to discard low confidence OVW retrievals. An accurate estimate of surface ocean $\sigma^0$ cannot be achieved when intense rain is involved; therefore, it is necessary to identify (flag) suspect wind vectors derived using rain contaminated $\sigma^0$ data. The optimal rain flagging algorithm is designed to eliminate only bogus data while preserving the high wind speed pixels. Unfortunately, wind and rain are difficult to discriminate using only QRad Tb's, which are the basis of the rain flag; hence, rain flagging in practice often discards desirable high wind speed measurements.

It is important to compare the Q-Winds excess-rain flags with the Multidimensional Histogram (MUDH) rain flags used in L2B-12.5km OVW products. The recommended MUDH rain probability of 0.1 was used as rain flags thresholds; however, for hurricane conditions, this MUDH level has difficulty in discriminating rain from legitimate high wind speeds. As a result, MUDH frequently is too conservative and flags most of TC wind vectors as being rain contaminated. On the other hand, the Q-Winds rain flagging algorithm uses QRad Tb's, which are more sensitive to rain and less affected by high wind speeds, to effectively screen rain-contaminated pixels. The following threshold was selected for optimal flagging: Tb H-pol = 190 K (Tb V-pol = 265 K where H-pol is not available) as described in Chapter-III. The Q-Winds quality flag is appended to the OVW retrieval (rather than deleting pixels); therefore, the decision to use the flag is the users' choice. The Q-Winds and MUDH quality flag statistics are

summarized below in Table 4.3. On a per rev basis, Q-Winds flags ~11% and MUDH discards ~36% of the storm.

Table 4.3: Rain flagging percentage evaluation

| Name#Rev (Category) | Q-Winds | MUDH | Name/Rev (Category) | Q-Winds | MUDH |
|---|---|---|---|---|---|
| Humberto#11805 (C1) | 2.94 | 23.38 | Ivan#27253 (C4) | 14.69 | 42.75 |
| Lili#17094 (C1) | 4.12 | 28.12 | Ivan#27260 (C5) | 17.19 | 32.44 |
| Lili#17116 (C3) | 6.75 | 52.06 | Ivan#27289 (C4) | 24.06 | 52.25 |
| Fabian#21898 (C4) | 7.19 | 34.50 | Jeanne#27431 (C2) | 5.44 | 23.31 |
| Fabian#21927 (C3) | 9.44 | 36.12 | Cindy#31481 (TS) | 7.62 | 20.62 |
| Isabel#22041 (C5) | 9.44 | 25.00 | Dennis#31531 (C1) | 4.75 | 28.25 |
| Isabel#22055 (C5) | 13.44 | 29.25 | Katrina#32230 (C3) | 3.06 | 12.94 |
| Ivan#27210 (C5) | 17.19 | 56.69 | Katrina#32237 (C3) | 14.31 | 46.06 |
| Ivan#27217 (C4) | 11.44 | 54.00 | Katrina#32251 (C5) | 25.38 | 49.69 |

## 4.8 Hurricane Radii Measurement

For hurricane analysts, the measurement of the storm's radii of gale, tropical storm and hurricane force winds are important for operational forecasts and warnings, and such information can be conveniently derived from scatterometer OVW retrievals.

The radial wind profiles are averaged by quadrant (90° sector of the TC) to determine these radii with respect to the storm center. The comparisons of the storm quadrant average wind speeds profiles of H*Wind surface wind speeds and Q-Winds are shown in Figs. 4.15 – 4.18 and the statistics are presented in Table 4.4. The radial profiles are calculated on the 45 deg diagonal

through the storm from northwest-to-southeast and northeast-to-southwest as shown in the left and right panels in Figs. 4.14 – 4.18, respectively. The horizontal lines correspond to wind speed thresholds for gale-force (17.5 m/s), tropical storm-force (25.7 m/s) and hurricane force (33 m/s) wind speeds. For these cases, which are typical, the various wind radii derived from Q-Winds agrees well with those derived from H*Wind.

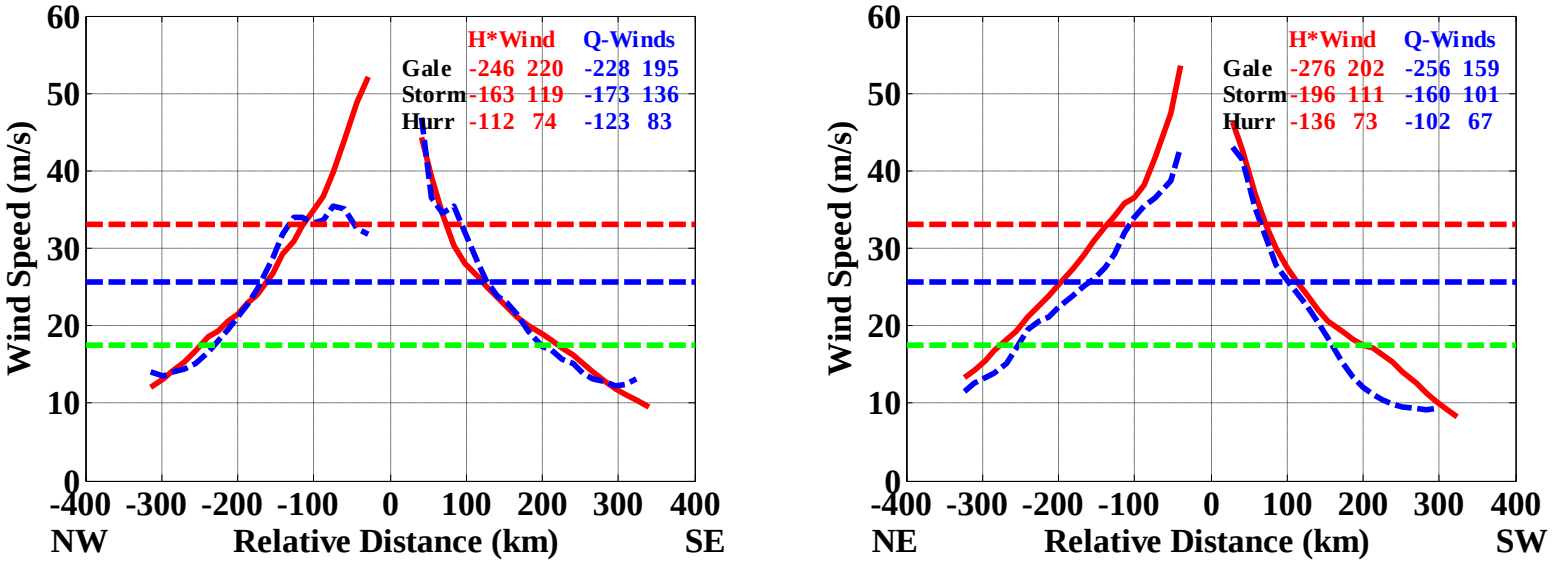


Fig. 4.15: Quadrant average wind speeds comparisons for Hurricane Fabian (rev#21898). Left panels are diagonal penetration from northwest to southeast. Right panels are diagonal penetration from northeast to southwest. Solid red lines are H*Wind and blue dash lines are Q-Winds with quality flags applied. The horizontal lines are the “gale”, “tropical storm”, and “hurricane” threshold lines from bottom to top.

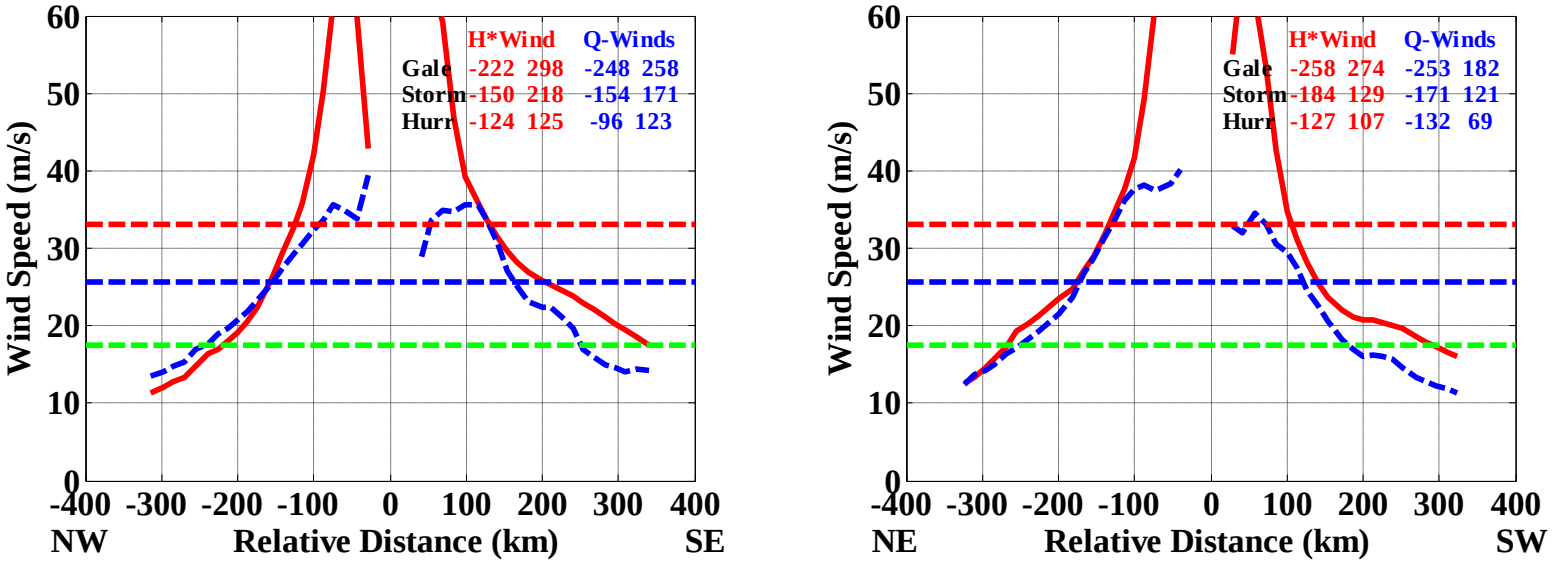


Fig. 4.16: Quadrant average wind speeds comparisons for Hurricane Isabel (rev#22055). Left panels are diagonal penetration from northwest to southeast. Right panels are diagonal penetration from northeast to southwest. Solid red lines are H*Wind and blue dash lines are Q-Winds with quality flags applied. The horizontal lines are the "gale", "tropical storm", and "hurricane" threshold lines from bottom to top.

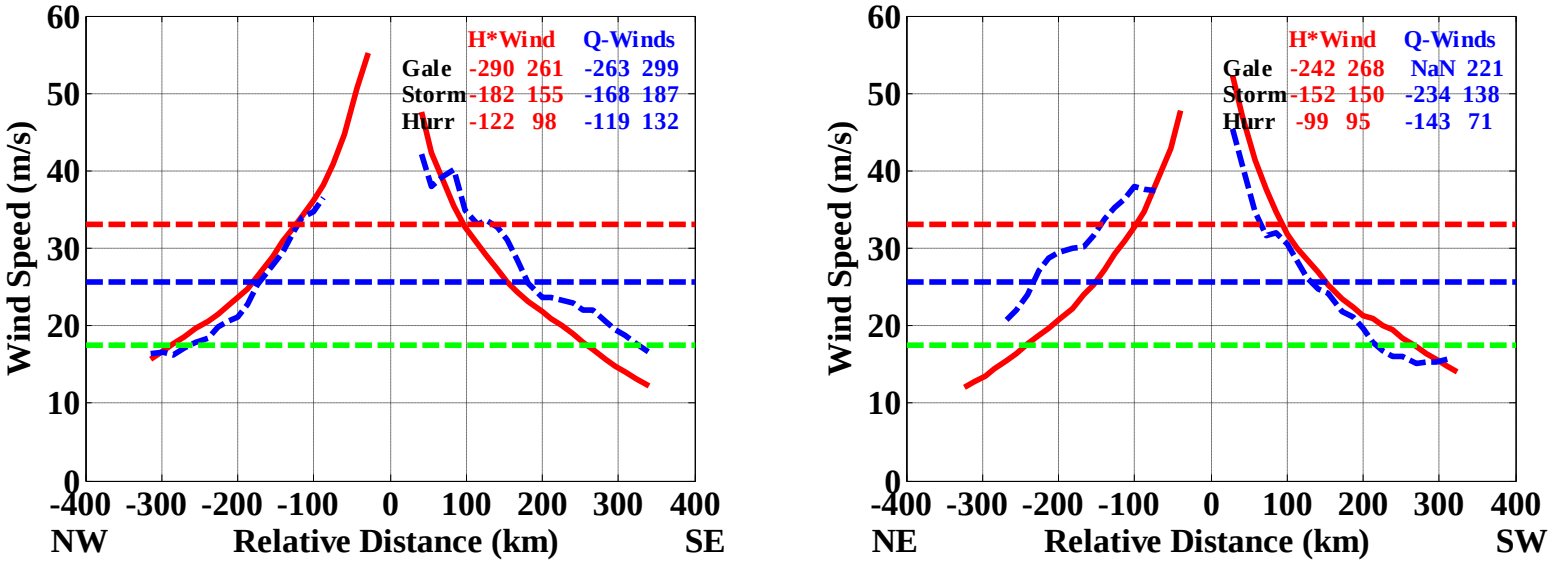


Fig. 4.17: Quadrant average wind speeds comparisons for Hurricane Ivan (rev#27253). Left panels are diagonal penetration from northwest to southeast. Right panels are diagonal penetration from northeast to southwest. Solid red lines are H*Wind and blue dash lines are Q-Winds with quality flags applied. The horizontal lines are the “gale”, “tropical storm”, and “hurricane” threshold lines from bottom to top.

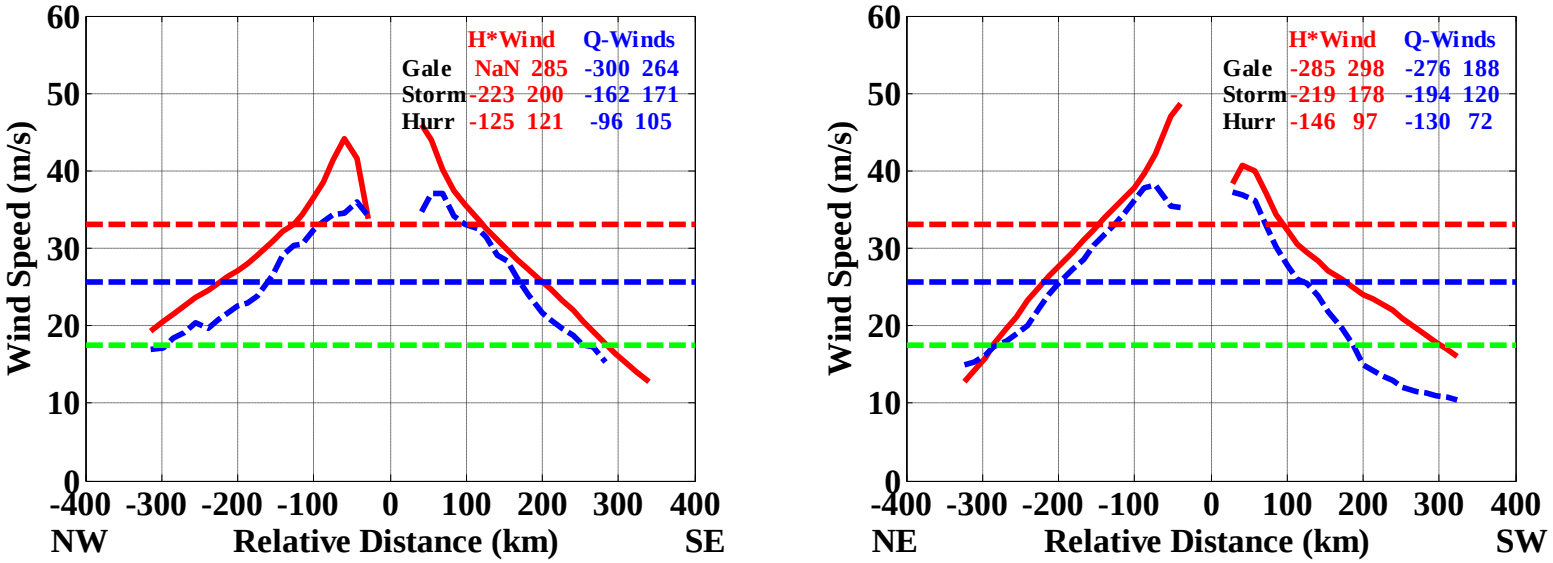


Fig. 4.18: Quadrant average wind speeds comparisons for Hurricane Katrina (rev#32237). Left panels are diagonal penetration from northwest to southeast. Right panels are diagonal penetration from northeast to southwest. Solid red lines are H*Wind and blue dash lines are Q-Winds with quality flags applied. The horizontal lines are the “gale”, “tropical storm”, and “hurricane” threshold lines from bottom to top.

Table 4.4: H*Wind and Q-Winds storm radii comparison

| Hurricane (Rev#) | Storm Class | Northwest | | Northeast | | Southwest | | Southeast | |
|---|---|---|---|---|---|---|---|---|---|
| | | H*Wind | Q-Winds | H*Wind | Q-Winds | H*Wind | Q-Winds | H*Wind | Q-Winds |
| | | km (nmi) | km (nmi) | km (nmi) | km (nmi) | km (nmi) | km (nmi) | km (nmi) | km (nmi) |
| Fabian (#21898) | Gale | 246 (133) | 228 (123) | 276 (149) | 256 (138) | 202 (109) | 159 (86) | 220 (119) | 195 (105) |
| | Storm | 163 (88) | 170 (92) | 196 (106) | 160 (86) | 111 (60) | 101 (55) | 119 (64) | 136 (73) |
| | Hurricane | 112 (60) | 128 (69) | 136 (73) | 102 (55) | 73 (39) | 67 (36) | 74 (40) | 83 (45) |
| Isabel (#22051) | Gale | 222 (120) | 248 (134) | 258 (139) | 253 (137) | 274 (148) | 182 (98) | 298 (161) | 258 (139) |
| | Storm | 150 (81) | 154 (83) | 184 (99) | 171 (92) | 129 (70) | 121 (65) | 218 (118) | 171 (92) |
| | Hurricane | 124 (67) | 96 (52) | 127 (69) | 132 (71) | 107 (58) | 69 (37) | 125 (67) | 123 (66) |
| Ivan (#27253) | Gale | 290 (157) | 263 (142) | 242 (131) | N/A | 268 (145) | 221 (119) | 261 (141) | 299 (161) |
| | Storm | 182 (98) | 168 (91) | 152 (82) | 234 (126) | 150 (81) | 138 (75) | 155 (84) | 187 (101) |
| | Hurricane | 122 (66) | 119 (64) | 99 (53) | 143 (77) | 95 (51) | 71 (38) | 98 (53) | 132 (71) |
| Katrina (#32237) | Gale | N/A | 300 (162) | 285 (154) | 276 (149) | 298 (161) | 188 (102) | 285 (154) | 264 (143) |
| | Storm | 223 (120) | 162 (87) | 219 (118) | 194 (105) | 178 (96) | 120 (65) | 200 (108) | 171 (92) |
| | Hurricane | 125 (67) | 96 (52) | 146 (79) | 130 (70) | 97 (52) | 72 (39) | 121 (65) | 105 (57) |

Because of the symmetrical nature of H*Wind surface wind analysis, the radial wind speed profiles are usually similar from both “storm diagonal directions” (northwest-to-southeast and northeast-to-southwest). For example shown in Fig. 4.19, consider Hurricane Fabian rev#21898. The cloud pattern viewed from the GOES-12 cloud track satellite (Fig. 4.19 (left)) reveals the asymmetrical structure of Hurricane Fabian; the densest region of clouds are clustered in the northeastern quadrant. However, the radial wind speed profile determined from H*Wind (red lines in Fig. 4.15) are almost identical for both penetrations, but some differences can be noticed for Q-Winds radial wind speed profile (blue lines in Fig. 4.15).

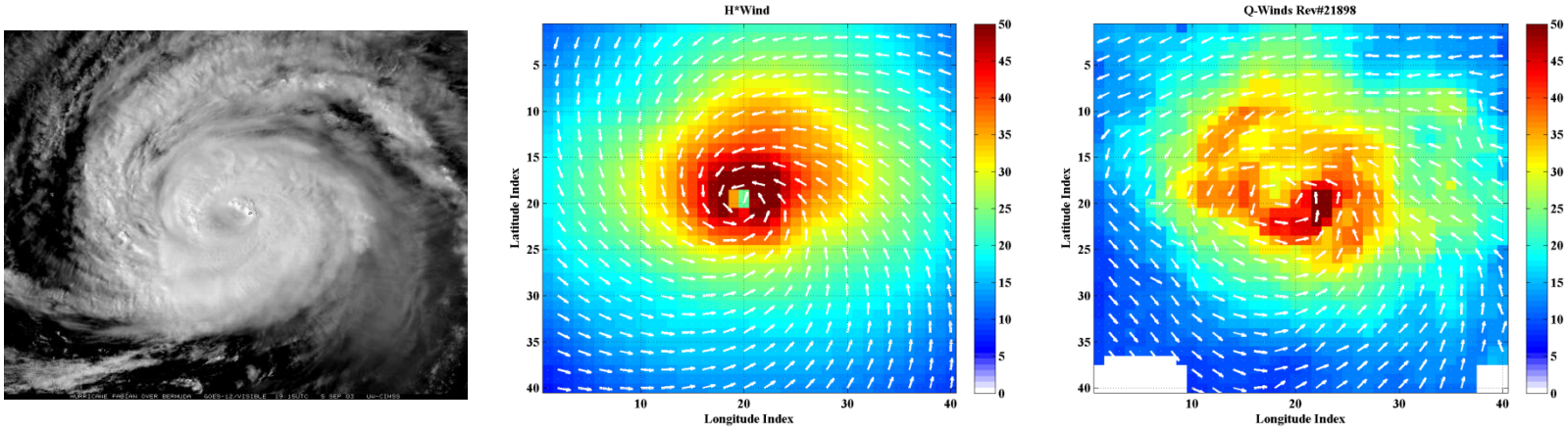


Fig. 4.19: Hurricane Fabian. Left is cloud pattern from GOES-12 visible imagery, center is H*Wind, and right is Q-Winds

## 4.9 Implementation Considerations

Even though Q-Winds significantly improves the current QuikSCAT wind retrieval algorithm for hurricane measurement, the use of Q-Winds has been validated only up to 45 m/s. Extending the wind speed range beyond this point is suspect for the following reasons:

1. Sigma-0 saturation of Ku-band scatterometer GMF. As the wind condition grows stronger, the ocean surface becomes more isotropic (i.e., less sensitive to wind direction), and the ocean radar backscatter becomes less responsive to ocean roughness (i.e., less sensitive to wind speed).
2. Sigma-0 measurements error. Because of the uncertainty of the $\sigma^0$ measurement, this GMF saturation effect magnifies wind speed retrieval errors at wind speeds > ~45 m/s.
3. Imperfect rain correction. Designed as a scatterometer, the QuikSCAT Radiometer (QRad) is not an optimum radiometer. The QRad brightness temperature measurements have large standard deviations (NEDT's), which this leads to error in rain the correction. Also, because of the antenna limited spatial resolution in the measurements (~25 km), partial beam filled rain cannot be estimated accurately.

# CHAPTER-V: CONCLUSIONS

The SeaWinds scatterometer on QuikSCAT has been demonstrated to accurately measure global synoptic ocean surface wind vectors; however, it exhibits significant shortcomings for hurricane applications. Specifically, SeaWinds is highly sensitive to rain and the model function saturates at high wind speed regime, which leads to significant underestimates of the peak wind speeds in extreme wind events e.g., tropical cyclones.

Although SeaWinds was not designed for tropical cyclone wind vector retrieval application, this dissertation explores a signal processing algorithm that was implemented to improve this capability. This research expands the utility of SeaWinds by using self-collocated active and passive measurements of ocean radar backscatter and brightness temperature in a novel active/passive OVW retrieval algorithm (known as Q-Winds) for hurricane measurements. This research also develops an atmospheric transmission correction for rain, a special hurricane GMF, and an effective rain flagging QC algorithm.

Q-Winds OVW retrievals are presented for eighteen hurricane QuikSCAT overpasses during 2001 - 2005, where simultaneous NOAA HRD aircraft flights occurred and surface winds were produced using the H*Wind analysis procedure. Comparisons are presented between H*Wind "surface truth" and SeaWinds OVW retrievals from both Q-Winds and JPL L2B-12.5km products. Results show that the L2B-12.5km product cannot reliably measure peak hurricane

wind speeds > 30 m/s, whereas Q-Winds compares well with H*Wind for wind speeds > 40 m/s (equivalent to a strong hurricane Category-1). Further, Q-Winds wind directions agreement with H*Wind is superior to L2B-12.5km directions, especially in the presence of rain.

Unfortunately, this Q-Winds algorithm is not able to measure the hurricane peak wind speed because of severe rain contamination; however, it can provide reliable hurricane radii information up to hurricane-force wind. The ability to measure wind radii for storm, gale, and hurricane force winds are valuable and provide critical information used in TC scientific analysis and operational warnings and forecasting. Furthermore, the Q-Winds QC rain flags provide a reliable method to identify low confidence OVW retrievals and thereby provide high quality data for scientific research and potentially near-real time storm analysis in operational application.

Although, the results in this dissertation are from hurricanes in the Atlantic Ocean, Gulf of Mexico, and Caribbean Sea, Q-Winds algorithm does not have geographical location restriction; therefore, this algorithm can be used worldwide. This capability extends the Q-Winds usage for other type of storms such as typhoon in the Pacific Ocean and mid-latitude cyclones such as extratropical cyclones.

The usage of Q-Winds algorithm for extra-tropical cyclones, which are larger and dryer than TC's, i.e., less rain contamination, offers significant advantages over the L2B-12.5km product. Because extra-tropical cyclones still have similar cyclonic wind rotations, the algorithm should

work exceedingly well, and with the QRad Tb's improved rain correction is possible over that provided in tropical cyclones where there is more rain of greater intensity. Because of our improved XW-GMF, the Q-Winds will much higher wind speeds which will provide valuable scientific and operational data not presently available. In summary, the algorithm is expected to perform even better than it does in TC's.

As far as the concerns for Q-Winds improvement and future applications, there are still opportunities for further advancement. Given more SeaWinds observations of tropical cyclones and associated "surface truth" from more aircraft underflights, this algorithm can be further improved by GMF refinement and to refinement of the rain correction algorithm. But the ultimate limitation of this technique is the saturation of the ocean surface roughness, which will restrict the retrieved wind speed to approximately 50 - 70 m/s.

Furthermore, the accuracy of the atmospheric transmission correction due to rain may be improved through a more sophisticated model. The current rain correction coefficient is mainly relies on the QRad brightness temperature and unfortunately the radiometric precision of QRad is rather inadequate for this application. The correction model may be refined using other parameters, e.g., ocean radar backscatter (wind) to Tb (rain) ratio.

For future operational application usage, recently, the Q-Winds hurricane retrieval algorithm was selected to be incorporated in Joint Hurricane Testbed (JHT) program for hurricane season 2009

- 2010. The proposed future works involves the development and operational implementation of an improved near-real time estimate of hurricane wind vector using Q-Winds algorithm using the NOAA NESDIS real-time SeaWinds L2B-12.5km product. Primary tasks include:

1. Development and testing of prototype algorithm during the 2009 hurricane season.
2. Algorithm validation and refinement based on operational user feedback and 2009 season observations.
3. Transition of the operational Q-Winds software system and integration at the TPC/NHC and JTWC operations centers for the 2010 hurricane season.
4. Development of appropriate training materials to facilitate proper operational utilization of new QuikSCAT product.

Once the validation phase is completed, all QuikSCAT hurricane passes will be processed in near-real time manner using the improved Q-Winds algorithm. Q-Winds will output OVW in the BUFR format, Merged Geophysical Data Record, the so called MGDR Lite, which is presently being used by forecasters at TPC/NHC and JTWC.

As this near-real time application is advanced, there will be undoubtedly useful scientific spin-off as well. In the future the JPL scatterometer project, will certainly performs reprocessing of the entire SeaWinds dataset, and the opportunity exists for using Q-Winds to provide an extreme winds data set for weather and climate research.

# APPENDIX A: MAXIMUM LIKELIHOOD ESTIMATION

Maximum likelihood (MLE) is a well-known statistical method to estimate parameters using a mathematical model and applying this to an empirical dataset with random errors of known probability distribution. The principle behind maximum likelihood estimation is to determine the variables that maximize the likelihood probability of the sample data. The advantages of this method are its robustness and its efficient method to determine the mean of the process.

Consider *x* is a continuous random variable with PDF

$$f(x; \theta_1, \theta_2, \dots, \theta_k) \tag{A.1a}$$

where $\theta_1, \theta_2, \dots, \theta_k$ are $k$ unknown constant parameters. For an experiment with $N$ independent observations, $x_1, x_2, \dots, x_N$. The likelihood function is defined as follows:

$$L(x_1, x_2, \dots, x_N | \theta_1, \theta_2, \dots, \theta_k) = L = \prod_{i=1}^{N} f(x_i; \theta_1, \theta_2, \dots, \theta_k) \tag{A.1b}$$

Assuming Gaussian distribution with identical standard deviation σ, the PDF of the distribution is given by:

$$f(x) = \frac{1}{\sigma\sqrt{2\pi}} e^{-\frac{1}{2}\left(\frac{x-\bar{x}}{\sigma}\right)^2} \tag{A.2}$$

where $\bar{x}$ denotes the mean value, and σ is the standard deviation of the process. MLE of the process is compute by (A.1) and yields:

$$L = \prod_{i=1}^{N} \frac{1}{\sigma\sqrt{2\pi}} e^{-\frac{1}{2}\left(\frac{x_i-\bar{x}}{\sigma}\right)^2} \tag{A.3a}$$

$$= \frac{1}{\left(\sigma\sqrt{2\pi}\right)^N} e^{-\frac{1}{2}\sum_{i=1}^{N}\left(\frac{x_i-\bar{x}}{\sigma}\right)^2} \tag{A.3b}$$

For convenience $L$ is usually expressed in logarithmic domain as:

$$\Lambda = \ln(L) = \ln \sum_{i=1}^{N} \ln f(x_i; \theta_1, \theta_2, \ldots, \theta_k) \tag{A.4a}$$

$$= -\frac{N}{2}\ln(2\pi) - N\ln\sigma - \frac{1}{2}\sum_{i=1}^{N}\left(\frac{x_i - \bar{x}}{\sigma}\right)^2 \tag{A.4b}$$

The MLE's of $\theta_1, \theta_2, \ldots, \theta_k$ are determined by maximizing $L$ (or Λ). Taking the partial derivatives of Λ with respect to each parameter and equates to zero yields:

$$\frac{\partial(\Lambda)}{\partial \bar{x}} = \frac{1}{\sigma^2}\sum_{i=1}^{N}(x_i - \bar{x}) = 0 \quad \text{(A.5a)}$$

$$\frac{\partial(\Lambda)}{\partial \sigma} = -\frac{N}{\sigma} + \frac{1}{\sigma^3}\sum_{i=1}^{N}(x_i - \bar{x})^2 = 0 \quad \text{(A.5b)}$$

Solving (A.5a) and (A.5b) simultaneously, solutions are:

$$\bar{x} = \frac{1}{N}\sum_{i=1}^{N} x_i \quad \text{(A.6a)}$$

$$\sigma = \sqrt{\frac{1}{N}\sum_{i=1}^{N}(x_i - \bar{x})^2} \quad \text{(A.6b)}$$

This implies that by minimizing $\sum_{i=1}^{N}(x_i - \bar{x})^2$ will also maximizes *L* (or Λ).

# APPENDIX B: WIND VECTOR RETRIEVAL USING MLE

The objective function, $J(u,\chi)$, is a convex function of the accumulative residue between the measurements and the model formed from the available measurements in a given WVC is expressed as follows:

$$J(u,\chi) = \sum_{k=1}^{n} \left( \frac{\sigma^0_{meas\ ,k} - \sigma^0_{mod\ ,k}}{\delta_k} \right)^2 \quad \text{(B.1)}$$

where $\sigma^0_{meas}$ = the measurement $\sigma^0$

$\sigma^0_{mod}$ = the model $\sigma^0$ from the GMF($u,\chi$)

$\delta$ = the estimated standard deviation of the $\sigma^0$ measurement

$u$ = wind speed (m/s)

$\chi$ = relative wind direction (°)

$k$ = # measurements in a particular WVC

The normalized standard deviation of measurement $\sigma^0$, often denoted by $K_p(\sigma^0)$, indicates the accuracy of the $\sigma^0$ measurement and is used to weight the residue of the objective function. The $K_p(\sigma^0)$ is a combination of uncertainty in the GMF, $K_{pm}$, signal noise due to fading and thermal noise, $K_{pc}$. The $K_p(\sigma^0)$ is defined as:

$$K_p(\sigma^0) = \sqrt{\left(K_{pc}^2 + K_{pm}^2 + K_{pc}^2 K_{pm}^2\right) GMF(u, \chi)} \tag{B.2a}$$

$$= \sqrt{\frac{Var\left(\sigma_{meas}^0\right)}{\sigma^0}} \tag{B.2b}$$

where $K_{pc}$ is expressed as [24]

$$K_p(\sigma^0) = \frac{\sqrt{Var\left(\sigma_{meas}^0\right)}}{\sigma^0} \tag{B.3}$$

The coefficients α, β, and γ characterize the surface scatters, signal-to-noise ratio (SNR) at the receiver, and the receiver design [24, 56]; and σt is the true σ0 without communication noise.

# LIST OF REFERENCES


[1] M. J. Brennan, H. D. I. Cobb, and R. D. Knabb, "Observations of gulf of Tehuantepec gap wind events from QuikSCAT: An updated event climatology and operational model evaluation," in *Preprints, 22nd Conference on Weather Analysis and Forecast/18th Conference on Numerical Weather Prediction*. Park City, UT: Amer. Meteor. Soc., 2007.

[2] Z. Jelenak and P. S. Chang, "QuikSCAT Follow-On Mission: User Impact Study," i. N. report, Ed., 2008.

[3] NOAA Operational Satellite Surface Vector Winds Requirements Workshop, Tropical Prediction Center, Miami, 2006, http//manati.orbit.nesdis.noaa.gov/SVW_nextgen/SVW_workshop_report_final.pdf.

[4] M. J. Brennan and R. D. Knabb, "Operational evaluation of QuikSCAT ocean surface vector winds in TC at the Tropical Prediction Center/National Hurricane Center," in *11th Symposium on Integrated Observing and Assimilation Systems for the Atmosphere, Oceans, and Land Surface*. San Antonio, TX: Amer. Meteor. Soc., 2007.

[5] M. J. Brennan, J. R. Rhome, and R. D. Knabb, "The extratropical transition of Hurricane Helene (2006): Observation of structural evolution and operational model evaluation using QuikSCAT," in *Preprint, 22nd Conference on Weather Analysis and Forecast/18th Conference on Numerical Weather Prediction*. Park City, UT: Amer. Meteor. Soc., 2007.

[6] R. K. Moore, "Satellite radar and oceanography -- An introduction," *Oceanography from Space*, pp. 355-366, 1965.

[7] R. K. Moore and W. J. Pierson, "Measuring sea state and estimating surface winds from a polar orbiting satellite," Inter. Symp. on Electromagnetic Sensing of the Earth from Satellites, Miami Beach, FL, 1965

[8] W. L. Jones, W. L. Grantham, L. C. Schroeder, J. W. Johnson, C. T. Swift, and J. L. Mitchell, "Microwave scattering from the ocean surface," *IEEE Trans. on MTT*, pp. 1053-1058, 1975.

[9] W. L. Jones and L. C. Schroeder, "Radar backscatter from the ocean dependence on surface friction velocity," *Boundary Layer Meteorology 13*, pp. 133-149, 1978.

[10] W. L. Jones, L. C. Schroeder, and J. L. Mitchell, "Aircraft measurements of the microwave scattering signature of the ocean," *IEEE Trans. Antennas Propagation/IEEE J. Oceanic Eng. (Special Issue on Radio Oceanography)*, vol. AP-25, pp. 52-61, 1977.

[11] W. L. Jones, F. J. Wentz, and L. C. Schroeder, "Algorithm for inferring wind stress from Seasat-A," *AIAA J. of Spacecraft and Rockets*, vol. 15, pp. 368-374, 1978.

[12] J. W. Wright, "Backscattering from capillary waves with application to sea clutter," *IEEE Trans. Ant. Prop.*, vol. AP-14, pp. 749-754, 1966.

[13] R. K. Moore and W. L. Jones, "Satellite scatterometer wind vector measurement - the legacy of the Seasat Satellite Scatterometer," in *IEEE GeoSci Rem Sens Newsletter*, 2004.

[14] W. L. Grantham, E. M. Bracalente, W. L. Jones, and J. W. Johnson, "The Seasat-A satellite scatterometer," *IEEE J. Oceanic Eng.*, vol. OE-2, No. 2, pp. 200-206, 1977.

[15] D. J. Carter and S. J. Austin, "European Space Agency's remote sensing satellite (ERS-1) Active Microwave Instrumentation (AMI) flight model performance," in *Digest IGARSS 90*, vol. 3. College Park, MD, 1990, pp. 2081-2084.

[16] L. F. Blivens and J. P. Giovanangeli, "An experimental study of microwave scattering from rain- and wind-roughened seas," *Int'l J. Rem. Sens.*, vol. 14, pp. 855-869, 1993.
[17] W. L. Grantham, E. M. Bracelente, C. L. Britt, F. J. Wentz, W. L. Jones, and L. C. Schroeder, "Performance evaluation of an operational spaceborne scatterometer," *IEEE Trans. Geosci. Rem. Sens.*, vol. GE-20, pp. 250-254, 1982.
[18] F. M. Naderi, M. H. Freilich, and D. G. Long, "Spaceborne radar measurement of wind velocity over the ocean - An overview of the NSCAT scatterometer system," *Proc. IEEE*, vol. 79, pp. 850-866, 1991.
[19] M. H. Freilich and R. S. Dunbar, "The accuracy of the NSCAT 1 vector winds: Comparison with National Data Buoy Center buoys," *J. Geophys. Res.*, vol. 104, pp. 11231-11246, 1999.
[20] S. J. Shaffer, "A Median-Filter-Based ambiguity algorithm for NSCAT," *IEEE Trans. Geosci. Remote Sens.*, vol. 29, pp. 167-174, 1991.
[21] A. E. Gonzales and D. G. Long, "An assessment of NSCAT ambiguity removal," *J. Geophys. Res.*, vol. 104, pp. 11449-11457, 1999.
[22] D. G. Long and M. R. Drinkwater, "Azimuth variation in microwave scatterometer and radiometer data over Antarctica," *IEEE Trans. Geosci. Rem. Sens.*, vol. 38, pp. 1857-1870, 2000.
[23] C. L. Wu, Y. Liu, H. Kellogg, K. S. Pak, and R. L. Glenister, "Design and calibration of the SeaWinds scatterometer," *IEEE Trans. Aero. and Elec. Sys.*, vol. 39, pp. 94-109, 2003.
[24] D. G. Long and M. W. Spencer, "Radar Backscatter Measurement Accuracy for a Spaceborne Pencil-Beam Wind Scatterometer with Transmit Modulation," *IEEE Trans. Geosci. Rem. Sens.*, vol. 35, pp. 102-114, 1997.
[25] N. Ebuchi, H. C. Graber, and M. J. Caruso, "Evaluation of wind vectors observed by QuikSCAT/SeaWinds using ocean buoy data," *J. Atmos. Oceanic Technol.*, vol. 19, pp. 2049-2062, 2002.
[26] R. Gaston and E. Rodriguez, "QuikSCAT Follow-On Concept Study," Jet Propulsion Laboratory, Pasadena, California JPL Publication 08-18, April, 2008 2008.
[27] M. D. Powell, S. H. Houston, L. R. Amat, and N. Morisseau-Leroy, "The HRD real-time hurricane wind analysis system," *J. Wind Eng. Indust. Aerodyn.*, vol. 77 & 78, pp. 53-64, 1998.
[28] T. F. Hock and J. L. Franklin, "The NCAR GPS dropwindsonde," in *Bull. Amer. Meteor. Soc.*, vol. 80, 1999, pp. 407-420.
[29] M. D. Powell and P. G. Black, "The relationship of hurricane reconnaissance flight-level wind measurements to winds measured by NOAA's oceanic platforms," *J. Wind Eng. Indust. Aerodynam.*, vol. 36, pp. 381-392, 1990.
[30] E. W. Uhlhorn, P. G. Black, J. L. Franklin, M. Goodberlet, J. R. Carswell, and A. S. Goldstein, "Hurricane surface wind measurements from an operational stepped frequency microwave radiometer," *Mon. Weather Rev.*, vol. 135, pp. 3070-3085, 2007.
[31] D. E. Fernandez, "IWRAP: the imaging wind and rain airborne profiler for remote sensing of the ocean and the atmospheric boundary layer within tropical cyclones," *IEEE Trans. Geosci. Rem. Sens.*, vol. 43, pp. 1775-1787, 2005.
[32] M. D. Powell and S. H. Houston, "Surface wind fields of 1995 Hurricane Erin, Opal, Luis, Marilyn, and Roxanne at landfall," *Mon. Weather Rev.*, vol. 126, pp. 1259-1273, 1998.

[33] M. D. Powell, S. H. Houston, and T. A. Reinhold, "Hurricane Andrew's landfall in South Florida Part I: Standardizing measurements for documentation of surface wind fields," *Wea. Forecast.*, vol. 11, pp. 304-328, 1996.

[34] M. D. Powell, S. H. Houston, and T. A. Reinhold, "Hurricane Andrew's landfall in South Florida Part II: Surface wind fields and potential real-time applications," *Wea. Forecast.*, vol. 11, pp. 329-349, 1996.

[35] B. Weiss and J. LaPointe, "SeaWinds Processing and Analysis Center (SeaPAC) Level 2A Data Software Interface Specification (SIS-2)," California Inst. Technol., Jet Propulsion Lab., Pasadena, CA D-20563, 2003.

[36] F. T. Ulaby, R. K. Moore, and A. K. Fung, *Microwave Remote Sensing Active and Passive*: Artech House, 1981.

[37] M. H. Freilich and R. S. Dunbar, "Derivation of satellite wind model functions using operational surface wind analyses: An altimeter example," *J. Geophys. Res.*, vol. 98, pp. 633-649, 1993.

[38] L. C. Schroeder, D. H. Boggs, G. Dome, I. M. Halberstam, W. L. Jones, W. J. Pierson, and F. J. Wentz, "The relationship between wind vector and normalized radar cross section used to derive SeaSat-A satellite scatterometer winds," *J. Geophys. Res.*, vol. 87, No. C5, pp. 3318-3336, 1982.

[39] A. K. Ahmad, W. L. Jones, T. Kasparis, S. Vergara, I. S. Adams, and J. D. Park, "Oceanic rain rate estimates from the QuikSCAT Radiometer: A global precipitation mission pathfinder," *J. Geophys. Res.*, vol. 110, 2005.

[40] R. Mehershahi, "Ocean brightness temperature measurements using the QuikSCAT radiometer," in *Electrical Engineering and Computer Science*. Orlando: University of Central Florida, 2000.

[41] M. Susanj, "An algorithm for measuring rain over oceans using the QuikSCAT Radiometer," in *Electrical Engineering and Computer Science*. Orlando: University of Central Florida, 2000.

[42] W. L. Jones, V. J. Cardone, W. J. Pierson, J. Zec, L. P. Rice, A. Cox, and W. B. Sylvester, "NSCAT high resolution surface winds measurements in typhoon Violet," *J. Geophys. Res.*, vol. 104, No. C5, pp. 11291-11310, 1999.

[43] W. L. Jones and J. Zec, "Evaluation of rain effects on NSCAT wind retrievals," Oceans '96, Ft. Lauderdale, FL, 1996

[44] D. W. Draper and D. G. Long, "Evaluating the effect of rain on SeaWinds scatterometer measurements," *J. Geophys. Res.*, vol. 109, 2004.

[45] D. E. Weissman, M. A. Bourassa, and J. Tongue, "Effects of rain rate and wind magnitude on SeaWinds scatterometer wind speed errors," *J. Atmos. Oceanic Technol.*, vol. 19, pp. 738-746, 2002.

[46] J. R. Carswell, E. J. Knapp, P. S. Chang, P. Black, and F. D. Marks, "Limitations of scatterometry high wind speed retrieval," in *Proc. IGARSS*, 2000, pp. 1226-1228.

[47] F. J. Wentz and D. Smith, "A model function for ocean-normalized radar cross section at 14 GHz derived from NSCAT observations," *J. Geophys. Res. - Oceans*, vol. 104, pp. 11499-11514, 1999.

[48] J. Zec and W. L. Jones, "Tropical cyclone geophysical model function for ocean surface wind retrievals from NASA scatterometer measurements at high wind speed," in *Proc. IGARSS*. Hamburg, Germany, 1999, pp. 1013-1016.

[49] C. Chi and F. Li, "A comparative study of several wind estimation algorithms for spaceborne scatterometers," *IEEE Trans. Geosci. Rem. Sens.*, vol. 26, pp. 115-121, 1988.
[50] B. W. Stiles, B. D. Pollard, and R. S. Dunbar, "Direction interval retrieval with thresholded nudging: A method for improving the accuracy of QuikSCAT winds," *IEEE Trans. Geosci. Rem. Sens.*, vol. 40, pp. 79-89, 2002.
[51] L. Rice, "Improved scatterometer algorithm for measuring winds in tropical cyclones," in *Electrical Engineering*. Orlando: University of Central Florida, 1999.
[52] J. Zec and W. L. Jones, "Scatterometer-retrieved hurricane wind direction ambiguity removal using spiral dealias," in *Proc. IGARSS*, 2000, pp. 275-277.
[53] I. S. Adams, C. C. Hennon, W. L. Jones, and A. K. Ahmad, "Evaluation of hurricane ocean vector winds from WindSat," *IEEE Trans. Geosci. Remote Sens.*, vol. 44, pp. 656-667, 2006.
[54] S. H. Houston, S. J. Shaffer, M. D. Powell, and J. Chen, "Comparisons of HRD and SLOSH surface wind fields in hurricanes: Implications for storm surge modeling," *Weather Forecast.*, vol. 14, pp. 671-686, 1999.
[55] J. N. Huddleston and B. W. Stiles, "A multi-dimensional histogram rain flagging technique for SeaWinds on QuikSCAT," in *Proc. IGARSS*, vol. 3. Honolulu, HI, 2000, pp. 1232-1234.
[56] T. E. Oliphant and D. G. Long, "Accuracy of scatterometer derived winds using the Cramer-Rao bound," *IEEE Trans. Geosci. Rem. Sens.*, vol. 37, pp. 2642-2652, 1999.